

On-chip Photonic Devices for Coupling to Color Centers in Silicon Carbide

Thesis by
Chuting Wang

In Partial Fulfillment of the Requirements for the
Degree of
Doctor of Philosophy

CALIFORNIA INSTITUTE OF TECHNOLOGY
Pasadena, California

2020
Defended December 16, 2019

© 2020

Chuting Wang

ORCID: 0000-0002-3711-682X

All rights reserved

ACKNOWLEDGEMENTS

Andrei, thank you so much for the opportunity of joining your lab and working on this research project. I learned a lot that I could not learn in my undergraduate studies. This project effectively pushed my limit to become more independent researcher. I deeply appreciate your patient attitude regarding my research and coursework, allowing myself to have enough time for reflection and planning.

I thank my thesis committee members professor Painter, professor Vahala and professor Minnich for reading my thesis and providing insightful feedback during my defense.

I am very grateful to KNI staff members for maintaining tools to make cutting edge science happen. Many thanks to Guy, Matt, Nathan, Alex, Bert and Melissa for training me to operate various tools safely and efficiently.

Thank you to Faraon group members for inspiring talks and discussions in group meetings. Thank you Ioana for a lot of discussions not only related to work but also to general interests. Thank you for putting up with me when I talked too much. Thank you Evan for your help to catch up with the lab and KNI work in the beginning. Thank you Yu for your help with simulations on servers and fabrication. Thank you Tian Z. and John for asking good questions and help in the lab. Thank you Mahsa and Ehsan for many observations and operational runs in KNI. Thank you Jon for your help with the laser and the single photon detector setup. Thank you Jake for your help with fabrication and communicating with people at Montana Instruments. Thank you Mi for your strong curiosity and for convincing me to go to the gym again. Thanks again to Ioana, Mahsa, Ehsan and Jon for help with coursework.

I am thankful to my previous advisors during my undergraduate studies, professor Kai-Mei Fu and professor Kohei Itoh for introducing me into the world of quantum applications.

I am thankful to my parents for exposing me to different environments when I was kid, and for allowing me to have a good education. Thank you for the support through the years. I am thankful to my grandparents for teaching me the importance of education and how a person should live.

ABSTRACT

Optical quantum networks are important for global use of quantum computers, and secure quantum communication. Those networks require storage devices for synchronizing or making queues of processing transferred quantum information. Practical quantum information networks should minimize loss of transmitted data (photons) and have high efficiency mapping when writing data on memories (solid state qubits). This requires strong light-matter interaction that is enabled by coupling qubits to optical cavities.

The first half of the thesis focuses on emerging candidates for promising qubits in silicon carbide (SiC). The optical and quantum properties of these color centers are discussed with focus on divacancies in 4H-SiC due to their long spin coherence time. Optically detected magnetic resonance of divacancies is shown, an essential technique for reading out the qubit state using the intensity of optical emission.

The second half of the thesis focuses on hybrid photonic devices for coupling to silicon carbide qubits. Hybrid devices are made of another layer of high refractive index material other than the qubit hosting material. Evanescent coupling to qubits close to the surface can be achieved without damaging the host material. Mainly the silicon (Si) on 4H-SiC hybrid ring resonator architecture is discussed starting from design, simulation to fabrication. The fabrication includes Si membrane transfer that is an important step to create a light confining layer on 4H-SiC. The final ring resonator device shows quality factors as high as 23000.

PUBLISHED CONTENT AND CONTRIBUTIONS

- [1] Chuting Wang et al. “Hybrid silicon on silicon carbide integrated photonics platform”. In: *Applied Physics Letters* 115.14 (2019), p. 141105.
DOI:10.1063/1.5116201
W.C participated in the conception of the project, fabricated and characterized the device, gathered and analyzed the data, and wrote the manuscript with F.A.
- [2] Chuting Wang et al. “Silicon on Silicon Carbide Ring Resonators for Coupling to Color Centers”. In: *2018 Conference on Lasers and Electro-Optics (CLEO)*. IEEE. 2018, pp. 1–2.
W.C participated in the conception of the project, fabricated and characterized the device, gathered and analyzed the data, and wrote the manuscript with F.A.

TABLE OF CONTENTS

Acknowledgements	iii
Abstract	iv
Published Content and Contributions	v
Table of Contents	vi
List of Illustrations	viii
List of Tables	xii
Chapter I: Introduction	1
1.1 Optical defects and their applications in quantum information technologies	1
1.2 Silicon Carbide (SiC) material background	4
1.3 Polytypes of SiC and 4H-SiC crystal structure	4
1.4 Divacancies ($V_C V_{Si}$) in SiC as promising qubits	5
1.5 Coupling optical defects to cavities	6
Chapter II: Photoluminescence of defects and impurities in SiC	9
2.1 Divacancies in 4H-SiC	9
2.2 Cr^{4+} ions in 4H, 6H-SiC	10
2.3 Other color centers	15
Chapter III: Optically detected magnetic resonance of defects in 4H-SiC	22
3.1 Principles of ODMR	22
3.2 ODMR setup	23
3.3 ODMR results on ensemble divacancies and on Cr ions	24
Chapter IV: Design and simulations of photonic resonators	29
4.1 Silicon photonic devices for near IR wavelength	29
4.2 Principles of finite-difference time-domain (FDTD) method	30
4.3 Comparison with other EM simulation method	33
4.4 MEEP simulation of c-Si on SiC ring resonator devices	34
Chapter V: Fabrication of on-chip photonic devices for coupling to defects in SiC	42
5.1 Qubits generation in 4H-SiC	42
5.2 4H-SiC transfer	43
5.3 a-Si:H Deposition	44
5.4 c-Si Membrane Transfer	45
5.5 c-Si on SiC device patterning and fabrication	50
Chapter VI: Photonic device characterization	56
6.1 Conclusion	62
Chapter VII: Concluding Remarks	63
Bibliography	65
Appendix A: GaAs photonic crystals	72
A.1 GaAs photonic crystal fabrication	72

Appendix B: Related codes 75
 B.1 MEEP codes 78

LIST OF ILLUSTRATIONS

<i>Number</i>	<i>Page</i>
1.1 An optical quantum network consists of three components: Quantum channels (black or green lines), quantum processors (laptop icons) and quantum repeaters (star icons)	3
1.2 Left: the smallest periodic component of the SiC unit cell. The center black sphere shows a Si (C) atom and the white spheres show C (Si) atom. Right: The SiC ideal tetrahedral component viewed in the plane that is parallel to connected straight line connecting two nearest atoms of same kind (1120 plane).	6
1.3 2H, 3C, 4H and 6H-SiC stacking structure viewed in the 1120 plane. The gray frame shows the unit cell of each structure.	6
1.4 Left: Local hexagonal (2H-SiC) or cubic (3C-SiC) environment changes crystal field on atoms in bilayers of 4H-SiC. Right: 3D view of 4H-SiC crystal structure with 4 possible divacancy configuration.	7
1.5 Impression of atoms interacting with light in a Fabry-Perot cavity.	8
2.1 4 types of divacancies that occupy different carbon/silicon lattice sites.	10
2.2 Photoluminescence of divacancies in a HPSI 4H-SiC sample excited by 780nm laser at 8.4 K.	11
2.3 c-axis and basal divacancy energy level structure in 4H-SiC for C_{3v} and C_{1h} symmetry. Marks next to the red arrows specify the polarization of electric field with respect to c-axis for electric dipole allowed transitions.	11
2.4 Photoluminescence of Cr ions and divacancies in a Cr implanted 4H-SiC sample excited by 780nm laser at 8.6 K.	12
2.5 Photoluminescence of Cr ions in 4H-SiC and 6H-SiC samples in better resolution at liquid nitrogen temperature (80 K)	13
2.6 Cr^{4+} energy level structure in 4H and 6H-SiC for T_d and C_{3v} symmetry. ZPL of Cr^{4+} is associated with the transition ${}^1E \rightarrow {}^3A_2$. The number at left on level bars denotes state degeneracy and Γ specifies the irreducible representation of corresponding symmetry group. Marks next to the red arrows specify the polarization of electric field with respect to c-axis for electric dipole allowed transitions.	14

2.7	Optical lifetime measurement of Cr^{4+} ions in doped 6H-SiC at liquid helium temperature. The fitting function is $I_0 \exp(-t/\tau)$ and reveals optical lifetime of 144 μs	15
2.8	Optical lifetime measurement fitting residual shows the goodness of fitting with single exponential $I_0 \exp(-t/\tau)$	16
2.9	Summary of optical lifetime measurements of Cr^{4+} ions in implanted 4H-SiC and doped 6H-SiC samples at different temperature.	17
2.10	Photoluminescence of V ions in semi insulating 4H-SiC sample excited by 780 nm laser at liquid helium temperature.	18
2.11	V^{4+} energy level structure in 4H-SiC for T_d and C_{3v} symmetry. ZPL of V^{4+} is associated with the transition ${}^2T_2 \rightarrow {}^2E$. The number at left on level bars denotes state degeneracy and Γ specifies irreducible representation of corresponding symmetry group. Marks next to red arrows specify polarization of electric field to c-axis for electric dipole allowed transitions.	19
2.12	Photoluminescence of Mo^{5+} ions in implanted sample (orange) in comparison with PL4 divacancies in a HPSi sample (blue) excited by 780 nm laser at 8.6K	19
2.13	Photoluminescence of Cu ions in Cu implanted Si excited by 780 nm laser at 8.2K	20
2.14	Photoluminescence of Cu ions in Cu implanted Si excited by 780 nm laser at different temperatures	21
3.1	Spin population and ODMR signal change when microwave is on/off	23
3.2	Schematic of the MW gold line deposited on a 4H-SiC sample. The right figure shows the image taken from CCD camera with 780nm excitation laser on.	24
3.3	MW setup around samples. Initial setup with a single wire on samples is replaced with more robust method with wire bonding and gold line deposition directly on sample.	24
3.4	ODMR signal collection method	25
3.5	Our ODMR signal collected on undoped HPSI 4H-SiC at liquid helium temperature (~ 20 K) at left side. Right side shows results from Koehl et al. [32]	26
3.6	ODMR signal collected on undoped HPSI 4H-SiC at liquid helium temperature (~ 20 K) with wider MW sweep range.	27
3.7	Power broadening of ODMR signal of ensemble divacancies PL2	27

3.8	ODMR signal of PL1 and PL2 divacancies in Cr implanted 4H-SiC under 0.15 T at liquid nitrogen temperature.	28
4.1	Left: c-Si ring resonator on 4H-SiC for spin-photon interfaces. c-Si is drawn in red, while the transparent part underneath is 4H-SiC. Right: Cross section showing the ring resonator near color centers in the 4H-SiC underneath it, that can couple to the evanescent field of the cavity.	30
4.2	Intrinsic quality factor of Si ring resonator surrounded by air at different temperature.	31
4.3	Electric and magnetic component positions in Yee algorithm.	34
4.4	2D cylindrical ring simulation (a) Refractive index setting (green: SiC/n=2.64, yellow: Si/n=3.55 and blue: air/n=1.00)(b) $\ln E_z $ with colormap(c) Plot of $\ln E_z $ at the ring width center cross section.	35
4.5	2D cylindrical ring simulation quality factor vs. ring radius with height 360 nm and width 300 nm.	36
4.6	3D ring simulation with waveguides. (a)Refractive index setting (color distribution same with figure 4.4) (b) $\ln E_z $ (c)Quality factor vs. waveguide distance	37
4.7	2D grating simulation normalization simulation on the left. Main simulation is on the right. Top figures are refractive index configuration and bottom figures are plotting $\ln E $	39
4.8	2D grating flux depending on period and duty cycle.	39
4.9	2D grating diffraction angle change depending on duty cycle (fixed period)	40
4.10	2D grating diffraction angle change depending on period (fixed duty cycle)	40
4.11	3D grating simulation configuration. Each figure is at the center plane of the simulated space.	41
5.1	SEM image of 4H-SiC membrane surface transferred by smart cut method.	44
5.2	SEM images of a-Si roughness. (a) a-Si deposited before any patterning procedure (b) A grating coupler after etching and cleaning process	45
5.3	AFM images for comparison of roughness. (a) Deposited a-Si. (b) Deposited 20nm alumina then a-Si. (c) Transferred c-Si all on top of 4H-SiC. (d) AFM on the 4H-SiC substrate.	46

5.4	(a)Design of the photomask (b)Etched SOI chip after photolithography (light gray: Si, dark gray:SiO ₂)	49
5.5	Cleaning by transferring a floating membrane to clean water	49
5.6	Picking up the membrane, drying and attachment on the substrate.	51
5.7	Successful membrane transfer. Most membranes are single but some of them are connected.	52
5.8	Failed membrane transfer. Water scattered underneath the membrane. Heating on a hot plate caused water to evaporate and made bulges on membranes. Wrinkles in membranes allow water to enter and flush of the entire membrane.	52
5.9	Residue of ZEP cleaned with O ₂ plasma	54
5.10	SEM image of a c-Si on 4H-SiC final ring resonator device	55
6.1	The optical confocal microscope setup diagram.	57
6.2	The actual setup (left) viewed from top and (right) viewed from the right.	57
6.3	The actual Littman configuration in the setup. The red solid lines show the main laser path and the dotted line shows the feedback path.	58
6.4	The internal cavity resonances change due to different diode current (40-60 mA).	59
6.5	The actual Littman configuration in the setup. The red solid lines show the main laser path and the dotted line shows the feedback path.	60
6.6	The ECDL power drift over 8 hours.	61
6.7	Main measurements were performed through the drop port.	61
6.8	(a)Coarse measurement through the drop port with supercontinuum laser. (b)Coarse measurement through the throughput port. Arrows indicate the locations of resonances. (c) Fine measurement with tunable laser scanning. The Lorentzian fit reveals $Q \sim 23000$	62
A.1	3D periodic photonic crystal bandgap simulation.	73
A.2	3D photonic crystal simulation with defect at the center	73
A.3	Transferring a part of devices using a nanomanipulator (a) Cut through between the 2 patterned lines before grating couplers because undercut wasn't enough to detach grating couplers from the substrate (b) The probe at the left side is welded to platinum, deposited around the grating tapered part, and the device is lifted up.	74

LIST OF TABLES

<i>Number</i>		<i>Page</i>
5.1	List of samples with different ion implantation and photoluminescence	43
5.2	a-Si recipe	45
5.3	c-Si transfer procedure	47
5.4	SOI chip square patterning procedure	48
5.5	E beam writing resist related procedure	53
5.6	Si pseudo-bosch etching recipe	54
A.1	a-Si recipe	74

INTRODUCTION

1.1 Optical defects and their applications in quantum information technologies

Quantum technologies have been extensively pursued for practical applications which classical system cannot achieve. This includes quantum key distribution (QKD) for unconditionally secure communication [1–3], quantum computers for efficiently simulating complex physical quantum systems [4–6] and quantum sensing with higher sensitivity [7–9]. Quantum technologies take advantage of the quantum mechanical aspects of systems such as the no cloning theorem [10], superposition states and entanglement to surpass the classical limit. Analogous to the term "bit" used for classical information, a unit of quantum information can be denoted as quantum bit, or "qubit". A qubit can be $|0\rangle$, $|1\rangle$ or any superposition state of the two states [11]:

$$|\psi\rangle = \alpha_0|0\rangle + \alpha_1|1\rangle \quad (1.1)$$

$$|\alpha_0|^2 + |\alpha_1|^2 = 1 \quad (1.2)$$

This is unlike classical bits, which can only be in the 0 or 1 state. Qubits are two-level quantum systems in the Hilbert space spanned by $|0\rangle$ and $|1\rangle$ states. Quantum information networks will have an important role in scaling up to globally distributed quantum technologies by interconnecting quantum computers or communication sites [12–14]. Qubits with long coherence time are necessary for quantum information storage. Photons are ideal for transport of quantum information because they can travel a long distance with minimum decoherence [15]. That is why qubit-photon interfacing via bright optical transitions is highly desired. There are three essential requirements for qubits that can be practically used for optical quantum communication [16]:

- (1) There are two long-lived and coherent spin states that are nondegenerate, which corresponds to pure $|0\rangle$ and $|1\rangle$ state. (Qubit state longevity)
- (2) There exists optical pumping cycles that can polarize the spin to each pure qubit state. (Optical qubit state initialization)

(3) Luminescence corresponding to each pure qubit state can be differentiated with intensity, wavelength or in other ways. (Optical qubit state readout).

For an example the lowest two states of a spin-1 particle, $|m_s = -1\rangle$ and $|m_s = 0\rangle$ can be used as $|0\rangle$ and $|1\rangle$ of a qubit [17, 18]. How well this system works compared to an ideal two-level quantum system is characterized by the decoherence induced by coupling to other existing states[19]. A good measure of decoherence for a single qubit is the lifetime of an arbitrary superposition state such as $(\alpha_0|0\rangle + \alpha_1|1\rangle)/\sqrt{|\alpha_0|^2 + |\alpha_1|^2}$, denoted by T_2 .

As shown in figure 1.1, a scalable optical quantum network should include the following three components: quantum channels, quantum processors and quantum repeaters [20]. Quantum channels are used to transmit qubits either via free space or via optical fibers. Quantum processors at the end nodes can range from processing simple measurements of qubits for communication to complex qubit manipulation for computing. Because photon loss cannot be avoided, error correction of transmitted quantum information is necessary. Quantum repeaters are inserted at regular intervals in the quantum channels to correct errors accumulated in transmission at long distance.

An initial optical quantum network was demonstrated with trapped atoms in optical resonators [21, 22]. Although the technology for controlling trapped atoms is mature [23], trapping a single atom requires a relatively large and complicated setup and is hard to scale it up due to its volume. On the other hand, solid state system can host many qubits in the crystal within a small volume. Solid state qubits are practical for scaling up due to the potential for compact chip size and easiness of on-chip integration [24, 25]. Many different solid state qubits have been investigated, such as semiconductor quantum dots, defects or impurities in diamond, silicon carbide (SiC), silicon and rare earth ions.

The state of the art QKD demonstration was performed with nitrogen vacancy (NV) centers in diamond. This experiment established entanglement between two NV electron spins separated by 1.3 km confirmed by a loophole-free Bell inequality test [18]. The capability of purifying entangled states was also demonstrated, an important milestone in scaling up the quantum network [26]. However, NV centers suffer from a low fraction of coherent photons emitted into the zero phonon line (ZPL) and spectral diffusion, which hinders the entanglement rate. Also, the nanofabrication procedure for diamond photonic devices is not easy. It is highly possible to create surface charges on the host material during fabrication that increase

spectral diffusion of optical linewidth [27, 28]. The state of the art experimental achievements in NV centers stimulated the search for other candidate qubits in other materials that are closer to ideal qubits with long coherence time and with better optical stability.

It is reasonable to search for color centers in wide bandgap materials similar to diamond, which can have optically active deep level states. It would be beneficial if these materials are common and affordable semiconductors, such as silicon, GaAs, or SiC for future mass production. These materials are also more compatible with existing photonic integrated circuits than diamond. With these ideas in mind, different defects in SiC were recently investigated and found to be attractive as qubits. Among these, divacancies in 4H-SiC have the longest coherence time so far. In the following few sections, I will discuss different types and structure of the host material silicon carbide and divacancies in 4H-SiC in more detail.

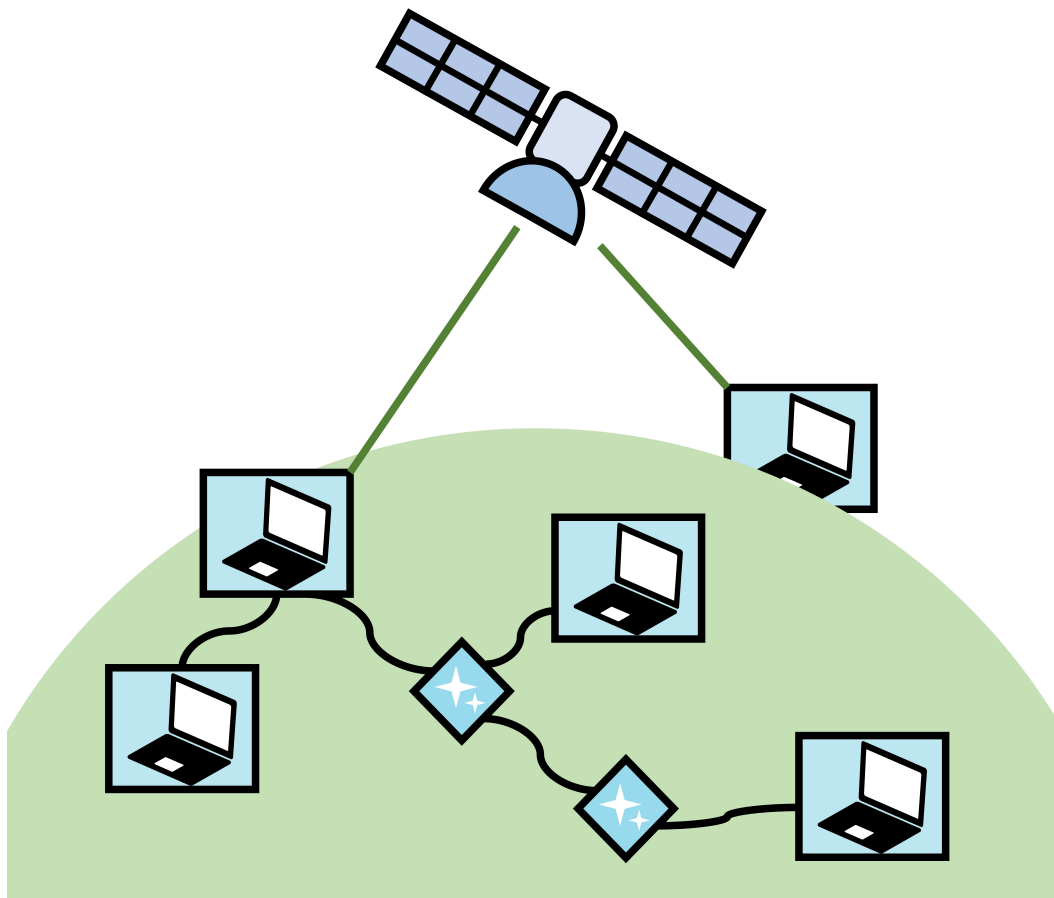


Figure 1.1: An optical quantum network consists of three components: Quantum channels (black or green lines), quantum processors (laptop icons) and quantum repeaters (star icons)

1.2 Silicon Carbide (SiC) material background

Silicon carbide (SiC) has been considered as a promising material for power electronics because of its excellent thermal conductivity, high maximum current density, small coefficient of thermal expansion and high melting point. It also has good mechanical properties and is suitable for MEMS devices. These advantages led to the development of wafer mass production and microfabrication in SiC. Although pure SiC has excellent properties, its commercialization was delayed compared to silicon due to poor electric performance caused by defects created during growth and fabrication process. The removal of the defects to unleash the electronic capability of SiC is an ongoing challenge. Some defects and impurities in SiC have been found to emit light at specific wavelength. Photoluminescence spectroscopy can be used to identify different defects and impurities in SiC. The existence of a rich literature about optical identification of these unwanted defects, accelerated the identification of potential qubits.

1.3 Polytypes of SiC and 4H-SiC crystal structure

In this section, the crystal structure of SiC is discussed for explaining divacancy photoluminescence in the later section. SiC is known to occur in different crystalline forms. Within those polymorphs, there are more than 150 polytypes [29]. Polytypes have the identical layer structure but differ in stacking sequence in the direction of crystal axis. The smallest periodic component of the SiC crystal structure is shown in figure 1.2. Ideally, 4 silicon atoms and one carbon atom (or vice versa) form a tetrahedron in this structure. If you look at any plane that intersects two silicon-carbon bonds (the 1120 plane and others related by a 120° rotation around c-axis), the structure looks like the right side of figure 1.2. If we set the crystal axis (c-axis) parallel to one bond (c), another in-plane bond (a) forms a $\sim 109.5^\circ$ angle with this c-axis. In perfect tetrahedra, $c=a$. However, the different stacking sequence of SiC layers change the equilibrium of electron structure which results in an elongated (c) bond for hexagonal SiC polytypes [30].

The common commercially used SiC polytypes are 3C, 4H, and 6H-SiC. 3C-SiC has cubic close-packed (fcc) crystal structure and 2H-SiC has hexagonal close-packed (hcp) structure. The stacking of 3C, 2H, 4H and 6H-SiC is shown in figure 1.3. Polytypes are often characterized by hexagonality, the fraction of local hexagonal crystal environment in the entire crystal structure, which is an important parameter influencing physical properties of SiC [31]. Carbon and silicon layers in 4H-SiC stack in ABCB pattern. 4H-SiC has half layers of quasi-hexagonal environment

and 50% hexagonality. Quasi-hexagonal (h) sites and quasi-cubic (k) lattice sites occur when silicon-carbon bilayers alternate between 2H-SiC and 3C-SiC as shown in the left side of figure 1.4. A particular bilayer experiences a different crystal field depending on whether it sees itself in hexagonal or cubic environment, considering the nearest neighbors.

1.4 Divacancies ($V_C V_{Si}$) in SiC as promising qubits

As its name suggests, a single divacancy defect consists of double vacancies at neighbor carbon and silicon sites. Depending on the locations of each vacancy, either h or k site, there are 4 combinations of a divacancy defect shown in the right side of figure 1.4. They are labeled as c-axis divacancies hh (PL1) kk (PL2) and basal (off-axis) divacancies hk (PL3) and kh (PL4). In this thesis, divacancies refer neutrally charged divacancies ($[V_C V_{Si}]^0$).

The quantum potential of divacancy defects was discovered initially by Koehl et al. [32]. This work demonstrated optically detected magnetic resonance (ODMR) and coherent spin polarization of ensemble divacancies. The ground spin state of divacancies can be initialized by a pulse of light and coherently manipulated by microwave pulses. The Ramsey (T_2^*) and Hahn echo (T_2) microwave pulse sequences were applied to measure spin decoherence characteristics. T_2^* characterizes the decoherence due to all sources, inhomogeneity of magnetic field within proximity and random spin-spin interactions. T_2 measurements add another pi pulse in the middle of the Ramsey sequence to cancel out the near DC magnetic field inhomogeneity, so T_2 is mainly related to decoherence due to random spin-spin interactions. The ensemble inhomogeneous spin coherence time T_2^* is $\sim 1.5 \mu s$ for basal divacancies at 20K and ~ 200 ns for c-axis divacancies at 200K. The ensemble Hahn-echo homogeneous spin coherence time T_2 is $\sim 200 \mu s$ for basal divacancies at 20K and $\sim 250 \mu s$ for c-axis divacancies at 200K. Later Christle et al. [33] investigated more on single divacancy properties. T_2^* of single divacancy is 1 - 5 μs at 20 K, similar to ensemble divacancies. T_2 of single PL2 divacancy is 1.2 ms at 20K, which is comparable to that of a NV center [33]. Considering that these results were measured on naturally isotopic 4H-SiC sample (including paramagnetic nuclear spin species ^{13}C 1.1%, ^{29}Si 4.7%), it is one of the longest Hahn-echo coherence time of an electron spin in solid state crystals [34]. The typical Rabi oscillation period is 0.3 μs [33], which suggests there can be ~ 4000 qubit polarization operations before the qubit information is erased by decoherence. This satisfies the practical requirement of fast single qubit operation with high fidelity.

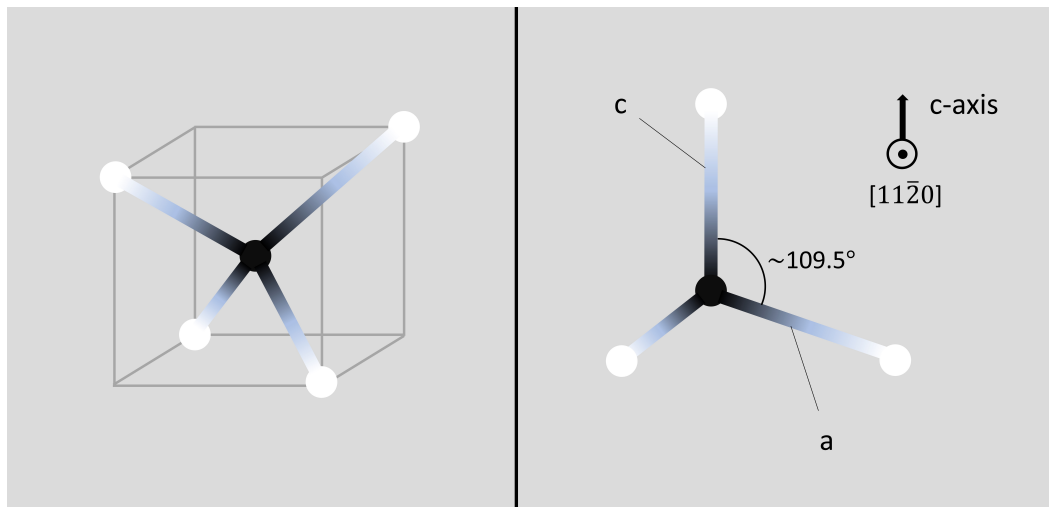


Figure 1.2: Left: the smallest periodic component of the SiC unit cell. The center black sphere shows a Si (C) atom and the white spheres show C (Si) atom. Right: The SiC ideal tetrahedral component viewed in the plane that is parallel to connected straight line connecting two nearest atoms of same kind ($11\bar{2}0$ plane).

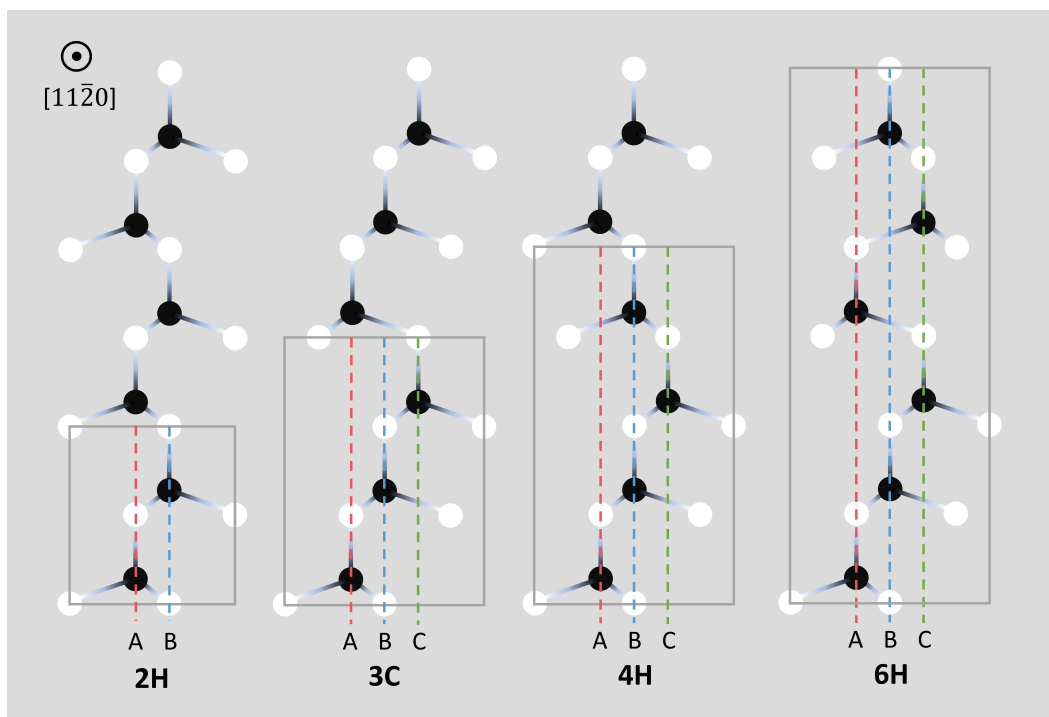


Figure 1.3: 2H, 3C, 4H and 6H-SiC stacking structure viewed in the $11\bar{2}0$ plane. The gray frame shows the unit cell of each structure.

1.5 Coupling optical defects to cavities

Optical quantum networks using solid state qubits require quantum information transmitted by photons to be stored for processing at the end nodes. In free space,

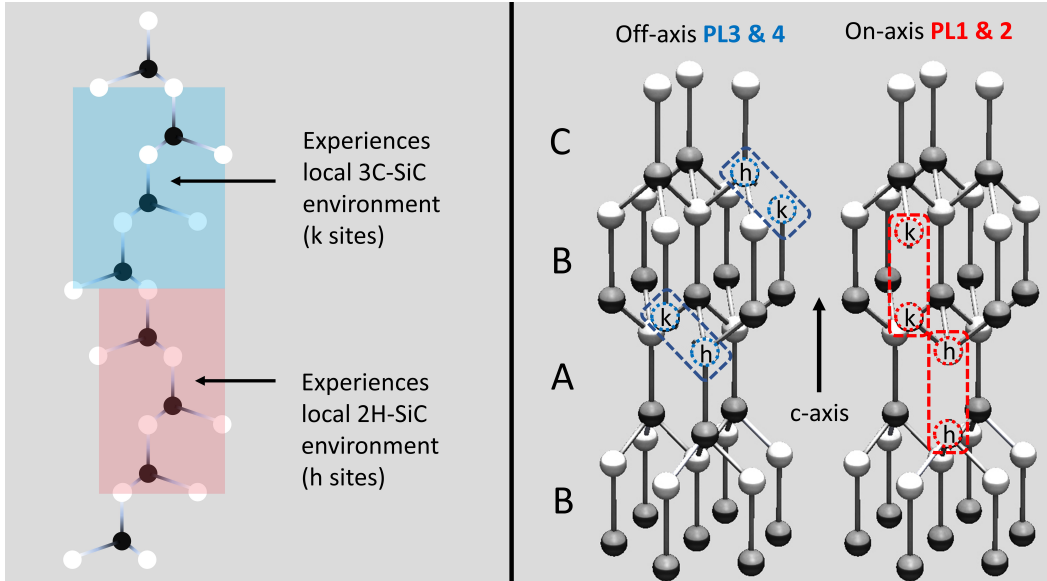


Figure 1.4: Left: Local hexagonal (2H-SiC) or cubic (3C-SiC) environment changes crystal field on atoms in bilayers of 4H-SiC. Right: 3D view of 4H-SiC crystal structure with 4 possible divacancy configuration.

the interaction or absorption cross section between atoms and photons is very small and it is hard to deterministically transfer quantum information between them with time much shorter than the time it can be preserved (atomic coherence time) [35]. Placing optically addressable solid state qubits in an optical cavity enhances the interaction rate between the qubit and the photon because the cavity traps the photon for a longer time and also confines it thus increasing the electric field corresponding to a single photon. This significantly boosts the light-matter interaction and is necessary for deterministic photon-qubit interaction. The cavity-qubit coupling is characterized by the g parameter which scales as $\frac{1}{\sqrt{V}}$, where V is mode volume of the cavity.

$$V = \frac{\int d^3\mathbf{r} \epsilon(\mathbf{r}) |\mathbf{E}(\mathbf{r})|^2}{\epsilon(\mathbf{r}_{max}) |\mathbf{E}(\mathbf{r}_{max})|^2} \quad (1.3)$$

The system composed of a qubit coupled to a cavity is characterized by the cooperativity parameter. A cooperativity greater than one means that the interaction occurs mainly between the atom and the photon trapped in the cavity before other sources of decoherence become dominant.

There are different types of optical cavities such as Fabry-Perot cavities, microspheres [36], whispering-gallery mode resonators [37], ring resonators [27], photonic crystals [38], etc. Ring resonators are easier to fabricate than photonic crystal

but have large mode volume. Photonic crystals can often achieve less than unit mode volume.

Cavities have the important role to enhance emission of solid state qubits for entanglement generation in QKD application. The state of the art entanglement generation rate using NV centers is 40 Hz [39]. The time to generate quantum entanglement compared to the spin decoherence time indicates how many multiple quantum network links can be maintained. Currently it is on the order of 1 and it needs to be much larger than 1 to reach practical level. Coupling coherent photoluminescence of qubits to optical cavities can greatly reduce its spontaneous emission rate by Purcell enhancement [40], can enhance the emission of a particular transition of interest, and enables better coupling into optical channels like optical fibers, which leads to a significant increase in the entanglement generation rate.

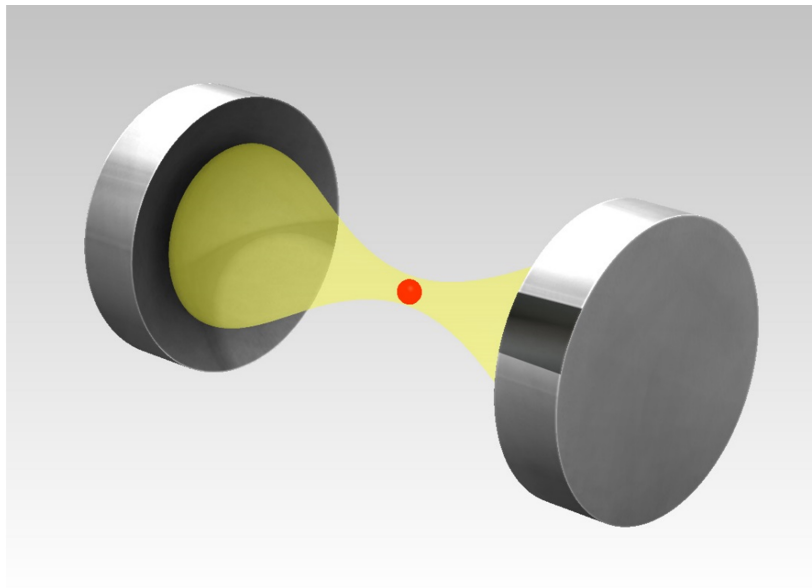


Figure 1.5: Impression of atoms interacting with light in a Fabry-Perot cavity.

Chapter 2

PHOTOLUMINESCENCE OF DEFECTS AND IMPURITIES IN SiC

2.1 Divacancies in 4H-SiC

Divacancies have 4 different configurations in the crystal lattice as shown in figure 2.1. They are associated with 4 different zero-phonon line (ZPL) labeled as PL1-4 shown in 2.2. ZPL emissions correspond to pure electronic transitions and often are observed with phonon-side-band (PSB) emission at higher wavelength that are phonon mediated transitions. As described in section 1.3, 4H-SiC has an elongated c-axis bonds. This makes a tetrahedron with one elongated bond parallel to c-axis with three identical bonds. If two adjacent defects occupy lattice sites parallel to c-axis, 120° rotations around c-axis still gives identical crystal configuration. c-axis divacancies have C_{3v} symmetry. If two adjacent defects occupy sites that are not parallel to c-axis, out of 3 neighboring bonds of each defect, one neighboring bond corresponds to an elongated bond and a rotational symmetry is removed. Only reflection against the plane that is parallel to c-axis and to the two defect bond makes the crystal unchanged. Basal divacancies have $C_{1h}(C_s)$ symmetry.

A single neutrally charged divacancy has 6 active electrons, 3 from nearby carbons and 3 from nearby silicons. From molecular orbital theory and ab initio density functional calculations, electrons in C_{3v} symmetry occupy orbital states $a_1^2 a_1^2 e^2$, which generates orbital singlet spin triplet 3A_2 , orbital doublet spin singlet 1E , and orbital/spin singlet 1A_1 in the order of the lowest energy level first [41–43]. The next excited state is $a_1^2 a_1^1 e^3$, which generates 3E and 1E levels. ZPL of c-axis divacancies (PL1,2) is associated with spin allowed transitions $^3E \rightarrow ^3A_2$ [44]. In reduced C_{1h} symmetry, E level splits into A' and A'' levels. ZPL of basal divacancies (PL3,4) is associated with $^3A' \rightarrow ^3A''$ [45]. Due to the fully allowed transition, the optical lifetime of the excited state of PL1-4 divacancies is relatively short, ~15 ns[46]. The energy diagram for c-axis and basal divacancies is shown in figure 2.3. Two spin singlet states lying between spin triplet excited and ground state of ZPL transition are coupled to spin triplet states with spin orbit coupling. Intersystem crossing between excited spin triplet state to singlet and then to ground spin triplet state is considered as main cause of spin dependent luminescence observed in magnetic

resonance (3.1)[47]. The Debye-Waller factor, the fraction of emission in ZPL out of the total emission is only $\sim 5\%$ [33].

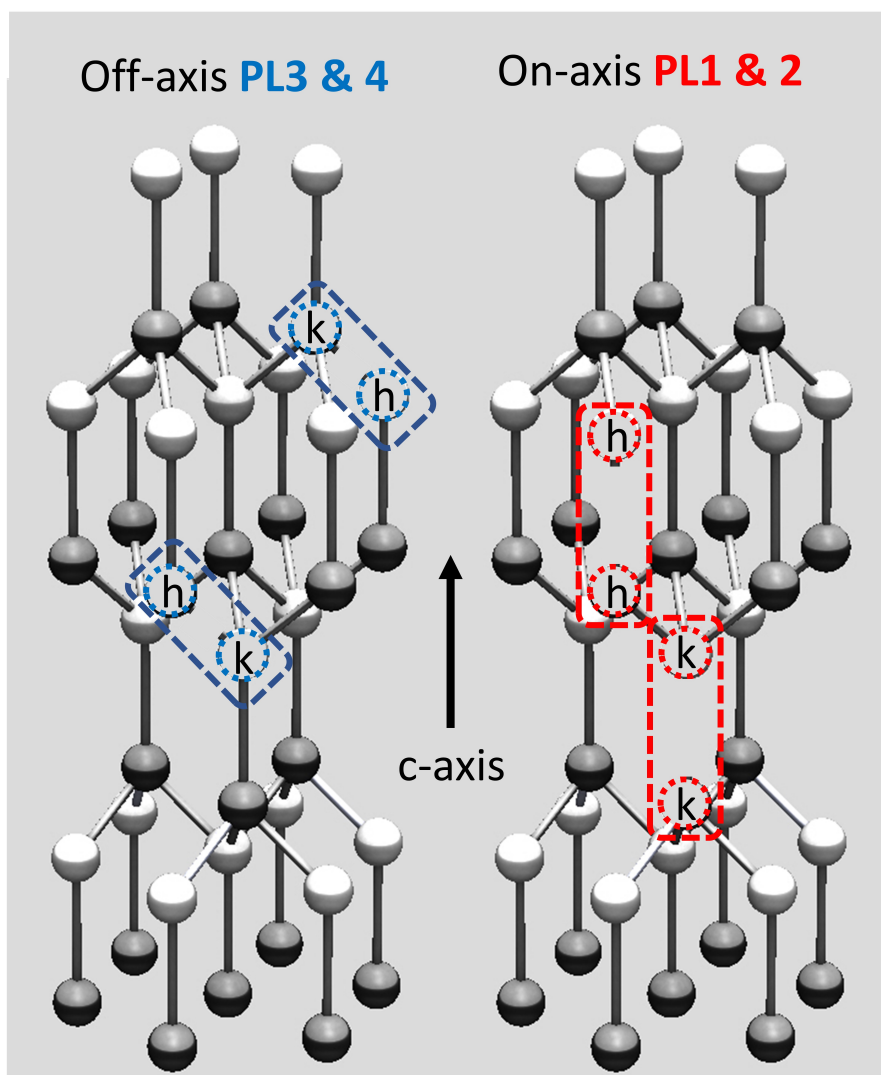


Figure 2.1: 4 types of divacancies that occupy different carbon/silicon lattice sites.

2.2 Cr^{4+} ions in 4H, 6H-SiC

Cr^{4+} ions show different ZPL depending on the substitutional locations of Cr ions in SiC. As mentioned in 1.3, 4H-SiC has 2 inequivalent lattice sites (h) and (k) that experience different crystal field. 6H-SiC have 3 of those. For 4H-SiC, Cr_A corresponds to Cr ions occupying quasi-cubic (k) sites with T_d symmetry that emit ZPL observable at ~ 1070 nm. Cr_C corresponds to those at hexagonal sites (h) with ZPL observable at ~ 1042 nm [48]. Symmetry of Cr_C is reduced to C_{3v} due to

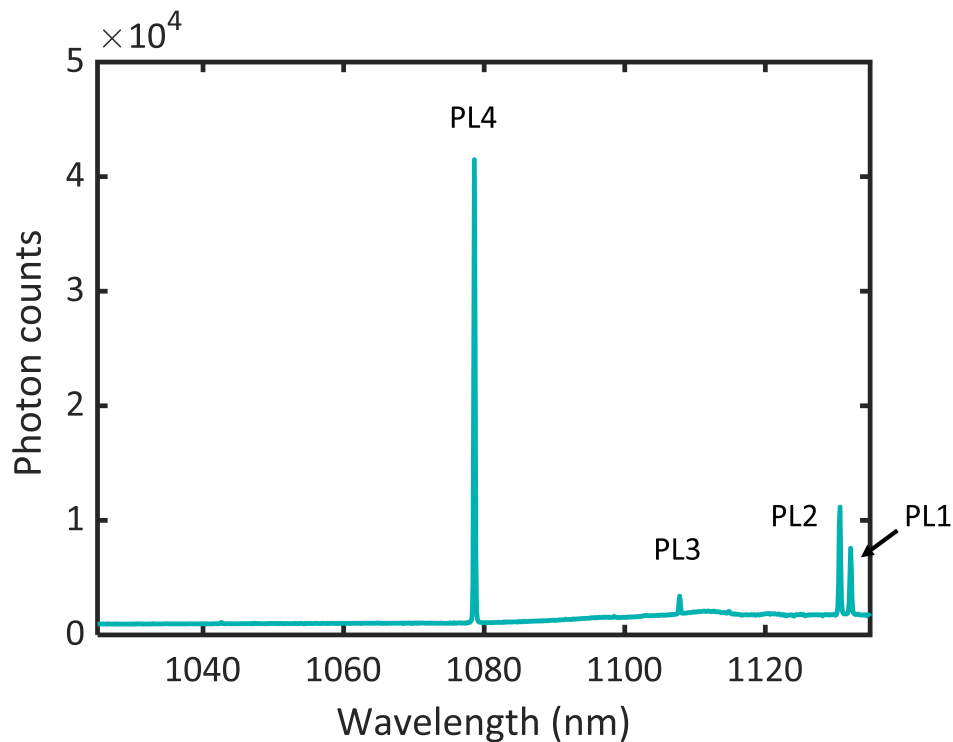


Figure 2.2: Photoluminescence of divacancies in a HPSI 4H-SiC sample excited by 780nm laser at 8.4 K.

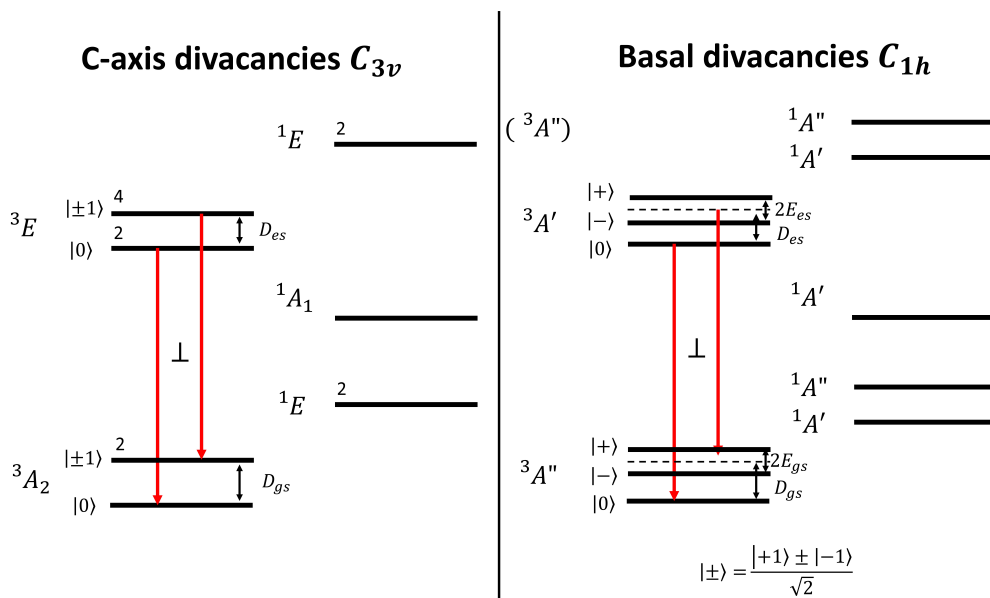


Figure 2.3: c-axis and basal divacancy energy level structure in 4H-SiC for C_{3v} and C_{1h} symmetry. Marks next to the red arrows specify the polarization of electric field with respect to c-axis for electric dipole allowed transitions.

elongated bond in the direction of c-axis as mentioned in 1.3. ZPL of Cr ions with intrinsic divacancies in Cr implanted HPSI 4H-SiC is shown in figure 2.4. Higher resolution ZPL of Cr^{4+} in 4H and 6H-SiC is shown in figure 2.5. Cr^{4+} in 6H-SiC were doped during the crystal growth process and ZPL peaks are much sharper than those in 4H-SiC due to less sample damage.

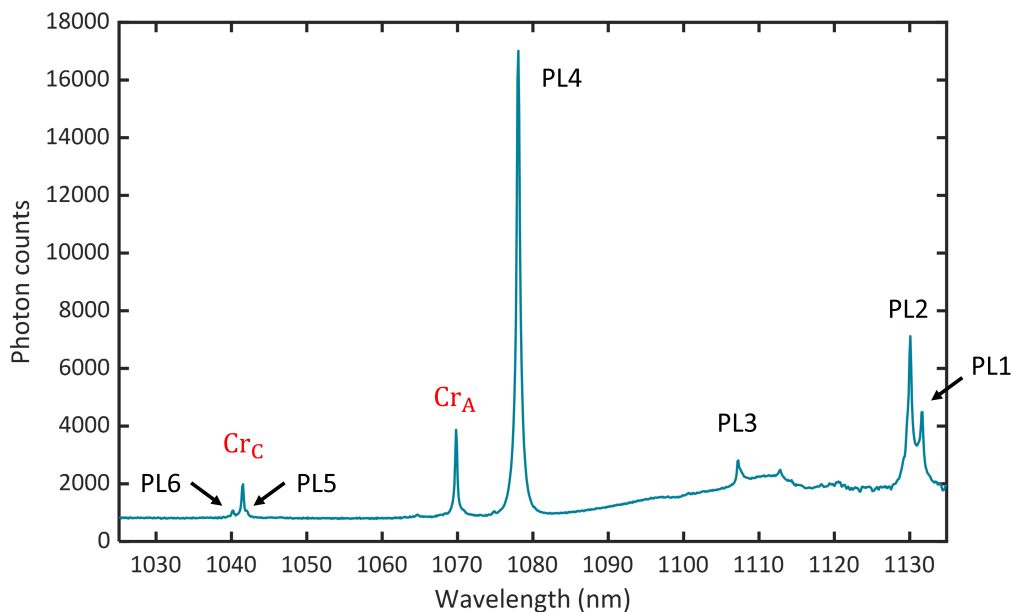


Figure 2.4: Photoluminescence of Cr ions and divacancies in a Cr implanted 4H-SiC sample excited by 780nm laser at 8.6 K.

The electron configuration for Cr^{4+} is 2 electrons in 3d shell ($3d^2$). Using group theory [49–51], we can determine the ground state and other existing states of free ions. For free ions having $3d^2$ configuration, the ground state is 3F , where left superscript denotes spin multiplicity $2S+1$ (S : total spin angular momentum). The next excited state depends on how much crystal field the ions feel in the crystal and the energy of taking each state changes according to the field strength. Group theory can determine how states of free spherical ions split when the symmetry is lowered with crystal field. In tetrahedral T_d symmetry, ${}^3F \rightarrow {}^3A_2 + {}^3T_1 + {}^3T_2$ as generating methods described in section 9.3 of Cotton [51]. A(B), E and T are Mulliken symbol that means 1, 2 and 3-dimensional irreducible representations of certain symmetry group, where the dimension corresponds to orbital degeneracy of states. For example, 3T_2 means orbital triplet and spin triplet, 9 states in total.

To know which of these is ground state and the next excited state, Racah parameters B,C and crystal field splitting parameter Dq needs to be measured based on

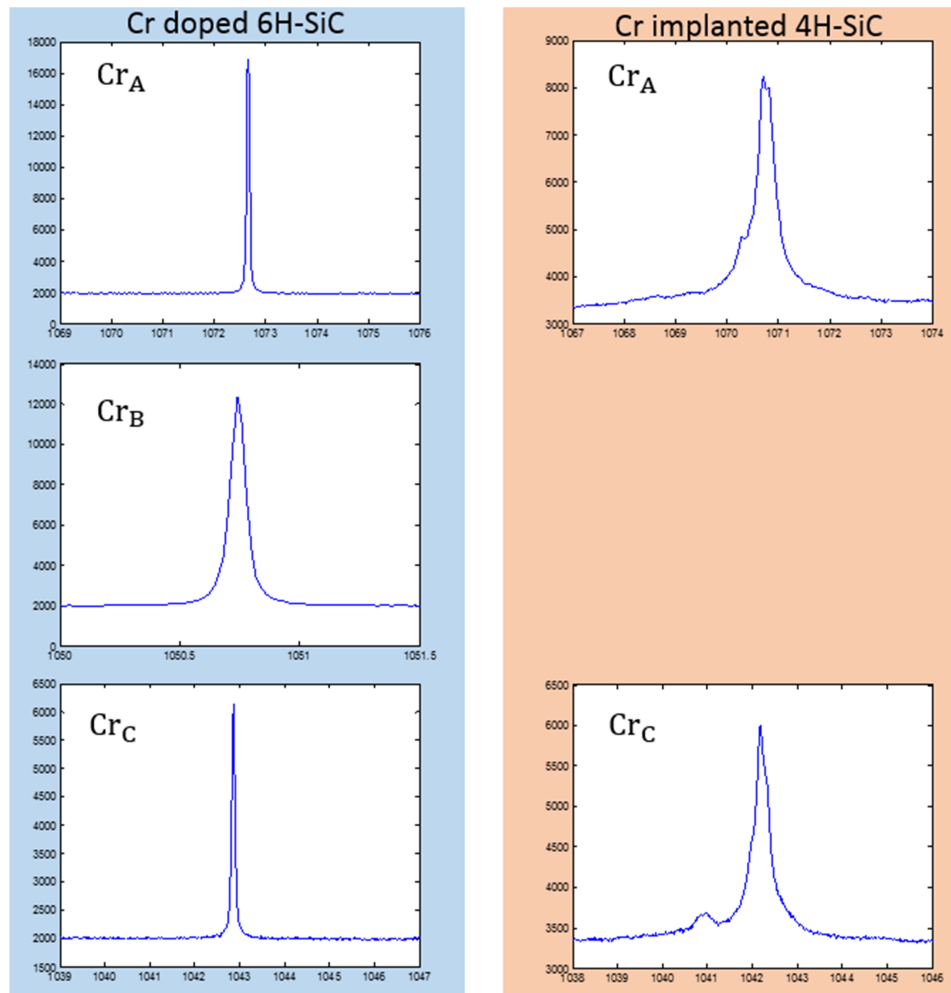


Figure 2.5: Photoluminescence of Cr ions in 4H-SiC and 6H-SiC samples in better resolution at liquid nitrogen temperature (80 K)

spectroscopy experiments. Derived parameters combined with Tanabe-Sugano formalism are often used to show the summary of energy of states vs. crystal field for complex metal ions [52]. From Tanabe-Sugano diagram for Cr^{4+} we can determine its ground state to be ${}^3A_2(\text{F})$ and the next excited state to be either ${}^3T_2(\text{F})$ or ${}^1E(\text{D})$ [53, 54]. Zeeman splitting measurements were performed to conclude the next excited state is actually 1E because each ZPL of spin triplet component of 3A_2 only splits to doublet excluding the possibility of 3T_2 with $S=1$ [48]. Cr^{4+} is in relatively high field system for 4H and 6H-SiC. ZPL of Cr^{4+} is associated with transition ${}^1E \rightarrow {}^3A_2$.

The energy diagram of Cr^{4+} ions is shown in figure 2.6. Cr_A with T_d symmetry and Cr_C with C_{3v} symmetry theoretically has the same energy level degeneracy when only the crystal field is considered. With spin orbit coupling in C_{3v} symmetry,

ground state $m_s = \pm 1$ states (Γ_3) and $m_s = 0$ become non degenerate. The electric dipole selection rule is shown next to red arrows. ZPL comes from spin forbidden but orbitally allowed transition.

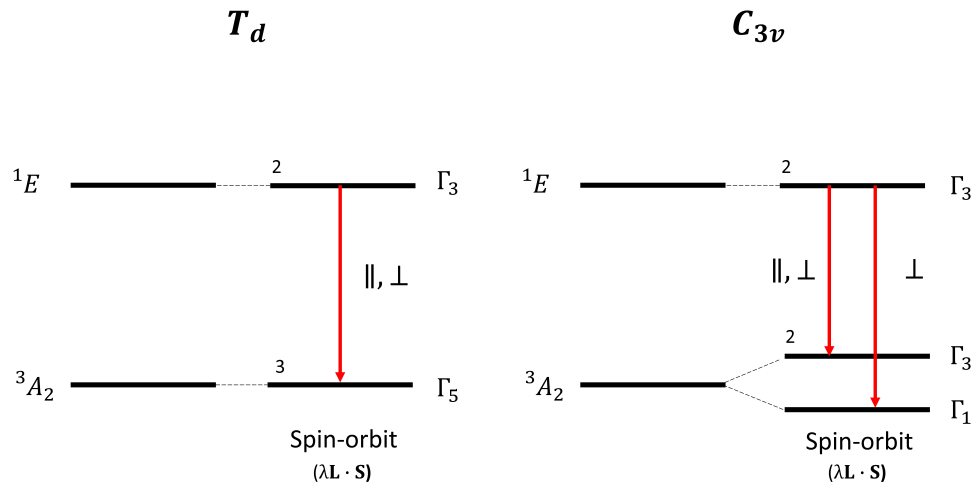


Figure 2.6: Cr^{4+} energy level structure in 4H and 6H-SiC for T_d and C_{3v} symmetry. ZPL of Cr^{4+} is associated with the transition ${}^1E \rightarrow {}^3A_2$. The number at left on level bars denotes state degeneracy and Γ specifies the irreducible representation of corresponding symmetry group. Marks next to the red arrows specify the polarization of electric field with respect to c-axis for electric dipole allowed transitions.

The lifetime of Cr^{4+} ZPL is in the order of 10 - 100 μs depending on the doping condition. The relatively long optical lifetime is expected for spin forbidden transitions that require spin flips. The photoluminescence decay profile from the excited state to the ground state can be measured by accumulating the timing of each emitted photon after excitation, expressed by $I(t) = I_o \exp(-t/\tau)$. τ is the optical lifetime and I_o is the photon counts right after the excitation in the first time bin. The PL decay curve of the lifetime measurement is shown in figure 2.7. The goodness of the fit was assessed by the zero offset and symmetry of the residual of the fit in figure 2.8. The table 2.9 shows the measured lifetime on implanted 4H-SiC samples (originally vanadium doped SI or highly purified SI wafer) and on doped 6H-SiC samples. There is not much difference in lifetime between Cr ions at different sites. At LHe temperature, Cr ions in 6H-SiC have lifetime 150 μs that is close to the values observed in doped 4H-SiC [55]. This 6H-SiC is expected to have the least damage and longest lifetime in the crystal compared to other 4H-SiC samples.

The inhomogeneous spin coherence time T_2^* of Cr^{4+} in 4H-SiC was recently mea-

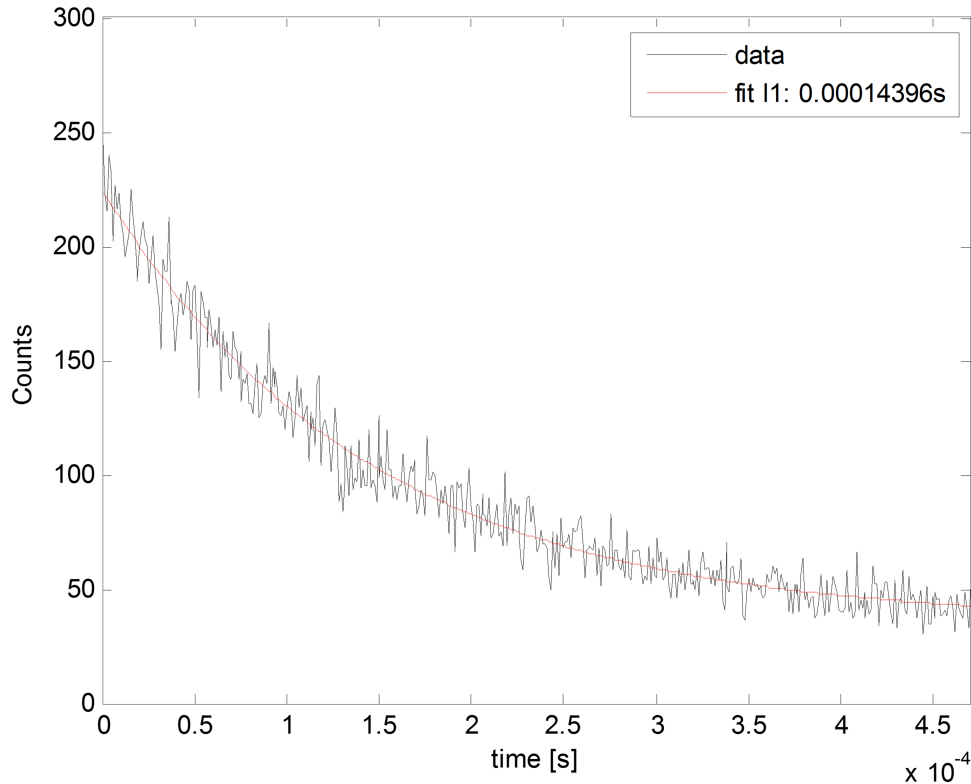


Figure 2.7: Optical lifetime measurement of Cr^{4+} ions in doped 6H-SiC at liquid helium temperature. The fitting function is $I_0 \exp(-t/\tau)$ and reveals optical lifetime of $144 \mu\text{s}$.

sured to be 37 ns. [55]. This result was published at the same period when I was looking into optical properties of Cr^{4+} ZPL. Due to this short coherence time, divacancies are more promising candidates as qubits so we will focus on them in later chapters.

2.3 Other color centers

Besides the previous divacancies and Cr ions I discussed, I also measured optical spectra and looked at some other color centers such as Vanadium, Molybdenum ions in SiC and Cu in Si. In this section, they are briefly reviewed.

V^{4+} ions in 4H-SiC

Conventionally, vanadium is doped in SiC as minority carrier lifetime killer to create semi insulating SiC wafer [56]. Depending on the position of the Fermi level, vanadium ions exist in either V^{3+} , V^{4+} , V^{5+} form [57][58]. In our semi insulating 4H-SiC samples, V^{4+} ions ZPL was observed as shown in figure 2.10. ZPL associated with (h) sites is labeled as α lines and can be observed around

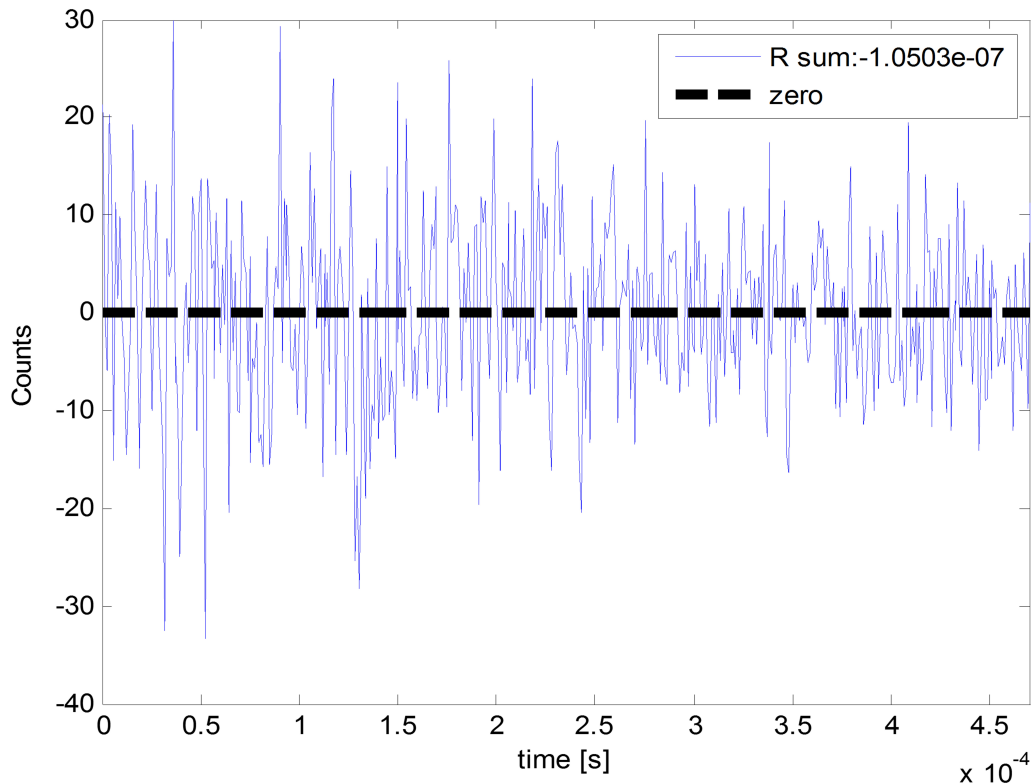


Figure 2.8: Optical lifetime measurement fitting residual shows the goodness of fitting with single exponential $I_0 \exp(-t/\tau)$.

wavelength 1280 nm. ZPL associated with (k) sites is labeled as β lines and can be observed around wavelength 1335 nm [59].

The energy level of V^{4+} is shown in figure 2.11. V^{4+} has $3d^1$ electronic configuration and single electron doesn't experience repulsion, which is the simplest case considering energy levels. In Russel-Saunders coupling scheme, a free V^{4+} ion takes only one energy level 2D . Under tetrahedral field, it splits to the ground state 2E and the excited state 2T_2 . In trigonal field, 2T_2 further splits to 2E and 2A_1 states. With spin-orbit coupling, all states split into Kramers doublets. In the spectroscopy setup, we illuminated our sample with polarization perpendicular to c-axis and the middle transitions in four α lines are expected to be stronger due to orbitally allowed transitions.

The spin relaxation time T_1 around 4 K is $1 \mu s$ or shorter depending on lattice sites[60].

Table 1 Cr Lifetime on implanted 4H-SiC

Temperature	Sample	Lifetime τ (us)	
		Cr_a	Cr_c
RT	HPSI	42.1	37.2
	SI	13.0	8.19
LN T	HPSI	49.8	53.0
	SI	26.6	26.0
LHe T	HPSI	48.9	52.5
	SI	30.5	40.1

Table 2 Cr Lifetime on doped 6H-SiC

Temperature	Lifetime τ (us)		
	Cr_A	Cr_B	Cr_C
RT	50.0	40.1	27.5
LHe T	147	153	137

Figure 2.9: Summary of optical lifetime measurements of Cr^{4+} ions in implanted 4H-SiC and doped 6H-SiC samples at different temperature.

Mo⁵⁺ ions in 4H-SiC

Photoluminescence associated with Mo ions were observed in 4H-SiC around 1076 nm as shown in 2.12. The corresponding configuration of Mo ions in 4H-SiC can be either substitutional or asymmetric split vacancy [61] and different electric charge state, which have not been determined in previous works [62–64] until recent work using two laser spectroscopy under magnetic field [65]. The result indicates substitutional Mo⁵⁺ at (h) site due to ground state Lande g-factor anisotropy. Mo⁵⁺ has 4d¹ electronic configuration, which results in the same energy level structure with V⁴⁺ ions. The measured optical lifetime of excited state is 56 ns. The inhomogeneous spin coherence time T_2^* is 320 ns [65].

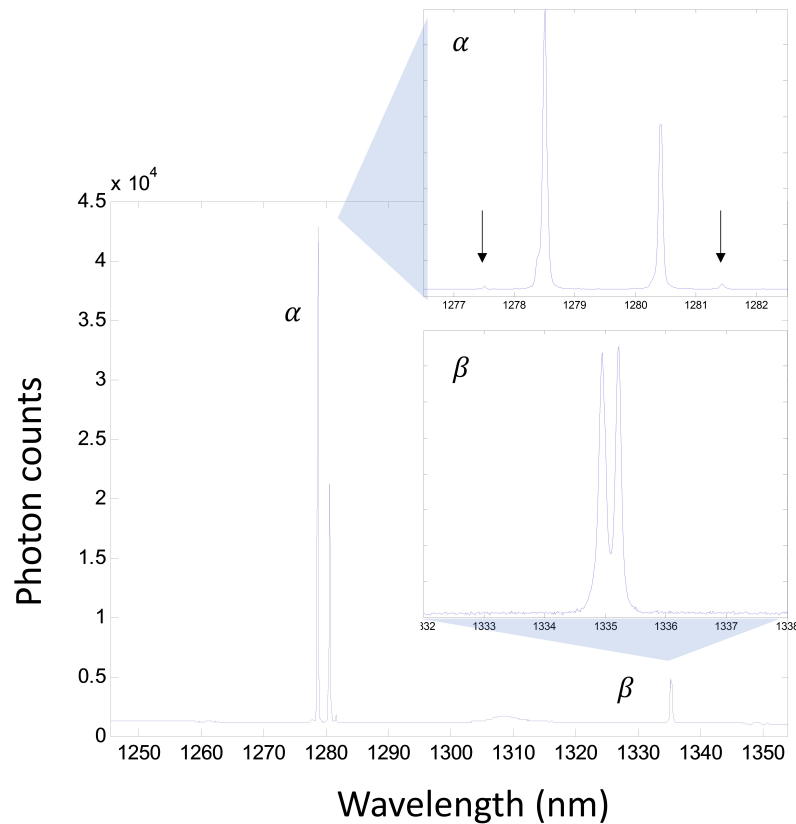


Figure 2.10: Photoluminescence of V ions in semi insulating 4H-SiC sample excited by 780 nm laser at liquid helium temperature.

Cu in Si

Cu in Si and exhibit bright and sharp photoluminescence around 1228 nm with optical lifetime 30 ns [66–68]. The PL spectra at different temperature are shown in figure 2.13 and 2.14. The spin relaxation or coherence time of these centers have not yet been investigated and the potential for qubits is still unknown.

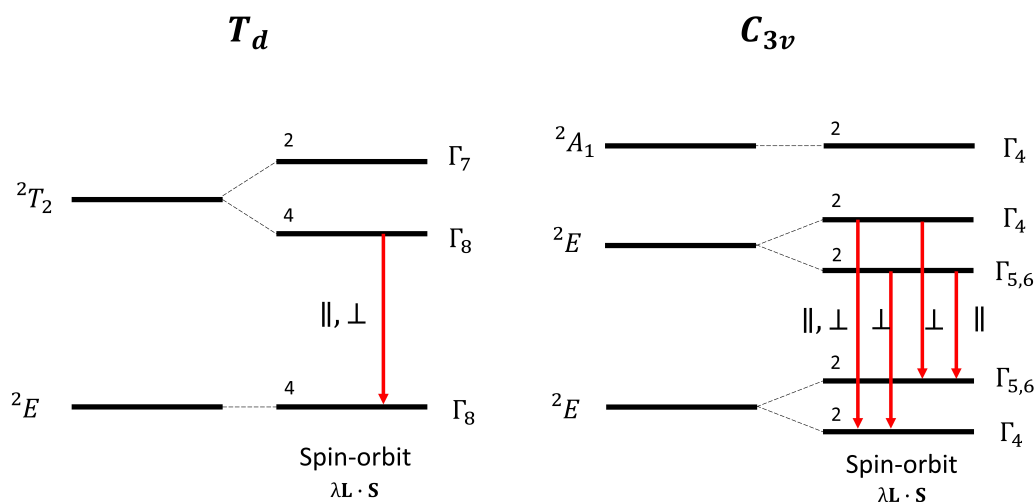


Figure 2.11: V^{4+} energy level structure in 4H-SiC for T_d and C_{3v} symmetry. ZPL of V^{4+} is associated with the transition ${}^2T_2 \rightarrow {}^2E$. The number at left on level bars denotes state degeneracy and Γ specifies irreducible representation of corresponding symmetry group. Marks next to red arrows specify polarization of electric field to c-axis for electric dipole allowed transitions.

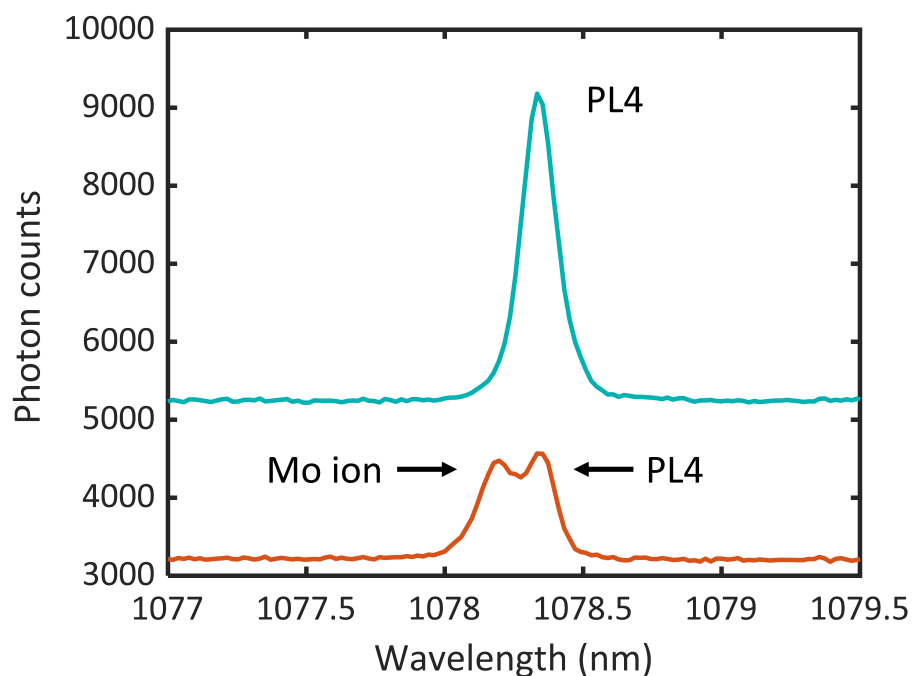


Figure 2.12: Photoluminescence of Mo^{5+} ions in implanted sample (orange) in comparison with PL4 divacancies in a HPSi sample (blue) excited by 780 nm laser at 8.6K

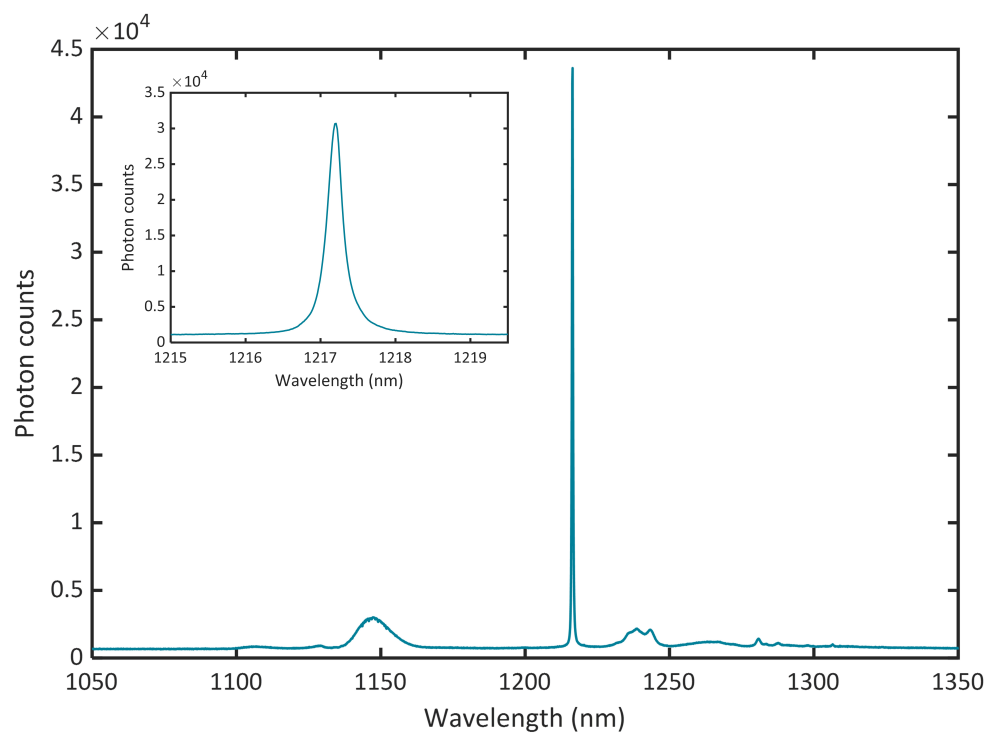


Figure 2.13: Photoluminescence of Cu ions in Cu implanted Si excited by 780 nm laser at 8.2K

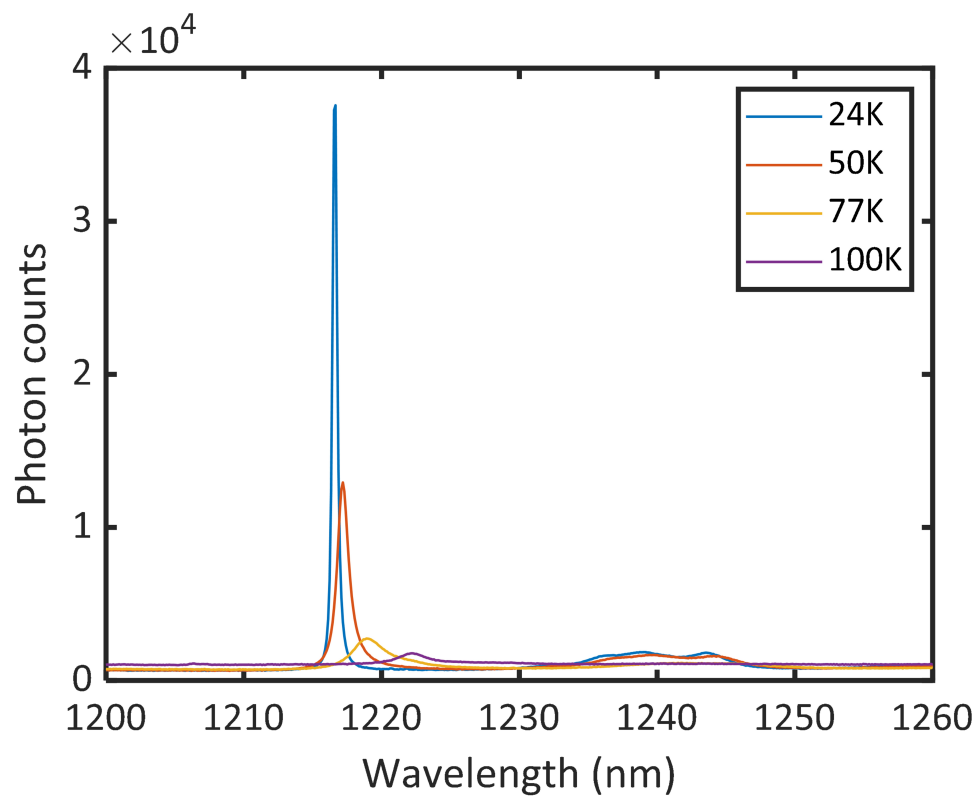


Figure 2.14: Photoluminescence of Cu ions in Cu implanted Si excited by 780 nm laser at different temperatures

Chapter 3

OPTICALLY DETECTED MAGNETIC RESONANCE OF DEFECTS IN 4H-SiC

3.1 Principles of ODMR

Optically detected magnetic resonance (ODMR) refers to optical readout of qubit spin states or optical polarization of spin states using microwave fields driving the resonance between different spin states. This effect is very useful in developing different optical quantum technologies. The signal of ODMR is the optical signal emitted by the optically addressable qubits in the ZPL or the phonon sidebands. Depending on the population ratio between different spin sublevels, the ZPL counts either increase or decrease. This contrast of ZPL counts gives information about spin polarization. For PL1 and 2 c-axis aligned divacancies in 4H-SiC, this is enabled by the non radiative decay path, so called intersystem crossing between the excited and ground triplet states [41, 44], with level structures similar to negatively charged nitrogen vacancy centers in diamond[43, 47, 69]. Microwaves are used to resonantly address different spin sublevels, which generates different optical emission intensity. A simplified energy level structure and ODMR mechanism for c-axis divacancies is shown in figure 3.1.

In the left side of the figure3.1, microwaves are off and divacancies are continuously excited non resonantly. Excited divacancies emit photoluminescence through spin conserving relaxation. The excited $m_s = \pm 1$ sublevels in excited states are more strongly coupled to singlet states that lie between the triplet states, which gives rise to non radiative relaxation. These singlet states are believed to be preferentially coupled to the ground $m_s = 0$ sublevel. Therefore continuous optical cycling between excited and ground triplet states will result in most divacancies populated in $m_s = 0$ sublevel. Because divacancies in excited $m_s = \pm 1$ sublevels have higher possibility to go through non radiative relaxation, there are less photon counts if more divacancies are populated in ground $m_s = 0$ sublevel. In the beginning of optical excitation/initialization, ZPL is darker as there are almost equal population in $m_s = 0$ and $m_s = \pm 1$ sublevel. However, continuous optical excitation will eventually achieve non- Boltzmann steady state with most spins to $m_s = 0$ and reach brighter ZPL emission.

In the right side of the figure, a microwave field is used to drive the spin transition. When the microwaves are on and the frequency is resonant with the energy gap between ground $m_s = 0$ and $m_s = \pm 1$ sublevels, the microwaves pump some of the population in the $m_s = \pm 1$ state, which leads to a change in the emitted photolumumescence. When the microwaves are not resonant with the spin transition there is no significant effect on the luminescence.

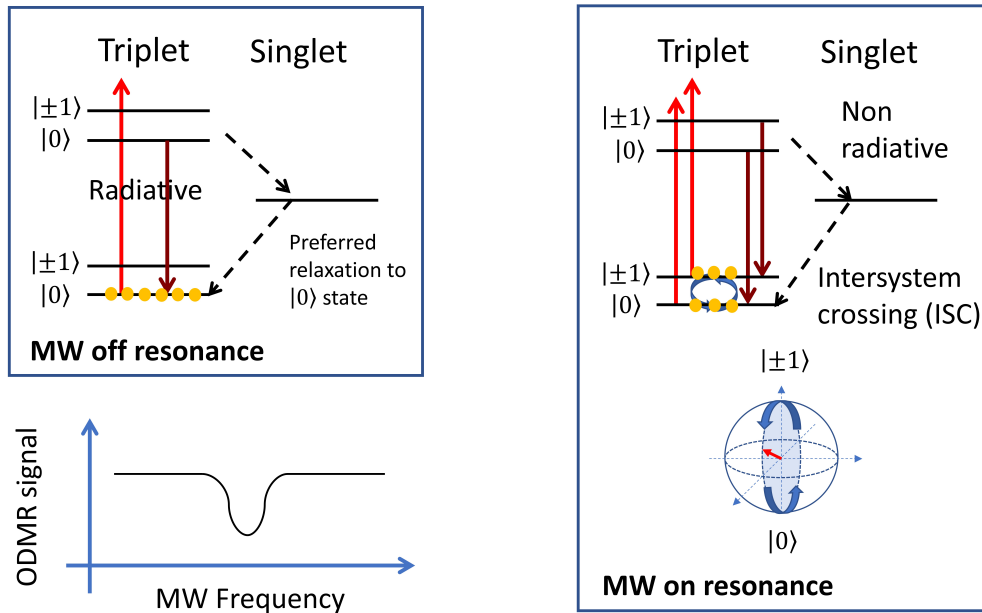


Figure 3.1: Spin population and ODMR signal change when microwave is on/off

3.2 ODMR setup

Our final ODMR setup uses a microwave (MW) line deposited on the SiC samples directly as shown in figure 3.2. The design was inspired from Koehl et al. [32] supplementary material. We glued a round PCB board around the copper cold finger and the gold MW lines (the design is shown in figure 3.2) were wire bonded to conductive segments on the board. Those segments were connected to an external SMA port with soldered wires (figure 3.3). The first version with a single wire put across the samples didn't provide good attachment to samples and the wire was prone to separation from the sample surface. With higher power MW applied in cryostat, the wire often moved away or across samples due to heat expansion resulting in weak MW drive amplitude on sample surface.

The ODMR signal shown in our results was defined by the equation shown in figure

3.4. ZPL of each divacancies was spectrally filtered by adjustable long pass and short pass filters. ODMR is the contrast of filtered ZPL with MW applied and ZPL without MW applied. As you can see in the typical spectrum of Cr implanted 4H-SiC or undoped 4H-SiC, PL4 is bright and its phonon side band counts of PL4 is comparable to ZPL of PL3, also lying on PL1 and PL2. This creates overlap of PL4 ODMR signal on PL1-3 ODMR signal that will be shown in the next section.

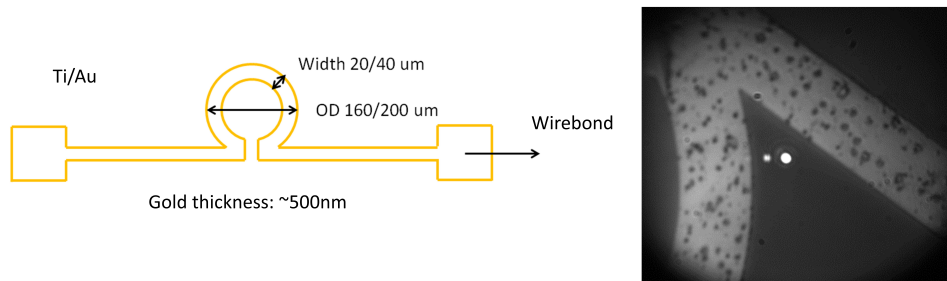


Figure 3.2: Schematic of the MW gold line deposited on a 4H-SiC sample. The right figure shows the image taken from CCD camera with 780nm excitation laser on.

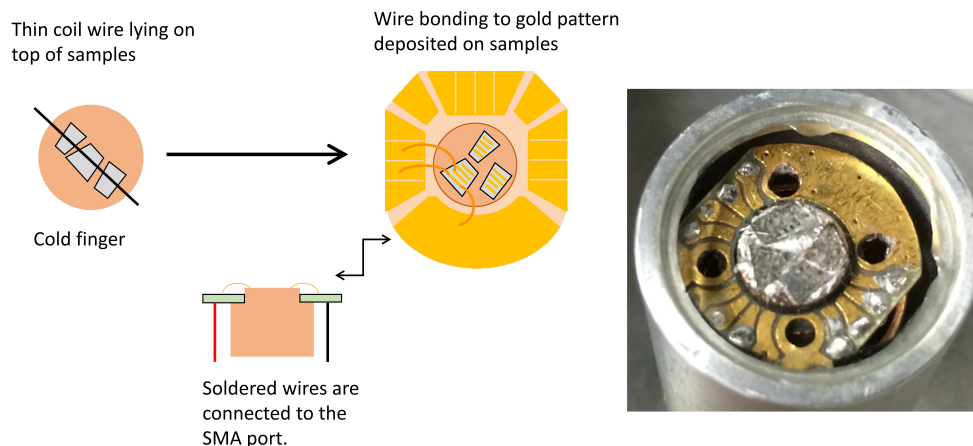


Figure 3.3: MW setup around samples. Initial setup with a single wire on samples is replaced with more robust method with wire bonding and gold line deposition directly on sample.

3.3 ODMR results on ensemble divacancies and on Cr ions

We observed similar ODMR signal to that shown in literature of divacancy ODMR [32]. The measurements were performed on highly purified semi insulating (HPSI)

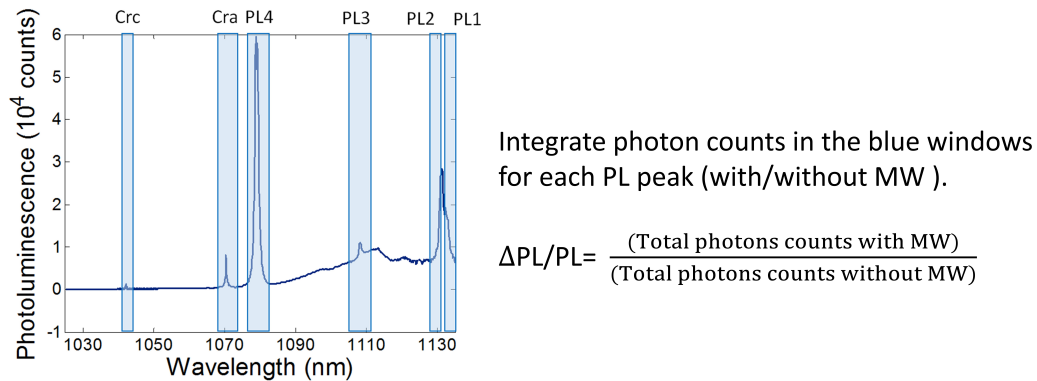


Figure 3.4: ODMR signal collection method

4H-SiC sample from CREE Inc without any post processing. Divacancies observed in this sample are incorporated intrinsically. Most of divacancies ODMR signal is in the range of 1.28-1.38 GHz. The comparison of our results (left) and the results from [32] (right) is shown in figure 3.5. Our ODMR signal peaks are generally broader than theirs, which suggests a power broadening effect considering that they used the same type of HPSI 4H-SiC samples. ODMR signal of PL3 at approximately 1.305 GHz is overlapped with background PSB ODMR signal of PL4. However PSB of PL4 on PL1 and PL2 ZPL is much smaller than their ZPL and there's no noticeable PL4 influence. Figure 3.6 shows a wide range of ODMR signals. A signal at 1.45 GHz is an artifact due to heating of the sample and change of the focus. You can see larger power broadening with larger MW power as shown in figure 3.7. The power label at the left side is the MW source power and this is amplified by 20dB through amplifier before MW is delivered to the sample gold lines.

ODMR measurements on Cr ions on Cr implanted 4H-SiC was attempted both with and without magnetic field. As zero field splitting parameter D of Cr_A and Cr_C was known to be < 1.2 GHz and ~ 6.0 GHz by Son et al. [48], we applied magnetic field to c-axis direction for 0.15 T, which gives expected ODMR signal around 1.7 GHz. We observed PL1 and PL2 ODMR at corresponding magnetic field calculated with $2g\mu_B B/h$ at around 2.75 and 2.78 GHz as shown in figure 3.8 but we didn't observe any ODMR signal from Cr_C with this continuous wave ODMR method.

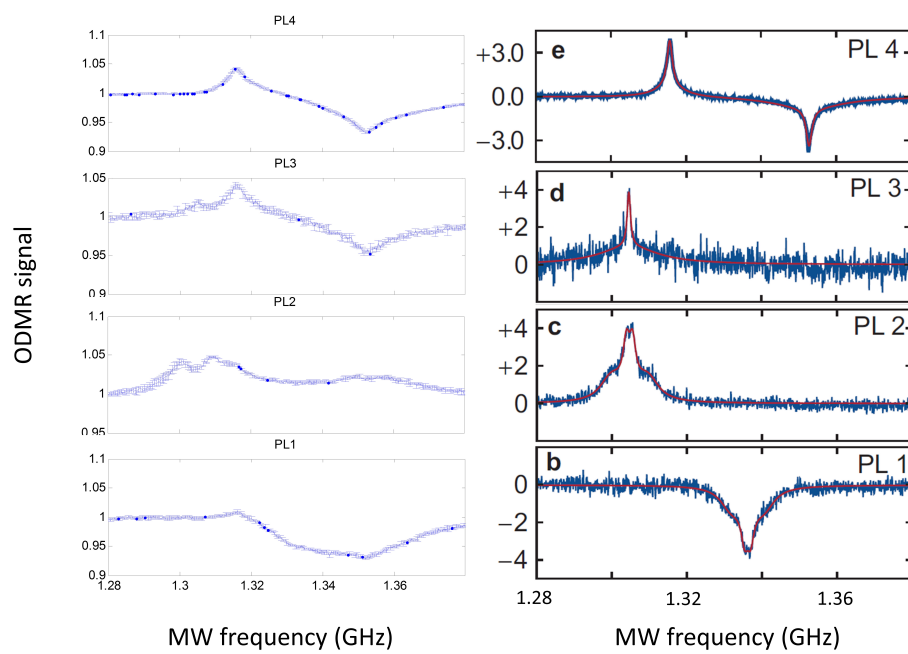


Figure 3.5: Our ODMR signal collected on undoped HPSI 4H-SiC at liquid helium temperature (~ 20 K) at left side. Right side shows results from Koehl et al. [32]

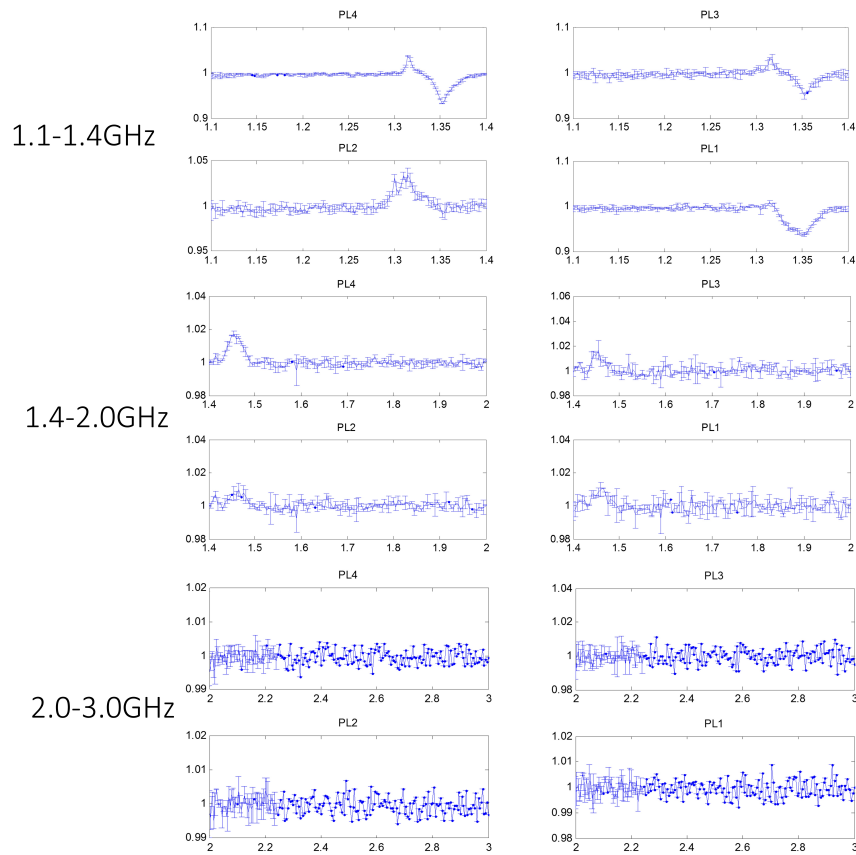


Figure 3.6: ODMR signal collected on undoped HPSI 4H-SiC at liquid helium temperature (~ 20 K) with wider MW sweep range.

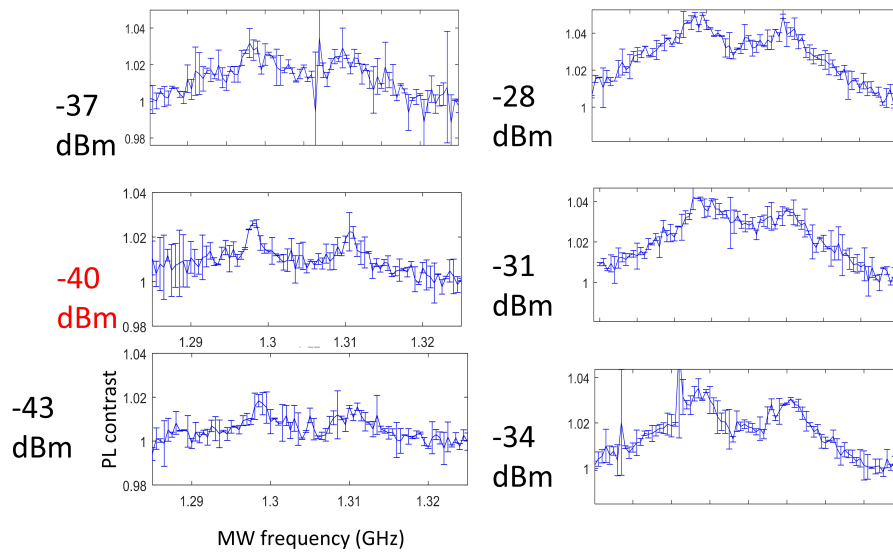


Figure 3.7: Power broadening of ODMR signal of ensemble divacancies PL2

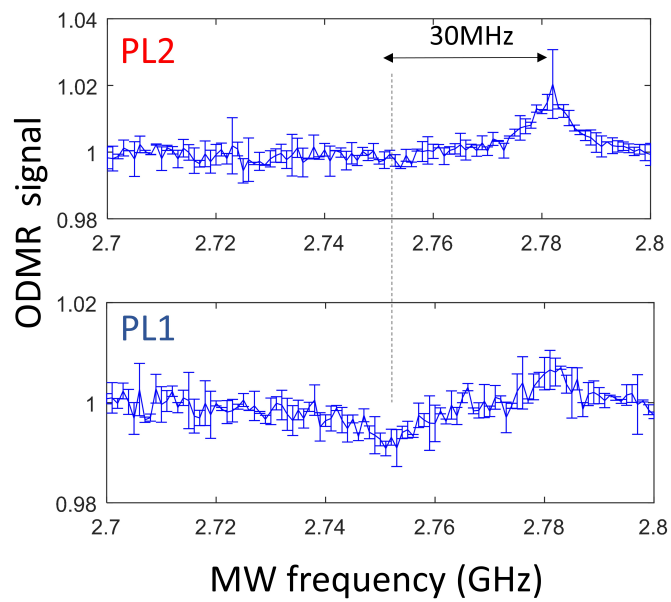


Figure 3.8: ODMR signal of PL1 and PL2 divacancies in Cr implanted 4H-SiC under 0.15 T at liquid nitrogen temperature.

Chapter 4

DESIGN AND SIMULATIONS OF PHOTONIC RESONATORS

This chapter explains why silicon is a good material for near IR wavelength photonic devices at low temperature. The basic theory of finite difference time domain (FDTD) simulations is explained. Then the entire FDTD simulation procedure is described, which is used to determine the parameters for Si ring resonators on SiC.

4.1 Silicon photonic devices for near IR wavelength

The emission of qubits can be improved by using scalable on-chip cavity devices that couple to the optical transition to generate lifetime limited emission and channel it into optical waveguides. One strategy to develop on-chip photonic devices is to fabricate them directly in the qubit host material. For this technique, it is required to start with thin membranes on a low refractive index substrate, or on a substrate that can be etched away or undercut. Even if some techniques exist to produce membranes, it is not always the case that these membranes can host high quality quantum emitters. Additionally, fabrication process often damages the material and leaves unwanted charges that degrades qubits' properties. For 4H-SiC, heteroepitaxial growth is not available and creating thin membranes is not straightforward. An alternative is to make hybrid devices in a high refractive index layer located on top of the substrate hosting the qubits, such that the emitters are coupled to the evanescent field. In my research project, we used a crystalline silicon (c-Si) hybrid platform of ring resonators and waveguides fabricated on top of SiC substrate shown in figure 4.1.

We want to choose the right device layer material for the hybrid platform. We can check if the material has large enough refractive index contrast to possibly confine light well and if it has minimal absorption for the wavelength range of interest. The intrinsic quality factor of the Si ring resonator surrounded by air is calculated for different temperature as shown in figure 4.2. This is calculated based on absorption

coefficient of Si [70, 71] and resonator theory [72, 73]:

$$a^2 = e^{-\alpha L} \quad (4.1)$$

$$FWHM = \frac{\Delta\theta\lambda_{res}^2}{\pi n_{eff}L - \lambda_{res}\Delta\theta} \quad (4.2)$$

$$\Delta\theta = \cos^{-1}\left(2 - \frac{1 + a^2|t_1|^2|t_2|^2}{2a|t_1||t_2|}\right) \quad (4.3)$$

a is single round amplitude transmission and α is absorption coefficient. L is the round trip length. t_1 and t_2 are self-coupling coefficient for two waveguides. λ_{res} is the resonant wavelength. n_{eff} is the effective refractive index. These intrinsic quality factor values correspond to silicon ring resonators with perfectly smooth surfaces (no scattering loss) with material absorption loss, characterized by a single round amplitude transmission a . Silicon has a bandgap at 1.11 eV (1120 nm wavelength of light) at 300K [74]. At lower temperature the bandgap decreases and silicon has less interband absorption. From the figure 4.2, at 1050 nm and 20K the intrinsic quality factor exceeds 10^8 . At this low temperature Si shows sufficient transparency to be used as a device layer coupling divacancy ZPLs ranging in the interval 1080-1130 nm.

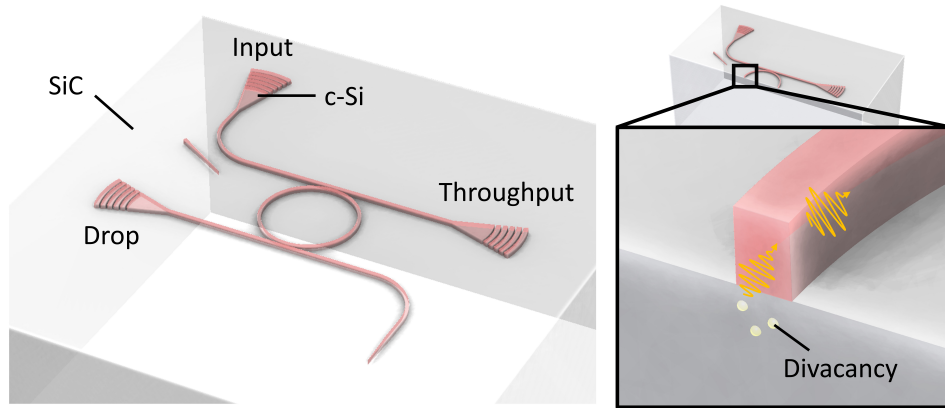


Figure 4.1: Left: c-Si ring resonator on 4H-SiC for spin-photon interfaces. c-Si is drawn in red, while the transparent part underneath is 4H-SiC. Right: Cross section showing the ring resonator near color centers in the 4H-SiC underneath it, that can couple to the evanescent field of the cavity.

4.2 Principles of finite-difference time-domain (FDTD) method

The finite-difference time-domain (FDTD) method is a systematic computational method for electromagnetic fields using the central difference approximation of

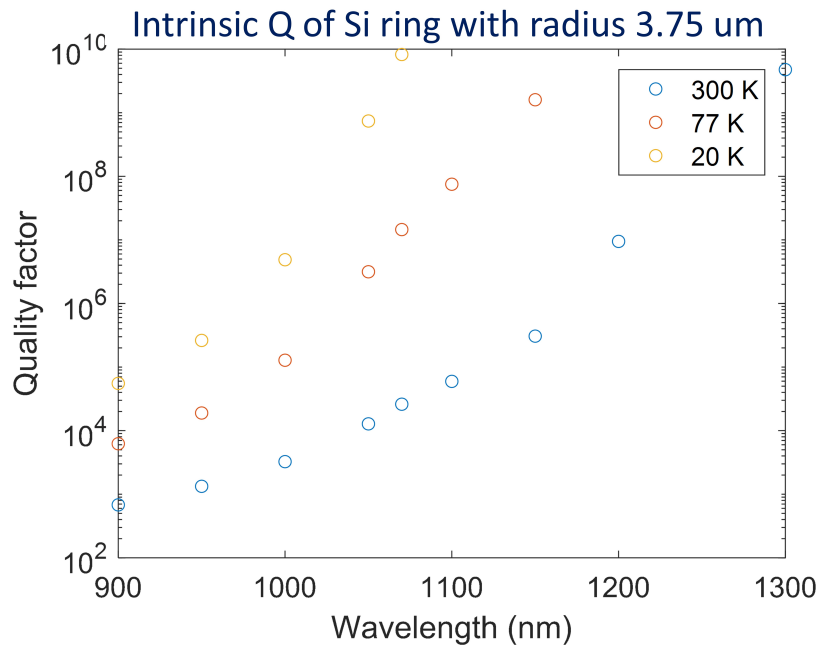


Figure 4.2: Intrinsic quality factor of Si ring resonator surrounded by air at different temperature.

coupled Maxwell's curl equations (Faraday's law and Ampere's law) [75]. Space and time is divided into grids, which is called Yee lattice to update the results of both electric and magnetic field at certain location/time to those of neighbor location/time. In an actual simulation, computation starts in a volume with finite grids in space at time zero and, using initial condition of electric or magnetic field, the field value at the neighbor grid in space at next time step will be calculated. This continues until all field values at that time step of interest are computed. Then time is incremented by one time step and the field calculation for the same region starts again.

If we consider an electromagnetic (EM) wave in isotropic media, the electric displacement field \mathbf{D} and auxiliary magnetic field \mathbf{H} are parallel to electric field \mathbf{E} and magnetic field \mathbf{B} accordingly.

$$\mathbf{D} = \varepsilon\mathbf{E} \quad (4.4)$$

$$\mathbf{B} = \mu\mathbf{H} \quad (4.5)$$

where ε is electric permittivity and μ is magnetic permeability. The Maxwell's curl

equations in isotropic media can be written as:

$$\nabla \times \mathbf{E} + \mu \frac{\partial \mathbf{H}}{\partial t} = 0 \quad (4.6)$$

$$\nabla \times \mathbf{H} - \varepsilon \frac{\partial \mathbf{E}}{\partial t} = \mathbf{J} \quad (4.7)$$

Each component of the electric field and auxiliary magnetic field is written,

$$\frac{\partial E_x}{\partial t} = \frac{1}{\varepsilon} \left(\frac{\partial H_z}{\partial y} - \frac{\partial H_y}{\partial z} - J_x \right) \quad (4.8)$$

$$\frac{\partial E_y}{\partial t} = \frac{1}{\varepsilon} \left(\frac{\partial H_x}{\partial z} - \frac{\partial H_z}{\partial x} - J_y \right) \quad (4.9)$$

$$\frac{\partial E_z}{\partial t} = \frac{1}{\varepsilon} \left(\frac{\partial H_y}{\partial x} - \frac{\partial H_x}{\partial y} - J_z \right) \quad (4.10)$$

$$\frac{\partial H_x}{\partial t} = \frac{1}{\mu} \left(\frac{\partial E_z}{\partial y} - \frac{\partial E_y}{\partial z} \right) \quad (4.11)$$

$$\frac{\partial H_y}{\partial t} = \frac{1}{\mu} \left(\frac{\partial E_x}{\partial z} - \frac{\partial E_z}{\partial x} \right) \quad (4.12)$$

$$\frac{\partial H_z}{\partial t} = \frac{1}{\mu} \left(\frac{\partial E_y}{\partial x} - \frac{\partial E_x}{\partial y} \right) \quad (4.13)$$

where \mathbf{J} is the electric current density. According to the Yee algorithm[75, 76], if we denote any function evaluated at a grid point in space and time with lattice increment $(\Delta x, \Delta y, \Delta z, \Delta t)$ in x, y, z and t coordinates,

$$u|_{i,j,k}^n = u(i\Delta x, j\Delta y, k\Delta z, n\Delta t) \quad (4.14)$$

the partial differential equations of time are approximated using centered finite difference expressions at a space point (i, j, k) :

$$\frac{\partial u|_{i,j,k}^n}{\partial t} = \frac{u|_{i,j,k}^{n+\frac{1}{2}} - u|_{i,j,k}^{n-\frac{1}{2}}}{\Delta t} + O[(\Delta t)^2] \quad (4.15)$$

Partial differential equations of space coordinates can be approximated in similar manner. As an example, using this approximation on equation 4.10, it can be written as following:

$$E_z|_{i,j,k}^{n+\frac{1}{2}} = \frac{\Delta t}{\varepsilon} \left(\frac{H_y|_{i+\frac{1}{2},j,k}^n - H_y|_{i-\frac{1}{2},j,k}^n}{\Delta x} - \frac{H_x|_{i,j+\frac{1}{2},k}^n - H_x|_{i,j-\frac{1}{2},k}^n}{\Delta y} - J_z|_{i,j,k}^n \right) + E_z|_{i,j,k}^{n-\frac{1}{2}} \quad (4.16)$$

As we can see from this equation, E_z is approximated by a combination of H_x and H_y at a half previous time step and E_z at the previous time step. Now we want to know how to approximate H_x and H_y using equations 4.11, 4.12, and 4.15.

$$H_x|_{i,j+\frac{1}{2},k}^n = \frac{\Delta t}{\varepsilon} \left(\frac{E_z|_{i,j+1,k}^{n-\frac{1}{2}} - E_z|_{i,j,k}^{n-\frac{1}{2}}}{\Delta y} - \frac{E_y|_{i,j+\frac{1}{2},k+\frac{1}{2}}^{n-\frac{1}{2}} - E_y|_{i,j+\frac{1}{2},k-\frac{1}{2}}^{n-\frac{1}{2}}}{\Delta z} \right) + H_x|_{i,j+\frac{1}{2},k}^{n-1} \quad (4.17)$$

$$H_y|_{i+\frac{1}{2},j,k}^n = \frac{\Delta t}{\varepsilon} \left(\frac{E_x|_{i+\frac{1}{2},j,k+\frac{1}{2}}^{n-\frac{1}{2}} - E_x|_{i+\frac{1}{2},j,k-\frac{1}{2}}^{n-\frac{1}{2}}}{\Delta z} - \frac{E_z|_{i+1,j,k}^{n-\frac{1}{2}} - E_z|_{i,j,k}^{n-\frac{1}{2}}}{\Delta x} \right) + H_y|_{i+\frac{1}{2},j,k}^{n-1} \quad (4.18)$$

As a further example, we write down E_x component used in H_x above:

$$E_x|_{i+\frac{1}{2},j,k+\frac{1}{2}}^{n-\frac{1}{2}} = \frac{\Delta t}{\varepsilon} \left(\frac{H_z|_{i+\frac{1}{2},j+\frac{1}{2},k+\frac{1}{2}}^{n-1} - H_z|_{i+\frac{1}{2},j-\frac{1}{2},k+\frac{1}{2}}^{n-1}}{\Delta y} - \frac{H_y|_{i+\frac{1}{2},j,k+1}^{n-1} - H_y|_{i+\frac{1}{2},j,k}^{n-1}}{\Delta z} \right) - J_x|_{i+\frac{1}{2},j,k+\frac{1}{2}}^{n-1} + E_x|_{i+\frac{1}{2},j,k+\frac{1}{2}}^{n-\frac{3}{2}} \quad (4.19)$$

You can see the half step coordinate offset between electric field and magnetic field component in these equations. With centered difference approximation, each electric field and magnetic field component lie at a different 3D spatial lattice point offset by half of the increment, in order to update them in time sequence. Also, the time step is half of the increment different for electric and magnetic field. This is shown in figure 4.3.

4.3 Comparison with other EM simulation method

Finite element method (FEM)

FEM replaces the Maxwell equations in continuous space with simpler interpolation functions in smaller subspaces (elements). By doing this, functions with infinite degree of freedom can be approximated by solving finite coefficients of simpler functions. The first step is discretization of the space that will be simulated. The entire space is divided into small elements that can take shapes of triangles or rectangles etc. in 2D, tetrahedra or rectangular blocks etc. in 3D. The size and distribution of the elements are carefully decided so that the numerical approximations

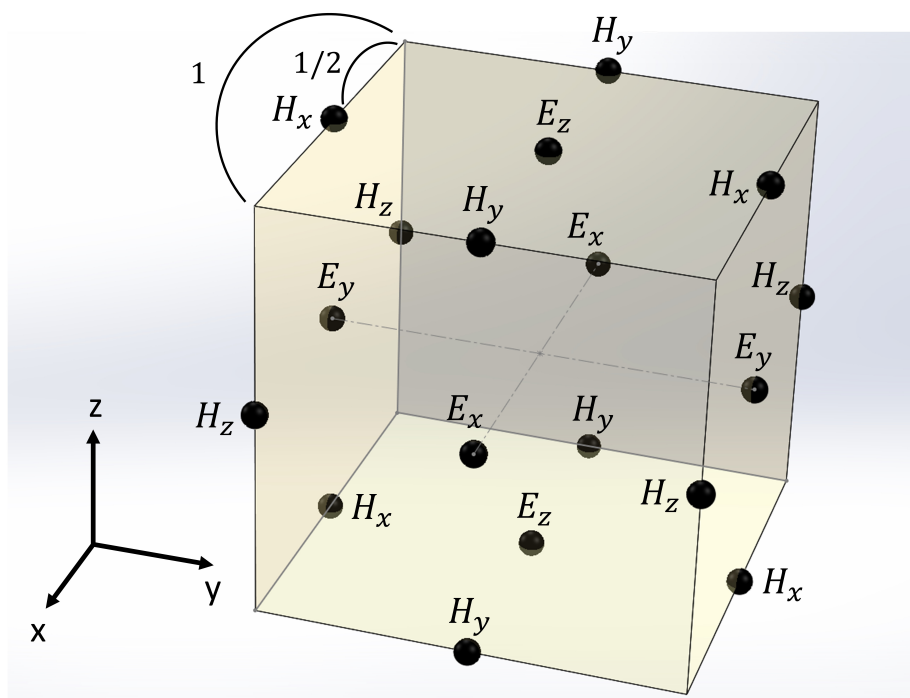


Figure 4.3: Electric and magnetic component positions in Yee algorithm.

are sufficiently accurate with appropriate computation time. The principle is that electromagnetic waves behave in a way that they minimize their total energy. FEM is used in COMSOL Multiphysics software offered by COMSOL, Inc.

4.4 MEEP simulation of c-Si on SiC ring resonator devices

We used the open-source software MEEP[77] to simulate our Si ring resonator devices on SiC with FDTD method. This section explains details of the MEEP simulation steps. These simulations were run in multi-core computers using the parallel computing version of MEEP, meep-mpi. The most time consuming simulation described in the section is a 3D ring simulation with waveguide, typically taking 2-3 hours with 20 processors.

2D cylindrical ring simulation

In this first simulation step, we want to simulate ring resonators by looking at the modes confined in a 2D space assuming cylindrical symmetry. We'd like to choose the ring's radius, width and height at the end of the simulation step. We prefer

smaller ring radius (smaller mode volume), smaller ring height (More evanescent field underneath the substrate) and high quality factor. We wanted to simulate single TM mode ring resonator. The refractive index configuration is shown in figure 4.4 (a). TM mode was chosen because stronger field can exist beneath the Si and SiC interface compared to the transverse electric mode due to the field discontinuity, which is shown in figure 4.4 (b)(c). This simulates the ring structure without any waveguide. Because it has continuous rotational symmetry, one dimension in ϕ is reduced and we can only think about field change in r and z coordinates. In MEEP, you can evaluate the quality factor by using special harmonic inversion function at a given point inside the ring. The simulated quality factor vs. ring radius with a fixed height 360 nm and width 300 nm is shown in figure 4.5. One can see more light leaking out through the substrate to the external ring direction when the radius of the ring is smaller. In this ring design, the radiation limit was reached with radius $\sim 3.25 \mu\text{m}$ with simulated $Q < 1000$. The radius $3.75 \mu\text{m}$ with simulated Q was chosen to minimize the ratio of the quality factor $Q = 7 \times 10^5$ to mode volume V considering that the quality factor in the current fabricated devices is limited by scattering losses to $Q = 23000$. The simulation gives a calculated V of $19.5 (\lambda_{ZPL}/n_{Si})^3$. The 2D cylindrical ring simulation code is attached in the appendix ??.

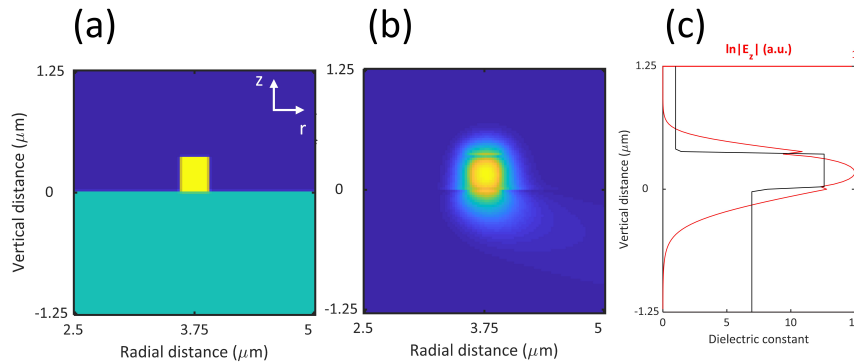


Figure 4.4: 2D cylindrical ring simulation (a) Refractive index setting (green: SiC/ $n=2.64$, yellow: Si/ $n=3.55$ and blue: air/ $n=1.00$)(b) $\ln|E_z|$ with colormap(c) Plot of $\ln|E_z|$ at the ring width center cross section.

3D ring simulation

3D ring simulation is necessary if we introduce waveguides that guide light to grating couplers. In contrast to 2D ring simulation with perfectly smooth sidewalls, roughness on rings is inevitable because of the computational grids (i.e. the resolution). In typical resolution of 40 pixels per unit length, 1 μm used in these simulation, the

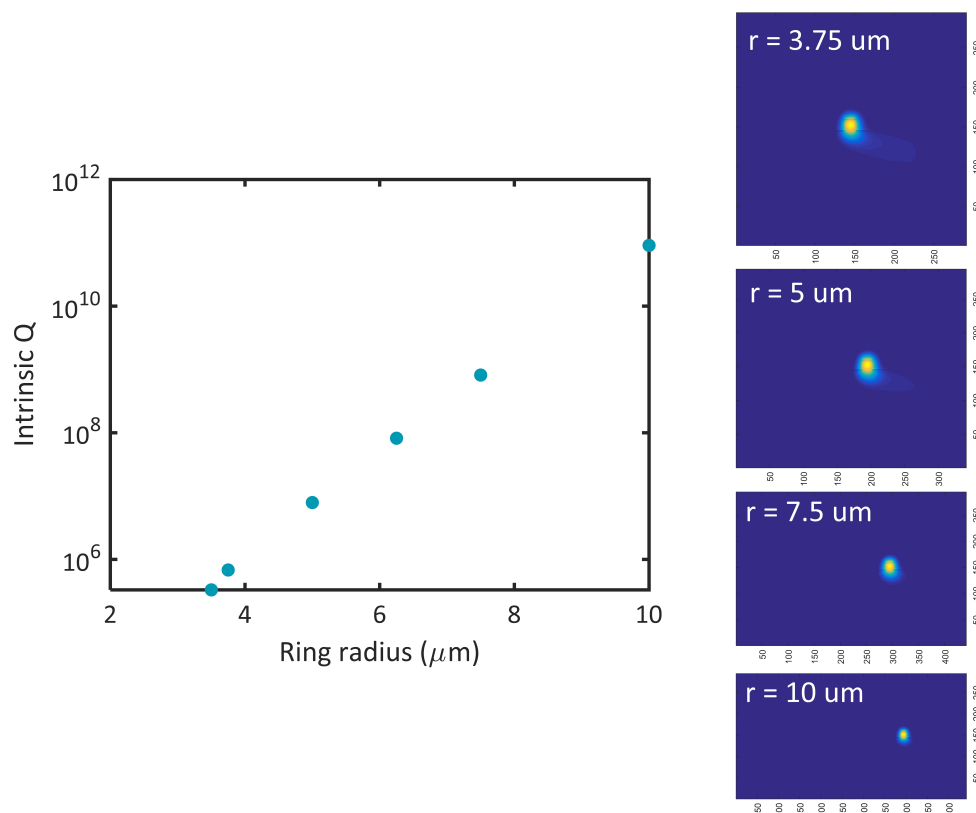


Figure 4.5: 2D cylindrical ring simulation quality factor vs. ring radius with height 360 nm and width 300 nm.

refractive index assignment causes rough radial surfaces with roughness of order ~ 10 nm. So we should consider the simulated quality factor in 3D a lower bound of that of fabricated ring resonators only with scattering effect. To fabricate close to critically coupled ring resonators, we simulated ring resonators with waveguides at different distances from rings. The typical simulation setup and results are shown in figure 4.6 (a)(b). The change in quality factor depending on waveguide-ring distance is shown in figure 4.6 (c). The intrinsic quality factor in this 3D simulation was 2.1×10^5 . From this result, we choose to fabricate arrays of ring resonators with different waveguide separation that gives 20-80% of intrinsic quality factor. The 3D ring-waveguide simulation code is attached in the appendix ??.

2D and 3D grating coupler simulation

To efficiently collect and detect emission from the divacancies grating couplers were added to the end of waveguides for diffracting light to a microscope objective. Basic

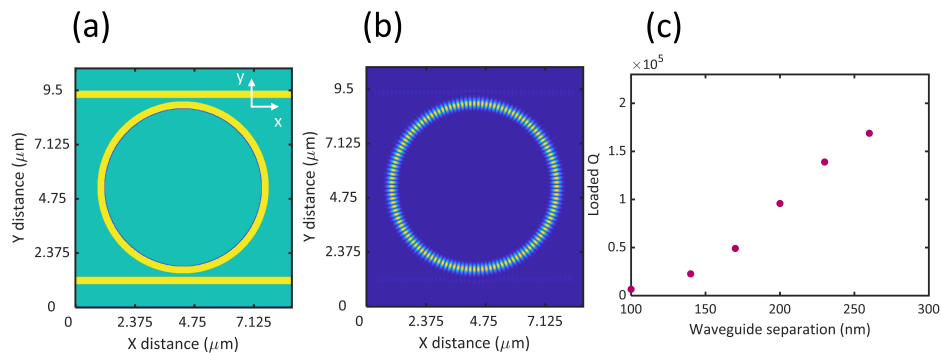


Figure 4.6: 3D ring simulation with waveguides. (a)Refractive index setting (color distribution same with figure 4.4) (b) $\ln|E_z|$ (c)Quality factor vs. waveguide distance

grating coupler parameters such as grating period and duty cycle were simulated for wavelength 1080 nm. To calculate the grating coupler efficiency we place a flux region in the simulated space where the fields are scattered and evaluate the electromagnetic flux or integral of Poynting vector going through that region. The following figure 4.7 depicts the typical simulation setup in 2D. The two lines are the flux regions in this simulation for evaluating diffracted light in almost vertical or angled direction accordingly. Also, a waveguide transmission simulation is performed to evaluate the flux going through the end of the waveguide, which is set to the same length of grating coupler in the other simulation. The grating coupler efficiency in these simulations is calculated by the normalization flux (F1) divided by the sum of the flux going through vertical/angled direction (F2+F3) in the grating coupler simulation, as shown in figure 4.7. In 2D simulations, gratings were considered to be straight and infinitely long in z direction.

I started the flux simulations by sweeping the grating period and duty cycle to find a parameter range that gives significant amount of F2 flux and a good wave profile. Our objective lens can collect light from a light cone of angle less than $\sim 38^\circ$, so we also wanted to pick parameters that ensure the grating doesn't diffract significantly beyond that angle. Then we simulated the flux in a finer sweep of parameters in this range and also took electric field output snapshots at the end of the simulation. The summary of the flux simulations with the finer sweep is shown in figure 4.8. We needed to look at the electric field diffraction pattern by plotting the snapshot to make sure the grating actually diffracts. Even if there seems to be a lot of flux going through F2, light might be scattered with the first grating without propagating

much. We wanted to see plane wave like pattern similar to what is shown in the right bottom figure 4.7. In this design of simple grating couplers, increasing the duty cycle with fixed period increases diffraction angle (figure 4.9) and increasing period with fixed duty cycle also increases diffraction angle (figure 4.10). This trend can be seen in the right panel of figure 4.8 by F2/F3 flux. To ensure the diffraction angle is not too steep I chose parameters with $F2/F3 > 10$ and F2 is close to maximum in the left panel of 4.8. From this simulation we picked grating parameters of grating period 470 nm and duty cycle 82 % (Grating width 385 nm and gap 85 nm) for fabrication.

3D simulations use concentric grating couplers, that are implemented in fabrication to see changes in efficiency compared to straight gratings. The 3D simulation configuration is shown in figure 4.11. The simulation revealed the concentric design doesn't change much the optimized parameters obtained in 2D simulation. The best parameters obtained from 3D simulation is period 490 nm and duty cycle 80 %. The 2D/3D simulation codes are included in appendix ??.

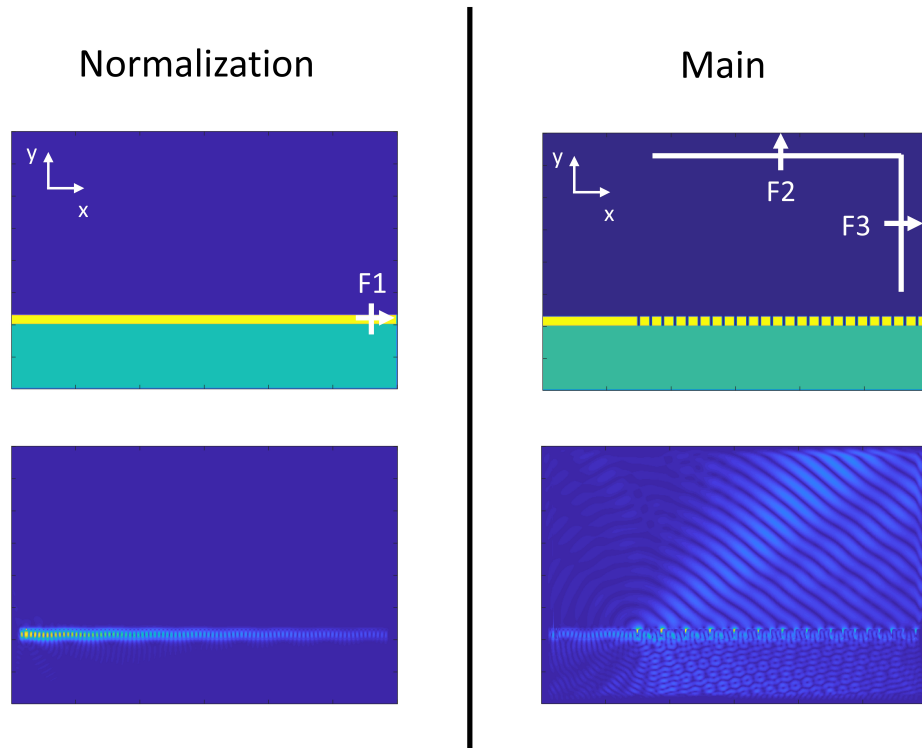


Figure 4.7: 2D grating simulation normalization simulation on the left. Main simulation is on the right. Top figures are refractive index configuration and bottom figures are plotting $\ln|E|$.

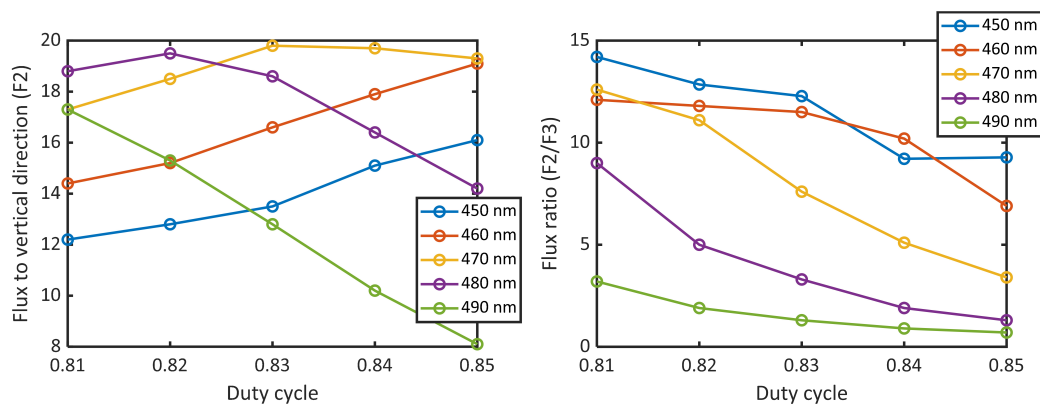


Figure 4.8: 2D grating flux depending on period and duty cycle.

Period 470 nm

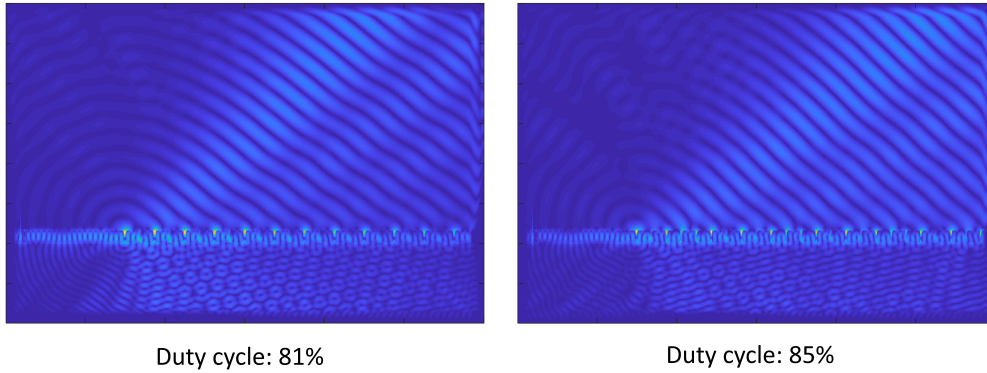


Figure 4.9: 2D grating diffraction angle change depending on duty cycle (fixed period)

Duty cycle 82%

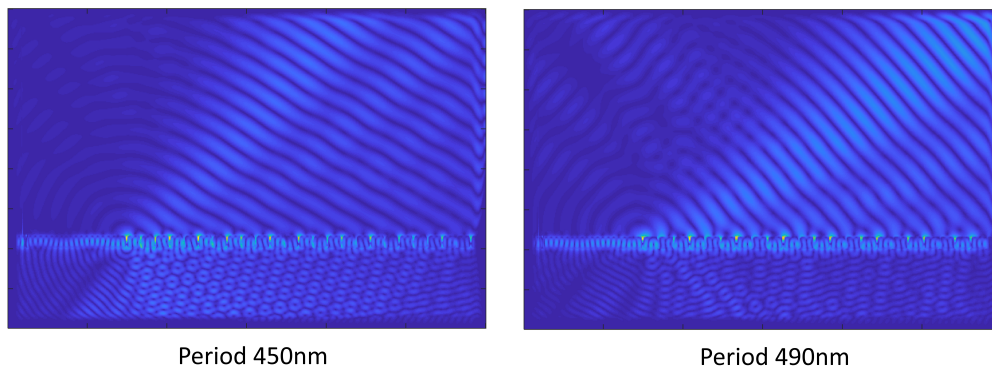


Figure 4.10: 2D grating diffraction angle change depending on period (fixed duty cycle)

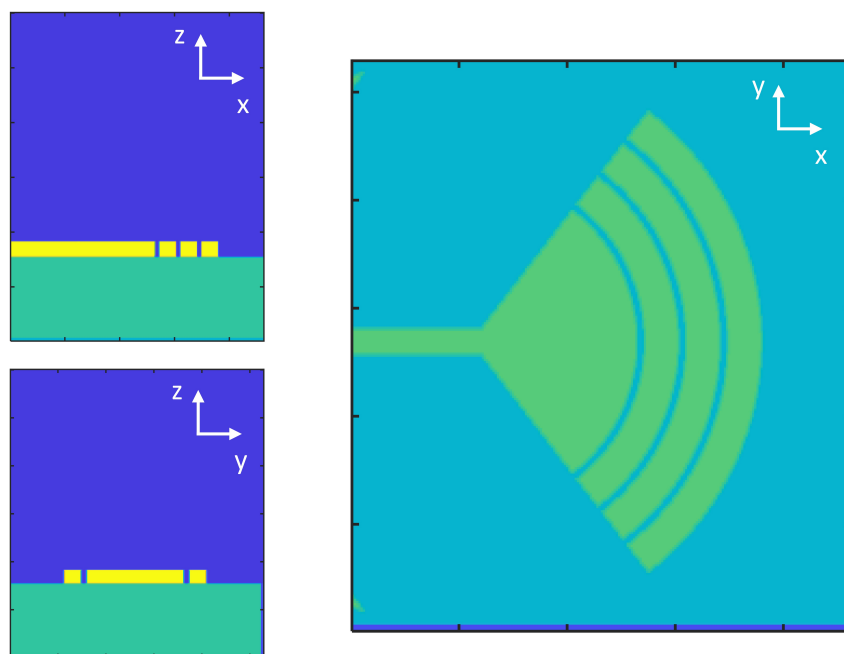


Figure 4.11: 3D grating simulation configuration. Each figure is at the center plane of the simulated space.

Chapter 5

FABRICATION OF ON-CHIP PHOTONIC DEVICES FOR COUPLING TO DEFECTS IN SiC

In this chapter I describe the fabrication procedure for on-chip photonic devices for coupling to luminescent defects in silicon carbide. The most successful effort was hybrid devices based on crystalline silicon (c-Si) placed on top of 4H-SiC.

5.1 Qubits generation in 4H-SiC

Ion implantation and divacancies

The concept of the hybrid devices that we aim to fabricate is that the photonic mode is confined in a silicon device and is evanescently coupled to luminescent centers located close to the surface of the substrate. In this case we aim to couple to divacancies. Divacancies are common and intrinsic in 4H-SiC and the ZPL of ensemble divacancies can be readily measured in our high-purity semi-insulating 4H-SiC wafers purchased from CREE Inc[32, 34]. Divacancies can also be created using Si or C implantation[38, 78] or electron irradiation[45]. Using implantation is advantageous in our case because the divacancies are created close to the surface. Since we also wanted to generate other color centers based on other elements, we also created divacancies by implantation of ions from the elements Cr and Mo.

Before implantation, we estimated the depth distributions of the implanted ions using computer simulations for Stopping and Range of Ions in Matter (SRIM)[79]. Having divacancies closer to the surface is beneficial because it leads to stronger coupling to the resonator mode. However, generally the proximity to surfaces leads to degradation in the optical and spin properties of the divacancies. Since we were not sure about these tradeoffs, we had some of our samples implanted with 10 and 150 keV implantation energy. For example for Cr implantation the distribution of implanted ions peaked between 9nm and 90nm. We assumed that divacancies will be created similarly to this distribution. The Cr ion density at 10nm depth with dose 10^{13} is estimated to be $10^{19}/\text{cm}^3$. The results of our implantation is shown in the following table, which also indicates if divacancies were observed.

Implanted ion	Implantation energy (keV)	dose (cm ²)	Photoluminescence detected? (1000-1500nm)
N	150	10 ⁹ ,10 ¹¹ ,10 ¹³	Divacancies
Ni	150	10 ⁹ ,10 ¹¹ ,10 ¹³	Divacancies
Cr	10, 150	10 ⁹ ,10 ¹¹ ,10 ¹³	Divacancies, Cr ions
Mo	200	5×10 ⁹ , 5×10 ¹⁰	Divacancies, Mo ions

Table 5.1: List of samples with different ion implantation and photoluminescence

Annealing

An annealing process is required such that the generated vacancies migrate and form divacancies. We annealed implanted 4H-SiC in Argon at 900 °C. We chose this temperature because divacancy formation decreases and trivacancies formations starts to dominate over 1400 °C [80]. We tried different annealing time, 30, 120, 240 mins and observed how the ZPL of specific divacancies change. The annealing process includes additional ramp up/down time of 30 mins each, which is kept the same for different annealing time. We note that it might be better to decrease the ramp time to increase PL of divacancies, as suggested by Gällström et al. [81]. The following ?? shows the ZPL of divacancies under different annealing temperature condition.

5.2 4H-SiC transfer

When starting this project, we first attempted to make photonic devices directly in the host material, SiC. Heteroepitaxial growth is available for 3C-SiC but not for 4H, or 6H-SiC. The alternative method is transferring a thin membrane of 4H-SiC onto a different material and fabricating the device directly into the SiC membrane. We transferred a thin layer of ion-sliced 4H-SiC on silica following the procedure similar to the one described in Lee et al. [82].

The transferred membranes were inspected under SEM. As it can be seen in figure 5.1, generally they have large roughness >10nm on the surface. We considered this surface too rough to have good photonic devices fabricated on and changed to hybrid approach that will be discussed in next 2 sections. Also, we did photoluminescence measurements on this material and we discovered that it was full of defects, including divacancies with very broad linewidth (~1 nm for PL1), which would make it difficult to develop devices that work at single photon level.

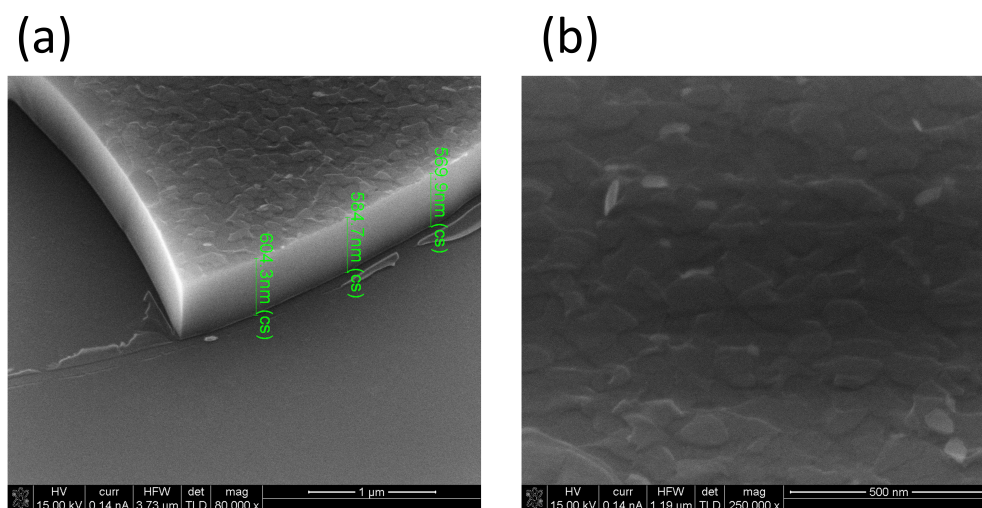


Figure 5.1: SEM image of 4H-SiC membrane surface transferred by smart cut method.

5.3 a-Si:H Deposition

The next technique that we tried was by depositing amorphous silicon onto SiC, with the goal of fabricating the devices directly into the silicon for evanescent coupling to defects in SiC. We deposited hydrogenated amorphous Si (a-Si:H) on 4H-SiC with plasma enhanced chemical vapor deposition (PECVD). We used parameters in table 5.2. The deposition rate is approximately 26 nm/min. The ring resonator devices we fabricated using a-Si only gave best $Q \sim 5000$. SEM inspection revealed there is noticeable roughness on the surface of a-Si as shown in 5.2. The surface shows grains of a-Si [83, 84]. We tried depositing alumina Al_2O_3 for 20 nm to reduce this effect as there might be substrate dependence on roughness [85, 86]. A 20nm thin layer of alumina between SiC and a-Si doesn't disturb the confined light profile according to simulation. Measurements with higher resolution of roughness were performed under atomic force microscope (AFM). The measured surface roughness was slightly improved compared between a-Si deposition with and without alumina as shown in figure 5.3 (a)(b). The roughness comparison AFM images of a-Si, c-Si and the original substrate are shown in figure 5.3. However, this roughness was still considered too high so we decided to fabricate devices in a crystalline silicon membrane transferred on top of SiC.

Deposition parameters	Values
RF forward power	10 W
5% SiH ₄ in Ar flow rate	40.0 sccm
Chamber pressure	801 mTorr
Wafer temperature	200 °C
Deposition rate	26 nm/min

Table 5.2: a-Si recipe

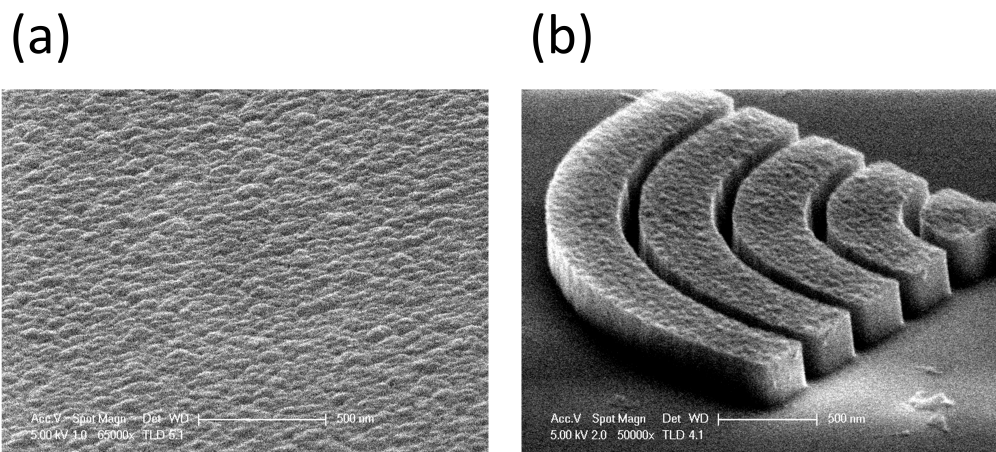


Figure 5.2: SEM images of a-Si roughness. (a) a-Si deposited before any patterning procedure (b) A grating coupler after etching and cleaning. process

5.4 c-Si Membrane Transfer

The fabrication process of the hybrid devices starts with transferring c-Si membrane from silicon on insulator (SOI) chips by Soitec. The SOI wafer has a Si device layer thickness of 500nm, close enough to the desired 360 nm height for the ring resonators. Si is B doped p-type and the buried oxide thickness is 3 um. The c-Si transfer procedure is summarized in table 5.3. The details of each step is described in following sections. This c-Si transfer procedure was inspired from work by Li et al. [87].

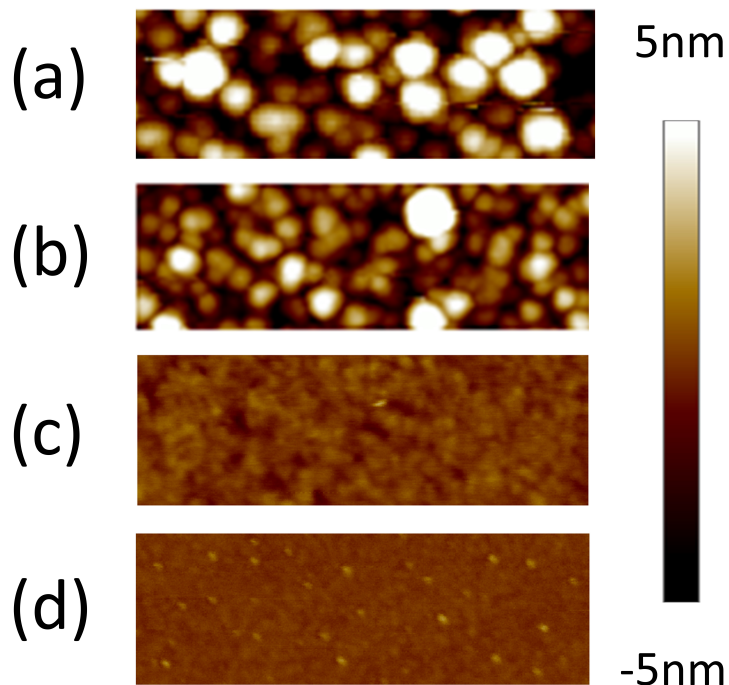


Figure 5.3: AFM images for comparison of roughness. (a) Deposited a-Si. (b) Deposited 20nm alumina then a-Si. (c) Transferred c-Si all on top of 4H-SiC. (d) AFM on the 4H-SiC substrate.

Cleaning

Purchased SOI wafers were dipped in Nanostrip(H_2SO_4 , H_2O_2) for one hour. Then they were cleaned in typical solvent rinsing (acetone, methanol, IPA).

Thinning c-Si to desired layer depth

Because it is hard to find SOI chips with the exact Si thickness of what we desire to use for the devices, this step is required to adjust the thickness of the membranes. The oxidation rate can be calculated and fitted based on the theory described by McGuire [88]. The rate depends on different factors such as Si surface charges, dopant concentration or oxygen distribution, pressure, etc. We took a few data points of (oxidation time, oxide thickness) and generated a MATLAB code that fits these to the theoretical curve to estimate the correct oxidation time, which is included in ???. This calculates for both wet or dry oxidation.

Based on the calculated oxidation time, we performed wet oxidation of 32 mins at 1000°C . Before and after the oxidation process, there is 1.5 hrs of ramp up/down time in nitrogen environment from/to 700°C . After the oxidation process, we

Step	Description
Cleaning	SOI chips are cleaned with Nanostrip.
Thinning the Si layer	Oxidation and HF wet etching are performed.
Dicing Si membranes	500 μm \times 500 μm squares are patterned.
Releasing membranes	HF wet etching of BOX layer are performed.
Cleaning 4H-SiC substrate	The surface is changed to hydrophilic state.
Picking up membranes	Quick pick-up with the substrate was performed.
Slow natural drying	Membranes are attached without air or water underneath.
Check membranes quality	Optical microscope and SEM examination are performed.

Table 5.3: c-Si transfer procedure

removed the generated oxide by wet etching with buffered HF. The final thickness of the Si device layer is fitted and calculated in a spectral reflectance analyzer by Filmetric with >95% goodness of fit and is $<\pm 10$ nm from the desired thickness.

Dicing Si membranes

This step is required to make membranes in small size so that it takes a short time to release the membranes and also increases the success rate of attachment of the membrane to the SiC substrate. Initially we hand cleaved an oxidized SOI chip into 3 mm square small pieces and tried to release the membranes in 52% HF. After 24 hours some of them were still not released and the Si membranes show gradation of color suggesting etching and damage by HF. Also, transferring released membranes in large size easily induce bending and cracking of membranes, which prevents good attachment to the substrate. When the attached membrane will be cleaned or spin coated later, one small opening between the substrate can allow liquid to flow in and the membrane can be flushed away. The same problem occurred when we tried transferring a large membrane with holes spaced regularly. Due to these reasons, we tried membranes with a smaller size of 500 μm \times 500 μm and this worked well with >50% yield.

We used a positive resist AZ 5214E for patterning squares on SOI chips. We exposed

spin coated chips with a photomask in a mask aligner photo-lithography system. The mask design is shown in 5.4 (a). The details of the patterning procedure is shown in 5.4. The etch will remove silicon from the exposed part of SOI chips and create separated Si membranes. We used an etching recipe described in table . A patterned SOI chip is shown in 5.4 (b) under optical microscope.

Step	Description
Step	Put SOI chips in the container for 3 mins.
Spin coating	1500 rpm/ 60 s ($> 2 \mu\text{m}$).
Soft baking	110 °C/ 45 s.
Exposure	5 s (75 mJ in total with 15 mJ /s).
Development	70 s in MF-319 developer.
Cleaning	Solvent cleaning with sonication for 5 mins.
ICP/RIE etching	pseudo-bosch for 8 mins.
Resist removal	Dip in acetone for 3 mins.

Table 5.4: SOI chip square patterning procedure

Releasing the membranes

This step releases Si membranes by detaching the Si device layer from its handle layer. We put small pieces of patterned SOI chips in 52 % HF filled in a small polypropylene jar Si side facing up. Generally it takes 15-30 mins to release all the membranes. We can identify this by the color change of the membranes due to removal of the BOX layer. We prepared large containers filled with water for rinsing membranes. Then we take the chip out slowly without tilting it to prevent membranes from floating away. We put it in water angled to make water go underneath the membrane and flush them away from the handle layer. The membranes are floating on the surface of water. We scoop a single membrane using a plastic spoon and transfer to different containers filled with water several times for cleaning the back side that will be attached to the substrate as shown in figure 5.5. At the end, we transferred the cleaned membrane to a large container filled with clean water where

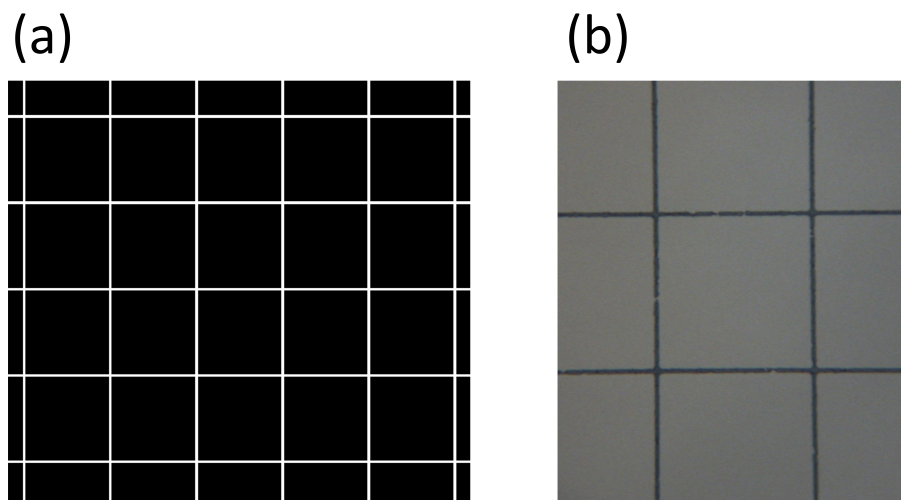


Figure 5.4: (a)Design of the photomask (b)Etched SOI chip after photolithography (light gray: Si, dark gray:SiO₂)

we will be picking it from. At this stage, any membrane that looks bent or folded is discarded. Bending or folding of a membrane often allows water to exist at the interface of the membrane/substrate, which is concluded with >30 trials.

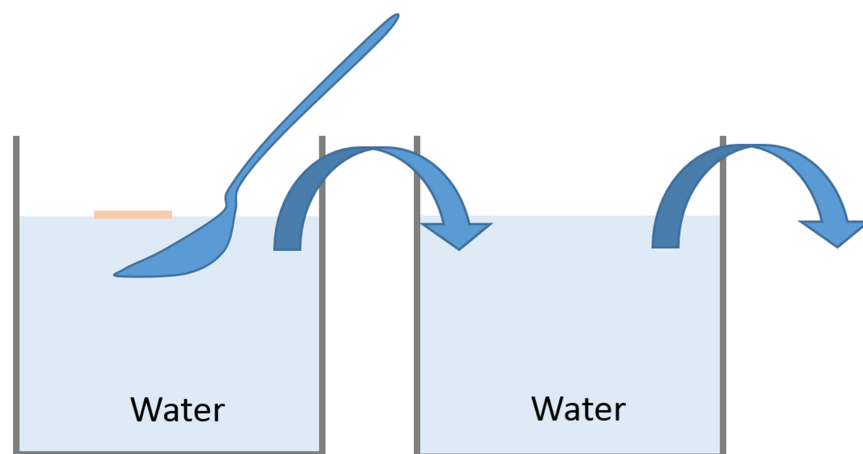


Figure 5.5: Cleaning by transferring a floating membrane to clean water

Cleaning the 4H-SiC substrate

Right before the pick-up process, oxygen plasma cleaning was performed to the 4H-SiC substrate. This step is required to make the substrate hydrophilic such that the bending angle of a picked-up membrane while drying won't be too large. Also, it makes the substrate clean such that water underneath the substrate is easier to move away when the membrane is pushed and attached by Van der Waals force, preventing for water left under the membrane. This step was essential for achieving a high yield of usable membrane area.

Picking up membranes and drying

This step involves transferring floating membranes to the substrate and natural attachment of membranes using Van der Waals force. We hold a cleaned substrate underneath a cleaned floating membrane and quickly pull it upward and toward the membrane out of water. This requires some speed to ensure the membranes stay on the substrate before they flow away. After picking-up the membranes, the substrate is placed in a place without disturbance and the membrane dries slowly. Rapid drying using a hot plate didn't gain good results with many bubbles underneath a membrane. If the substrate is smooth and the membrane is flat, Van der Waals force will push water away and shouldn't leave any water underneath the membrane that can be seen by eye (figure 5.6). After the substrate dried fully we put it on a hot plate with temperature > 150 °C and inspect if any water is left. The following figures 5.7, 5.8 show examples of successful and failed attempts of membrane transfer. After this step, if the membrane has more than 50 % area left without any water or other defects, we will use it in next electron beam writing step. This entire c-Si transfer procedure overall gives ~ 50 % yield of such usable membranes. Because this transferring method requires physical dexterity and we don't have control over where to put the membrane on the substrate, we wanted to find more reliable methods of fabricating hybrid devices. For this, we attempted to transfer GaAs photonic crystal devices using a nanomanipulator implemented in FIB/SEM system, which is described in A.3.

5.5 c-Si on SiC device patterning and fabrication

Electron beam lithography

All the device patterning was performed under Raith EBPG 5000+ or 5200 system operated at electron energy of 100 keV. ZEP520A positive tone resist is used. Also, our SiC substrate is not conductive so we spin coated conductive polymers,

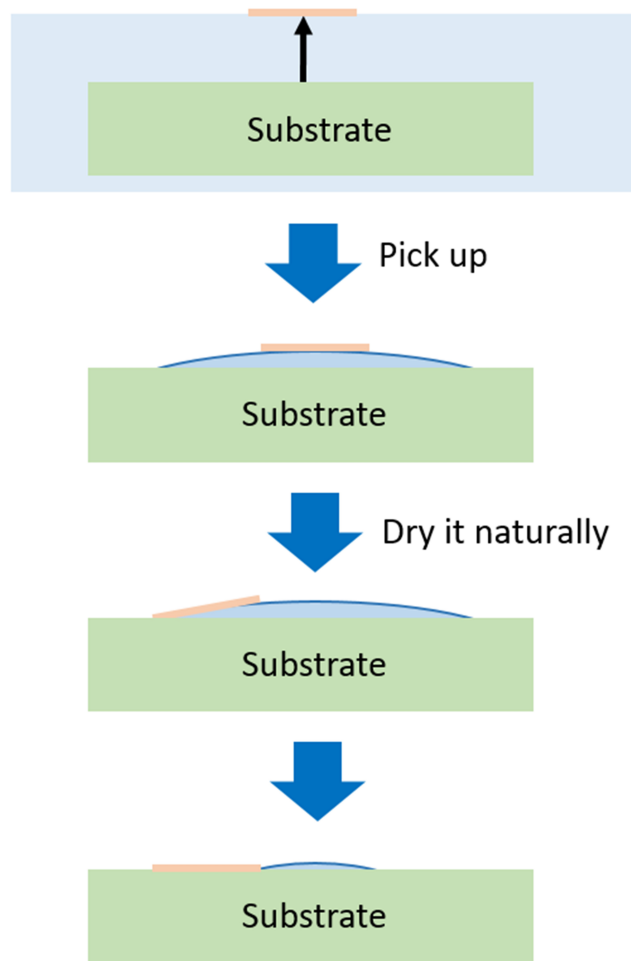


Figure 5.6: Picking up the membrane, drying and attachment on the substrate.

AQUASAVE to prevent electron beam trajectory distortion due to built up charges. The spin coating and development parameters are shown in table 5.5. Ring resonators are patterned with 300 pA, approximately 2 nm beam spot size. The electron scattering induces undesired exposure to nearby exposed locations. Such proximity effect can be corrected by knowing how much electron energy is exposed to neighbor resist by a single pixel exposure. The point spread function distortion due to proximity effect is simulated by Monte Carlo simulation, PENELOPE [89]. We simulated the proximity effect with settings of 10M electrons for the sample layers from the substrate up to ZEP resist.

ICP/RIE etching

A resist reflow technique is used to improve the sidewall roughness caused by resist roughness in the process of development[90]. By heating the resist at right

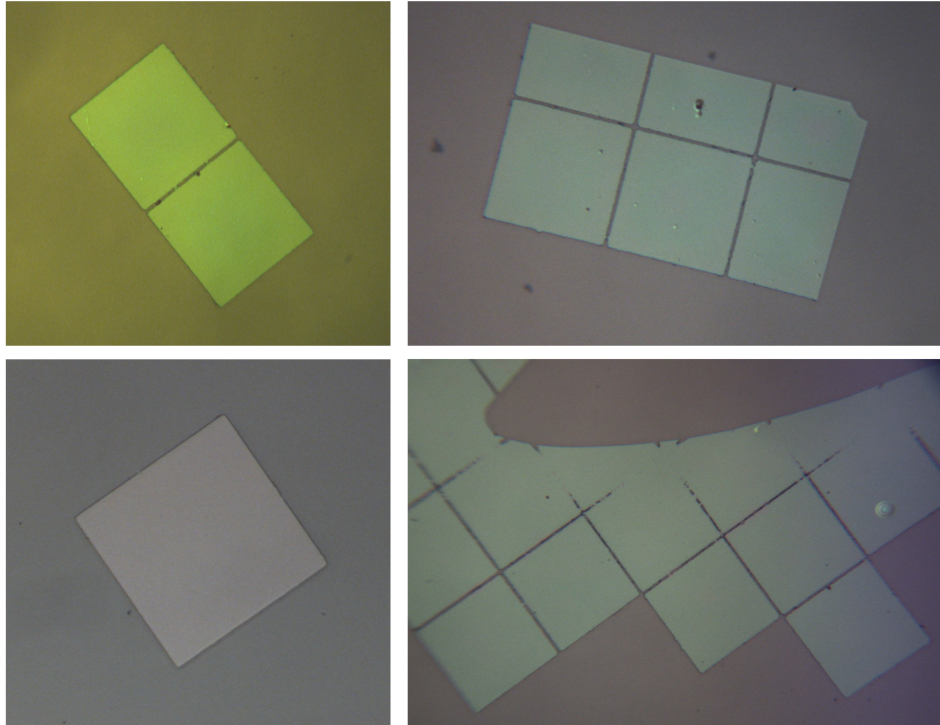


Figure 5.7: Successful membrane transfer. Most membranes are single but some of them are connected.

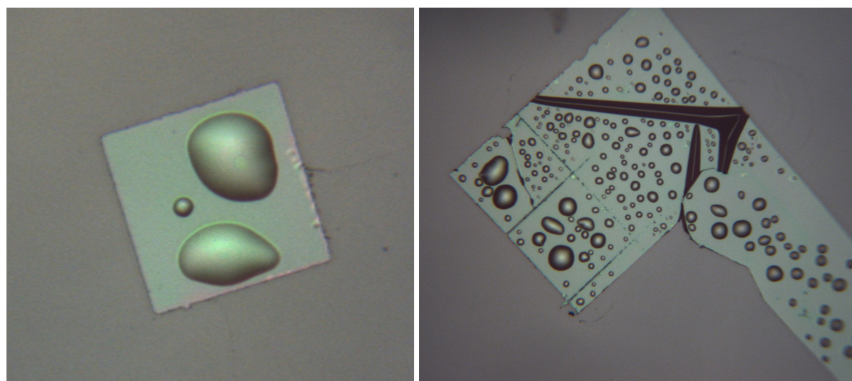


Figure 5.8: Failed membrane transfer. Water scattered underneath the membrane. Heating on a hot plate caused water to evaporate and made bulges on membranes. Wrinkles in membranes allow water to enter and flush of the entire membrane.

Steps	Parameters
Resist spin coating	5000 rpm / 60 s
Baking	180 °C / 3 mins.
AquaSAVE spin coating	1500 rpm / 60 s
Baking	70 °C / 5 mins.
Development	Dip in ZED (slowly stirred) / 3 mins then rinse with MIBK / 30s and with water.
Resist reflow	145 °C / 10 mins

Table 5.5: E beam writing resist related procedure

temperature it slowly melts and roughness in the resist is reduced. We put the sample in an oven at 145 °C for 10 mins, which is empirically determined by monitoring the resulted sidewall angle under SEM. As described in a later section for our devices that have quality factor ~ 20000 , the resist reflow did not result in a huge improvement in the quality factor ($< 10\%$).

After the reflow process, we etched the sample in $\text{SF}_6/\text{C}_4\text{F}_8$ plasma for ~ 6 mins with 60 nm /min etching rate. Santovac oil is applied at the back of the sample for fixing the sample and for thermal conduction, which can be easily removed with IPA or acetone. The Si pseudo-bosch recipe we used for etching a-Si and c-Si ring resonators is shown in following table. 5.6.

ZEP resist removal

After etching, we removed the ZEP by dipping the sample in N-Methyl-2-pyrrolidone (NMP) based solvent Remover PG for >12 hrs at 80°C, then we did oxygen plasma treatment for 10 mins and acetone/IPA flush at the end. Some byproducts of oxygen plasma reacting with ZEP are not volatile and there will be residue left as shown in figure 5.9 without solvent cleaning. Dipping in nanostrip after these steps should clean the samples more thoroughly but in my work, all devices were cleaned only with PG remover, oxygen plasma and solvent.

Etching parameters	Values
RF forward power	23 W
ICP forward power	1200 W
DC bias voltage	70 - 90 V
SF ₆ flow rate	15.0 sccm
C ₄ F ₈ flow rate	40.0 sccm
Chamber pressure	11.0 mTorr
Wafer temperature	15 °C
Helium backing pressure	4.0 Torr
Etching rate	60 nm/min

Table 5.6: Si pseudo-bosch etching recipe

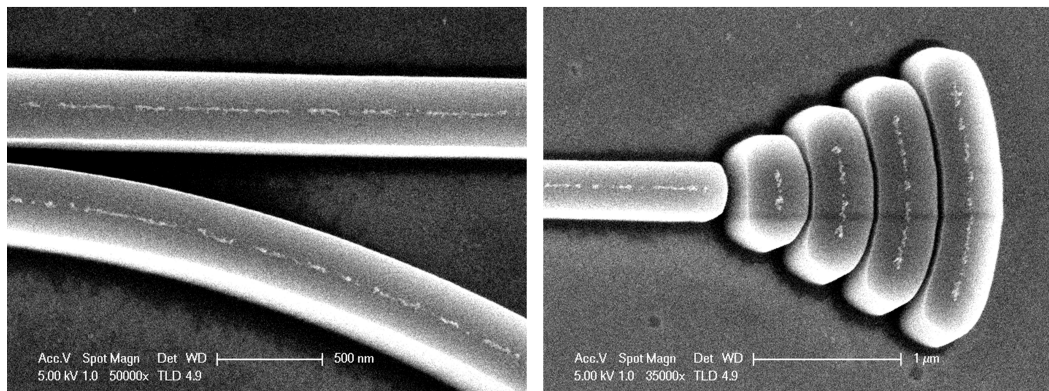


Figure 5.9: Residue of ZEP cleaned with O₂ plasma

Final fabricated c-Si on SiC devices

Figure 5.10 shows a fabricated c-Si on 4H-SiC ring resonator device. Devices written on clean membrane surface without visible bubbles or change in color rarely

had the problem of detaching from the substrate after all the fabrication and cleaning process.

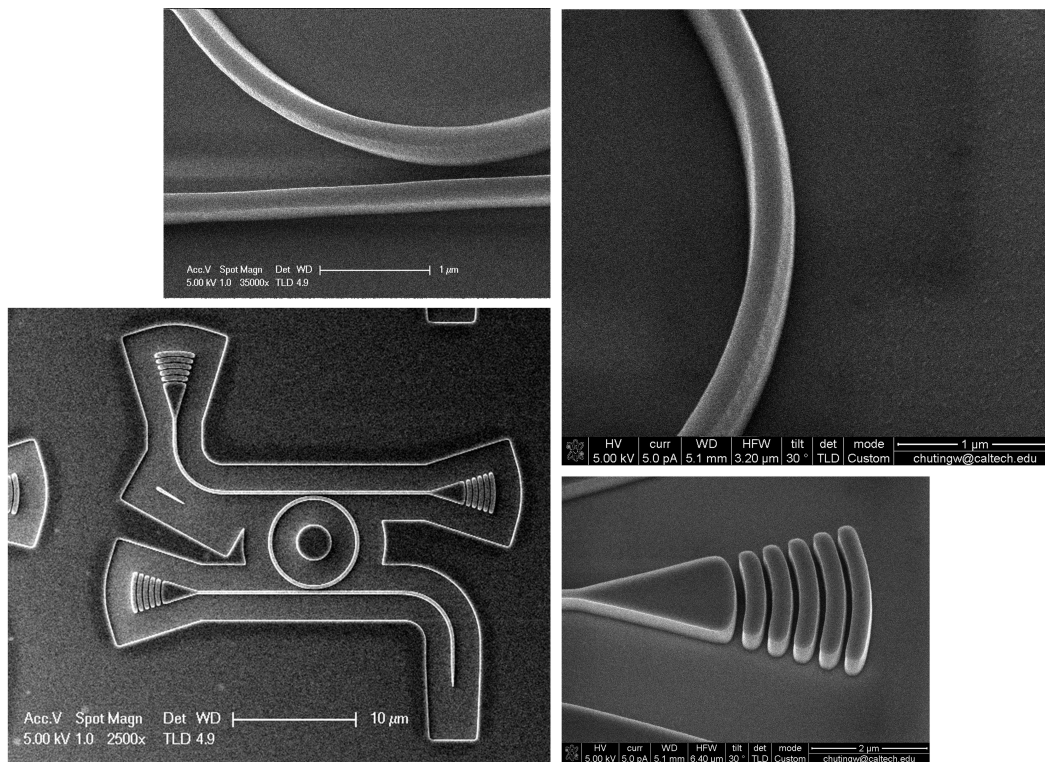


Figure 5.10: SEM image of a c-Si on 4H-SiC final ring resonator device

PHOTONIC DEVICE CHARACTERIZATION

Experimental setup

A home-built optical confocal microscope setup is used to characterize the fabricated ring resonators. The diagram of the setup is shown in figure 6.1 and the pictures of the actual setup are in figure 6.2. A 950 nm long-pass dichroic mirror was used to filter 780 nm excitation laser for spectroscopy measurements. For ODMR measurements, the nitrogen gas transfer port was replaced by SMA ports that can be connected to MW sources. Each ZPL of divacancies (PL1-4) was filtered using tunable longpass and shortpass filters. A superconducting nanowire single photon detector (SNSPD) was used for lifetime measurements on divacancies and Cr ions. An InGaAs detector after a beam splitter was used for the timing input to the time correlated photon counting board. A supercontinuum laser with repetition rate of 20 MHz and 2 kHz was used for divacancies (lifetime ~ 15 ns) and Cr ions (lifetime ~ 130 μ s) accordingly. The coarse resonance measurements of Si ring resonators were performed using a near IR spectrometer with a supercontinuum source. The gratings in the spectrometer are able to measure quality factors up to $\sim 30,000$ reasonably. The nitrogen gas tuning can typically tune resonances of silicon ring resonators for ~ 1.5 nm at 1070 nm.

To further characterize the resonance in higher resolution, I built a tunable external cavity diode laser with Littman-Metcalf configuration using Thorlabs kit (TLK-L1050M) with AR coated diode (LD-1050-0050-AR-2) purchased from Toptica as shown in figure 6.3. The coherent light was generated by stimulated emission with the help of an external cavity between the end face of the diode and the mirror. The feedback light that selects the wavelength of amplified light comes from the 1st order diffraction from the grating, and it was reflected back by a mirror in Littman configuration. The direction of the output laser is fixed during tuning because the output is the reflected light (0th order diffraction) from the grating, which is a main advantage over Littrow configuration. The wavelength tuning can be performed by moving the angle of the mirror and by sending back light with a different wavelength. The mirror can be controlled either with a DC servo motor (Z812) or with a piezoelectric actuator attached to the contact point of the motor

and the mirror arm. The maximum power is 50 mW around 1040 nm and > 10 mW in the range 1020-1085 nm before fiber coupling.

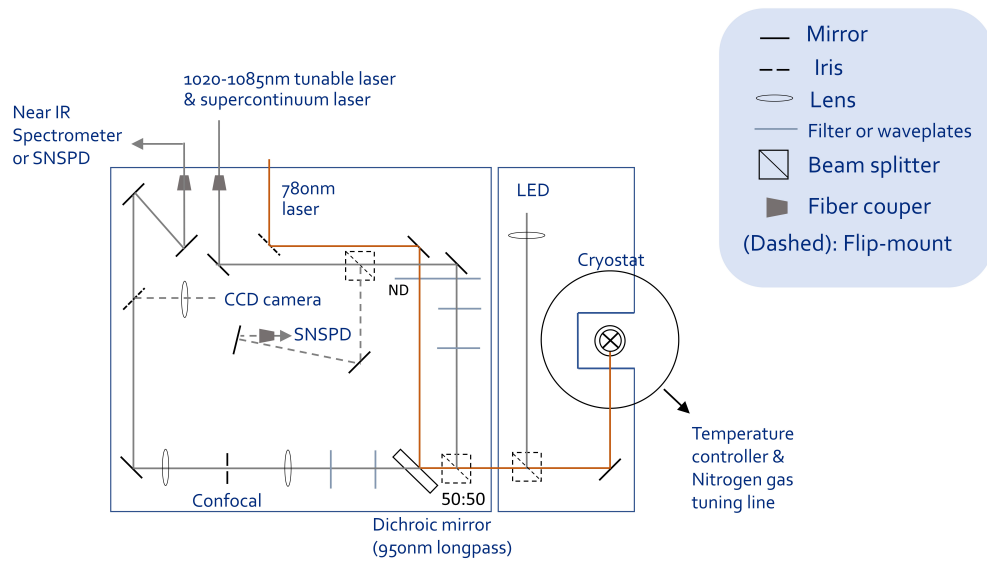


Figure 6.1: The optical confocal microscope setup diagram.

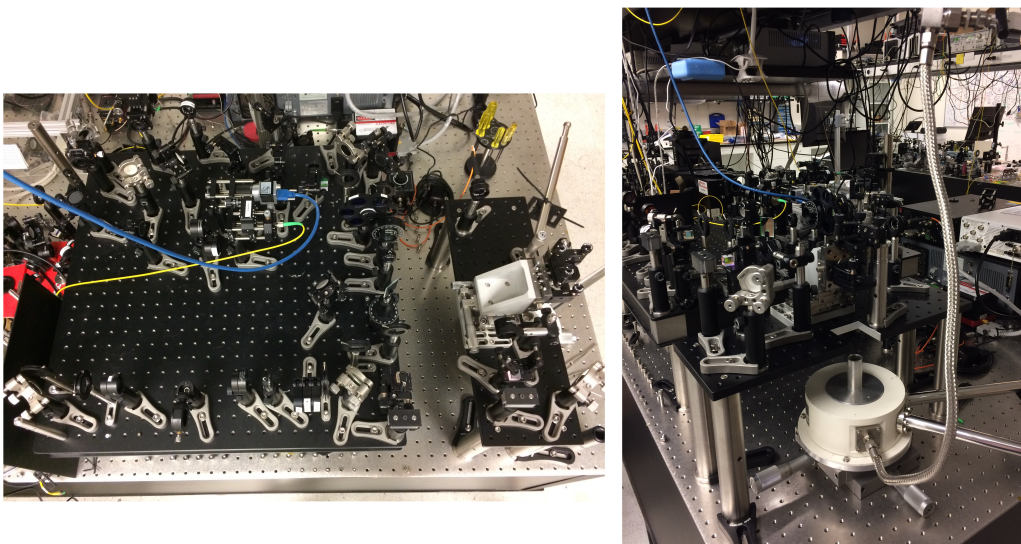


Figure 6.2: The actual setup (left) viewed from top and (right) viewed from the right.

Mode hop free tuning for a relatively large frequency range was required for scanning a resonant peak of an optical resonator. The mode hops occur when the next mode

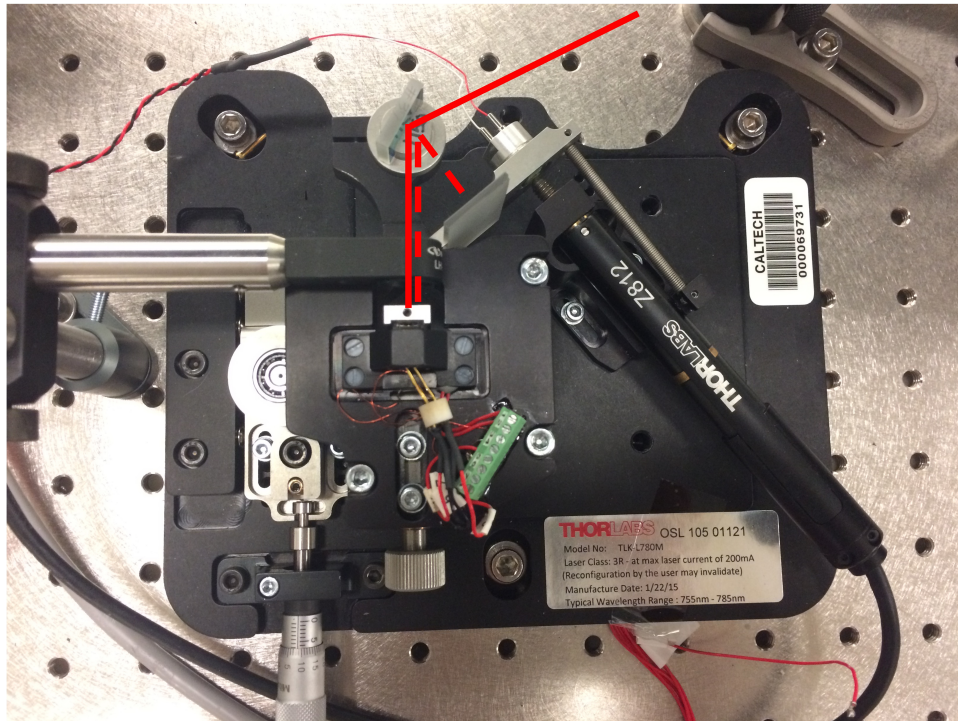


Figure 6.3: The actual Littman configuration in the setup. The red solid lines show the main laser path and the dotted line shows the feedback path.

has more optical feedback than the current mode, which often happens when the resonant peak of internal cavity formed by two end diode faces and of the external cavity don't match. We need to maintain both cavity gain peaks aligned during wavelength tuning. The internal cavity resonance moves by changing the diode current. The current and piezoelectric actuator voltage need to be changed at the same time with an optimized ratio to prevent mode hops[91]. The wavelength change of the internal cavity mode peak against diode current is expressed by $\beta = \frac{\Delta\lambda}{\Delta I_{LD}}$. To measure β , the laser diode output without feedback was measured using an optical spectrum analyzer for different diode current. Part of the measurements for low current 40-60 mA are shown in figure 6.4. $\beta=2.2$ GHz/mA at low current and $\beta=2.6$ GHz/mA at high current around 150 mA.

After lasing was confirmed with alignment, laser modes are monitored using a scanning fabry-perot interferometer. When the feedback is not optimal the laser operates in multimode with next mode separated by 1.9 GHz corresponding to ~ 8 cm external cavity length. After single mode operation is confirmed at fixed wavelength, the output power is maximized by optimizing the alignment. Then

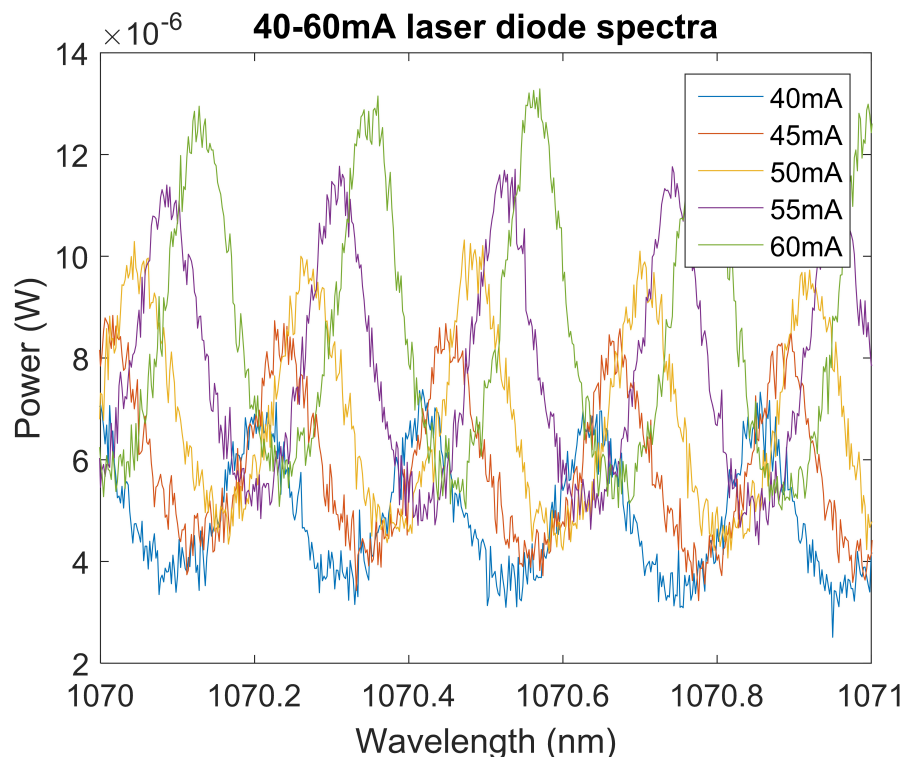


Figure 6.4: The internal cavity resonances change due to different diode current (40-60 mA).

piezo tuning as a function of applied voltage $\frac{\Delta\lambda}{\Delta V_{PZT}}$ was measured with a fixed fabry-perot resonance. With previously measured β , I built an inverting amplifier that controls the laser diode current depending on the piezoelectric actuator voltage so that internal and external cavity modes move at the same rate. I used a potentiometer for one of the 2 resistors to adjust the change of β at higher diode current during tuning. The external signal proportional to the piezo voltage is input to the inverting amplifier and its output was fed to the laser current controller.

After single mode operation in a full piezo scan without mode hops was confirmed, piezo calibration was performed. Piezo movements are not linear against applied voltage and the wavelength change per unit voltage change at different piezo voltages was measured as shown in figure 6.5. Piezo modulation of 1 Hz triangular wave (0-150 V) is used for measurements. The InGaAs detector of the IR spectrometer continuously takes frames during the scanning and the photon counts at every wavelength pixel is integrated for each frame as output signal. Because the linewidth

of laser was not measured and it is less than the 67 MHz scanning fabry-perot resonance FWHM, the scanning frequency is adjusted so that this scanning method can give 95 MHz resolution. 1 GHz separated sidebands were added by electro-optic modulator as a standard and changed the resonance of a scanning fabry-perot to measure peak to peak separation in the range of 0-150 V. The resulting curve was fitted and used for correction of resonance scan data.

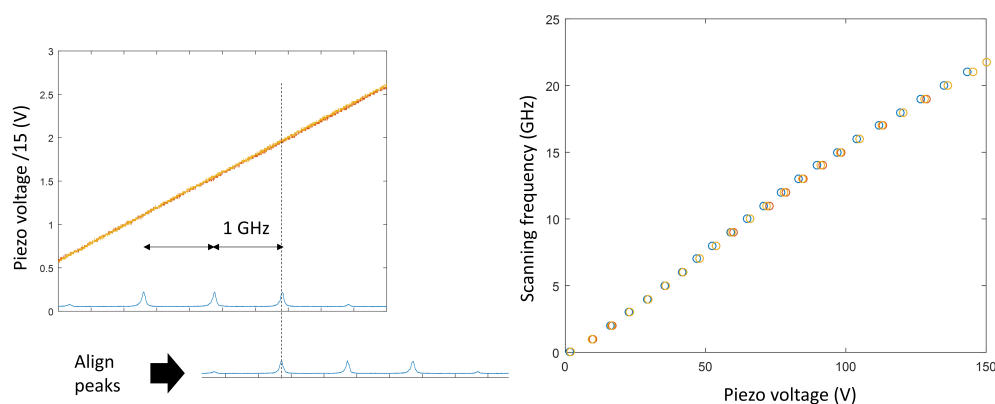


Figure 6.5: The actual Littman configuration in the setup. The red solid lines show the main laser path and the dotted line shows the feedback path.

The laser power is modulated during scanning and the laser power versus diode current was measured to provide correction to scan data as well. The laser power is almost linear to the diode current as shown in the left panel of figure 6.6. The stability of the laser power was measured over 8 hours to verify that the laser is stable enough for scanning measurements as long as a couple seconds each, as shown in the right panel of figure 6.6. The wavelength shift was < 1.0 pm/hr.

c-Si on SiC resonators measurement results

The measurements of the quality factor of ring resonators were mostly performed by focusing the laser on the input port and collecting the output from the drop port as shown in figure 6.7. One of the best ring resonators has a quality factor of 23000 at 1078 nm measured at 20 K. The measurement results are shown in figure 6.8. The condition for critical coupling of ring resonators coupled with two waveguides is $\alpha = \frac{t_1}{t_2}$, where α is ring round-trip loss coefficient, t_1 is the self coupling coefficient

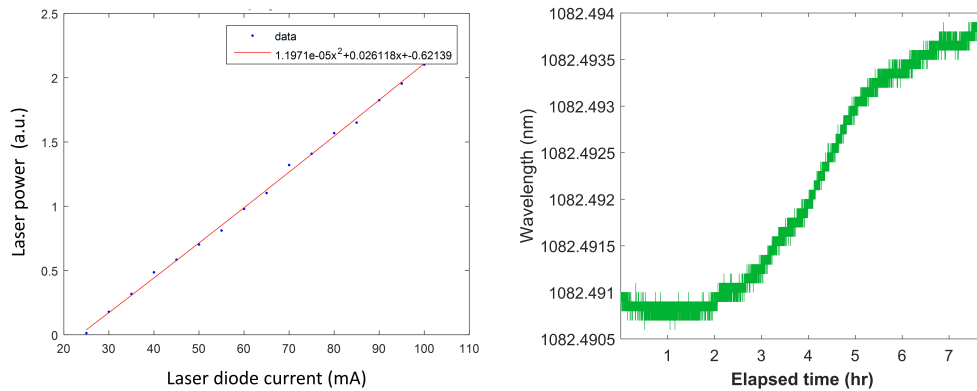


Figure 6.6: The ECDL power drift over 8 hours.

from input to throughput port and t_2 is self coupling coefficient from add to drop port. Because there is always loss ($\alpha \neq 1$), the symmetrical waveguide design that we used is never at critical coupling condition.

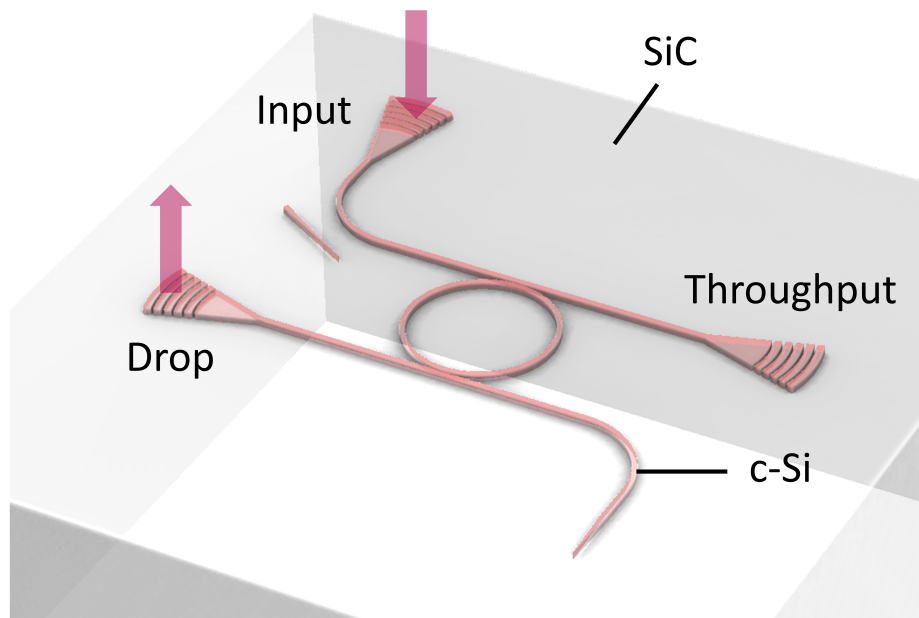


Figure 6.7: Main measurements were performed through the drop port.

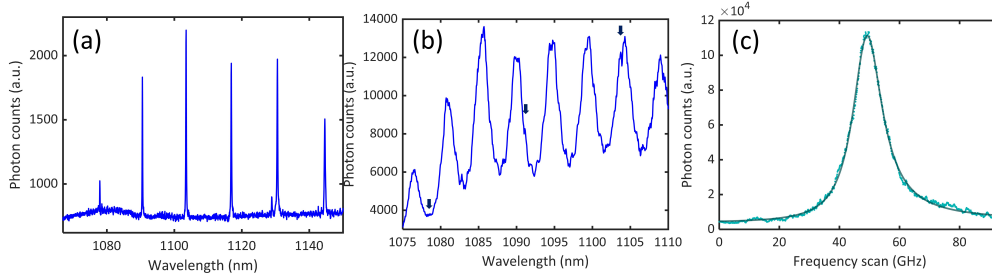


Figure 6.8: (a) Coarse measurement through the drop port with supercontinuum laser. (b) Coarse measurement through the throughput port. Arrows indicate the locations of resonances. (c) Fine measurement with tunable laser scanning. The Lorentzian fit reveals $Q \sim 23000$.

The Purcell factor for a qubit in hybrid cavities is [36]:

$$F_{ZPL} = \frac{3}{4\pi^2} \left(\frac{\lambda_{ZPL}}{n_c} \right)^3 \frac{n_c Q}{n_h V} \left| \frac{\mathbf{E}(\mathbf{r}_{qubit})}{\mathbf{E}(\mathbf{r}_{max})} \right|^2 \quad (6.1)$$

Based on simulation and measurements, the mode volume of the ring resonator is 19.5 and the best measured quality factor is 23000 at a wavelength of 1078 nm. This would result in a Purcell enhancement factor of 36 assuming perfect dipole alignment for an emitter located at 10 nm below the surface. The estimated Purcell enhancement factor for an emitter at a depth of 100 nm is 12 due to a 3 times smaller field.

6.1 Conclusion

We were able to fabricate on-chip silicon ring resonator on 4H-SiC with quality factor of 23000. The crystalline silicon membrane transfer method described in 5.4 can be used to successfully place membranes as a photonic device layer on silicon carbide and potentially other host materials. The smooth surface of crystalline silicon has the potential to achieve better quality factor than amorphous silicon devices. The change from a-Si to c-Si or using resist reflow technique only improved the quality factor by order of 2. This suggests the limiting factor is surface or material absorption of silicon used in this work.

*Chapter 7***CONCLUDING REMARKS**

In my Ph.D. projects, I fabricated Si on SiC hybrid ring resonators to couple ZPL emissions of divacancies in 4H-SiC. Photonic devices such as ring resonators can be used to enhance coherent emission for indistinguishable photons used in quantum networks. Quantum entanglement generation rate is a key measure for the distance at which quantum communication can be established. This rate scales linearly or with higher order with indistinguishable photon generation rate, which makes enhancing coherent emission of qubits an important engineering challenge.

Among different qubits, divacancy defects in 4H-SiC recently emerged as promising candidates with long spin coherence time and good optical stability compared to NV centers in diamond (See chapter 2). I also studied a few other impurities like Cr and Mo ions in 4H-SiC and they were found to possess relatively short $T_2 < 1 \mu\text{s}$, which does not satisfy the high fidelity qubit polarization condition. My research is mainly focused on divacancies in 4H-SiC and fabrication of photonic devices on 4H-SiC. The ZPL emission of divacancies is useful as indistinguishable photons for entanglement generation, which only consists of $\sim 5\%$ of total emission. In order to unleash the potential of divacancies it is important to enhance only the usable coherent emission with narrow-linewidth photonic devices. In my research I developed a fabrication method for silicon ring resonators on SiC (or on other materials). Silicon is used for the photonic device layer. This hybrid approach avoids charge build-up around the qubits, which is believed to degrade optical properties of the emitters. It is transparent and suitable for coupling divacancy's near IR wavelength from 1050 nm as shown in chapter 4.

4H-SiC is widely used for power electronics devices and readily available in mass production. Recently, a single divacancy residing in commercially available p-i-n diodes showed $T_2 \sim 1 \text{ ms}$ at 5K [92]. Integrating qubit host materials with classical semiconductor devices might be beneficial as a new type of quantum devices. The Si photonic devices shown in this thesis are compatible with this platform as long as divacancies are located in the proximity to the surface. Silicon integrated photonics is currently accepted as a next generation power-efficient classical telecommunication platform [93]. The advantage is low-cost and high-volume silicon photonic

on-chip devices manufacturing that is compatible to the CMOS technology. The Si hybrid devices can be readily integrated with a variety of Si components such as filters, multiplexers, modulators and sensors. Additionally, integration between silicon photonics and superconducting nanowire single photon detectors (SNSPDs) [94] can enable on-chip spin-spin entanglement platform and a range of quantum technologies.

For quantum emitters with lower than 1050 nm wavelength, different material is required for the optical device layer. For example, silicon vacancies (V_{Si}) in 4H-SiC exhibits ZPL at 860 and at 920 nm [95]. Materials such as GaAs with bandgap 1.44 eV (300 K) is transparent enough for silicon vacancies at low temperature. Currently, our group is developing GaAs hybrid photonic devices for Yb^{3+} ions in YVO with optical transition at 984 nm [96]. GaP with bandgap 2.24 eV (300 K) can be used for confining light with shorter wavelength > 600 nm including ZPL of NV centers in diamond at 637 nm [97].

Direct device fabrication on SiC membranes can achieve largest light confinement at the spot of qubits in SiC, achieving strong enhancement of the emission. Vuckovic group showed 4H-SiC photonic crystal on insulator with fusion bonding technique [98]. If this can be expanded to wafer scale bonding, mass production of on-chip quantum networks will be possible.

BIBLIOGRAPHY

- [1] Stephen Wiesner. “Conjugate coding”. In: *ACM Sigact News* 15.1 (1983), pp. 78–88.
- [2] Hoi-Kwong Lo, Marcos Curty, and Kiyoshi Tamaki. “Secure quantum key distribution”. In: *Nature Photonics* 8.8 (2014), p. 595.
- [3] Umesh Vazirani and Thomas Vidick. “Fully device independent quantum key distribution”. In: *Communications of the ACM* 62.4 (2019), pp. 133–133.
- [4] Peter JJ O’Malley et al. “Scalable quantum simulation of molecular energies”. In: *Physical Review X* 6.3 (2016), p. 031007.
- [5] Benjamin P Lanyon et al. “Towards quantum chemistry on a quantum computer”. In: *Nature chemistry* 2.2 (2010), p. 106.
- [6] John Preskill. “Quantum Computing in the NISQ era and beyond”. In: *Quantum* 2 (2018), p. 79.
- [7] Hannah Clevenson et al. “Broadband magnetometry and temperature sensing with a light-trapping diamond waveguide”. In: *Nature Physics* 11.5 (2015), p. 393.
- [8] Christian L Degen, F Reinhard, and P Cappellaro. “Quantum sensing”. In: *Reviews of modern physics* 89.3 (2017), p. 035002.
- [9] Quntao Zhuang, Zheshen Zhang, and Jeffrey H Shapiro. “Distributed quantum sensing using continuous-variable multipartite entanglement”. In: *Physical Review A* 97.3 (2018), p. 032329.
- [10] William K Wootters and Wojciech H Zurek. “A single quantum cannot be cloned”. In: *Nature* 299.5886 (1982), p. 802.
- [11] Yazhen Wang et al. “Quantum computation and quantum information”. In: *Statistical Science* 27.3 (2012), pp. 373–394.
- [12] H Jeff Kimble. “The quantum internet”. In: *Nature* 453.7198 (2008), p. 1023.
- [13] Jeremy L O’Brien, Akira Furusawa, and Jelena Vučković. “Photonic quantum technologies”. In: *Nature Photonics* 3.12 (2009), p. 687.
- [14] Stefano Pirandola and Samuel L Braunstein. “Physics: Unite to build a quantum Internet”. In: *Nature News* 532.7598 (2016), p. 169.
- [15] DL Moehring et al. “Quantum networking with photons and trapped atoms”. In: *JOSA B* 24.2 (2007), pp. 300–315.
- [16] JR Weber et al. “Quantum computing with defects”. In: *Proceedings of the National Academy of Sciences* 107.19 (2010), pp. 8513–8518.

- [17] Wolfgang Pfaff et al. “Unconditional quantum teleportation between distant solid-state quantum bits”. In: *Science* 345.6196 (2014), pp. 532–535.
- [18] Bas Hensen et al. “Loophole-free Bell inequality violation using electron spins separated by 1.3 kilometres”. In: *Nature* 526.7575 (2015), p. 682.
- [19] Michael A Nielsen and Isaac Chuang. *Quantum computation and quantum information*. 2000.
- [20] Stephanie Wehner, David Elkouss, and Ronald Hanson. “Quantum internet: A vision for the road ahead”. In: *Science* 362.6412 (2018), eaam9288.
- [21] Tatjana Wilk et al. “Single-atom single-photon quantum interface”. In: *Science* 317.5837 (2007), pp. 488–490.
- [22] Stephan Ritter et al. “An elementary quantum network of single atoms in optical cavities”. In: *Nature* 484.7393 (2012), p. 195.
- [23] Dietrich Leibfried et al. “Quantum dynamics of single trapped ions”. In: *Reviews of Modern Physics* 75.1 (2003), p. 281.
- [24] Lilian Childress and Ronald Hanson. “Diamond NV centers for quantum computing and quantum networks”. In: *MRS bulletin* 38.2 (2013), pp. 134–138.
- [25] David D Awschalom et al. “Quantum technologies with optically interfaced solid-state spins”. In: *Nature Photonics* 12.9 (2018), pp. 516–527.
- [26] Norbert Kalb et al. “Entanglement distillation between solid-state quantum network nodes”. In: *Science* 356.6341 (2017), pp. 928–932.
- [27] Andrei Faraon et al. “Coupling of nitrogen-vacancy centers to photonic crystal cavities in monocrystalline diamond”. In: *Physical review letters* 109.3 (2012), p. 033604.
- [28] Sara L Mouradian and Dirk Englund. “A tunable waveguide-coupled cavity design for scalable interfaces to solid-state quantum emitters”. In: *APL Photonics* 2.4 (2017), p. 046103.
- [29] Ajit Ram Verma and Padmanabhan Krishna. “Polymorphism and polytypism in crystals”. In: *1966, 341 P. JOHN WILEY AND SONS, INC., 605 THIRD AVENUE, NEW YORK, N. Y. 10016* (1965).
- [30] F Bechstedt et al. “Polytypism and properties of silicon carbide”. In: *physica status solidi (b)* 202.1 (1997), pp. 35–62.
- [31] Gary Lynn Harris. *Properties of silicon carbide*. 13. Iet, 1995.
- [32] William F Koehl et al. “Room temperature coherent control of defect spin qubits in silicon carbide”. In: *Nature* 479.7371 (2011), p. 84.
- [33] David J Christle et al. “Isolated electron spins in silicon carbide with millisecond coherence times”. In: *Nature materials* 14.2 (2015), p. 160.

- [34] Hosung Seo et al. “Quantum decoherence dynamics of divacancy spins in silicon carbide”. In: *Nature communications* 7 (2016), p. 12935.
- [35] Andreas Reiserer and Gerhard Rempe. “Cavity-based quantum networks with single atoms and optical photons”. In: *Reviews of Modern Physics* 87.4 (2015), p. 1379.
- [36] C Santori et al. “Nanophotonics for quantum optics using nitrogen-vacancy centers in diamond”. In: *Nanotechnology* 21.27 (2010), p. 274008.
- [37] Michael Gould et al. “Large-scale GaP-on-diamond integrated photonics platform for NV center-based quantum information”. In: *JOSA B* 33.3 (2016), B35–B42.
- [38] Greg Calusine, Alberto Politi, and David D Awschalom. “Cavity-enhanced measurements of defect spins in silicon carbide”. In: *Physical Review Applied* 6.1 (2016), p. 014019.
- [39] Peter C Humphreys et al. “Deterministic delivery of remote entanglement on a quantum network”. In: *Nature* 558.7709 (2018), p. 268.
- [40] Edward M Purcell, H Co Torrey, and Robert V Pound. “Resonance absorption by nuclear magnetic moments in a solid”. In: *Physical review* 69.1-2 (1946), p. 37.
- [41] Adam Gali et al. “Theory of neutral divacancy in SiC: a defect for spintronics”. In: *Materials Science Forum*. Vol. 645. Trans Tech Publ. 2010, pp. 395–397.
- [42] A Lenef and SC Rand. “Electronic structure of the N-V center in diamond: Theory”. In: *Physical Review B* 53.20 (1996), p. 13441.
- [43] MW Doherty et al. “Theory of the ground-state spin of the NV- center in diamond”. In: *Physical Review B* 85.20 (2012), p. 205203.
- [44] David J Christle et al. “Isolated spin qubits in SiC with a high-fidelity infrared spin-to-photon interface”. In: *Physical Review X* 7.2 (2017), p. 021046.
- [45] Kevin C Miao et al. “Electrically driven optical interferometry with spins in silicon carbide”. In: *arXiv preprint arXiv:1905.12780* (2019).
- [46] Abram L Falk et al. “Electrically and mechanically tunable electron spins in silicon carbide color centers”. In: *Physical review letters* 112.18 (2014), p. 187601.
- [47] Jeronimo R Maze et al. “Properties of nitrogen-vacancy centers in diamond: the group theoretic approach”. In: *New Journal of Physics* 13.2 (2011), p. 025025.
- [48] NT Son et al. “Photoluminescence and Zeeman effect in chromium-doped 4H and 6H SiC”. In: *Journal of applied physics* 86.8 (1999), pp. 4348–4353.
- [49] Daniel C Harris and Michael D Bertolucci. *Symmetry and spectroscopy: an introduction to vibrational and electronic spectroscopy*. Courier Corporation, 1989.

- [50] Bodie E Douglas and Charles A Hollingsworth. *Symmetry in bonding and spectra: An introduction*. Academic Press, 2012.
- [51] F Albert Cotton. *Chemical applications of group theory*. John Wiley & Sons, 2003.
- [52] Yukito Tanabe and Satoru Sugano. “On the absorption spectra of complex ions II”. In: *Journal of the Physical Society of Japan* 9.5 (1954), pp. 766–779.
- [53] C Deka et al. “Optical spectroscopy of Cr 4+: Y 2 SiO 5”. In: *JOSA B* 10.9 (1993), pp. 1499–1507.
- [54] Hergen Eilers et al. “Spectroscopy and dynamics of Cr 4+: Y 3 Al 5 O 12”. In: *Physical Review B* 49.22 (1994), p. 15505.
- [55] William F Koehl et al. “Resonant optical spectroscopy and coherent control of Cr 4+ spin ensembles in SiC and GaN”. In: *Physical Review B* 95.3 (2017), p. 035207.
- [56] Sergey A Reshanov. “Growth and high temperature performance of semi-insulating silicon carbide”. In: *Diamond and Related Materials* 9.3-6 (2000), pp. 480–482.
- [57] Karin Maier, Harald D Müller, and Jürgen Schneider. “Transition metals in silicon carbide (SiC): vanadium and titanium”. In: *Materials Science Forum*. Vol. 83. Trans Tech Publ. 1992, pp. 1183–1194.
- [58] K Maier et al. “Electron spin resonance studies of transition metal deep level impurities in SiC”. In: *Materials Science and Engineering: B* 11.1-4 (1992), pp. 27–30.
- [59] M Kunzer, HD Müller, and U Kaufmann. “Magnetic circular dichroism and site-selective optically detected magnetic resonance of the deep amphoteric vanadium impurity in 6H-SiC”. In: *Physical Review B* 48.15 (1993), p. 10846.
- [60] Gary Wolfowicz et al. “Vanadium spin qubits as telecom quantum emitters in silicon carbide”. In: *arXiv preprint arXiv:1908.09817* (2019).
- [61] Viktor Ivady et al. “Asymmetric split-vacancy defects in SiC polytypes: A combined theoretical and electron spin resonance study”. In: *Physical review letters* 107.19 (2011), p. 195501.
- [62] Andreas Gällström, Björn Magnusson, and Erik Janzén. “Optical identification of Mo related deep level defect in 4H and 6H SiC”. In: *Materials Science Forum*. Vol. 615. Trans Tech Publ. 2009, pp. 405–408.
- [63] Andreas Gällström et al. “A defect center for quantum computing: Mo in SiC”. In: (2015).
- [64] J Baur, M Kunzer, and J Schneider. “Transition metals in SiC polytypes, as studied by magnetic resonance techniques”. In: *physica status solidi (a)* 162.1 (1997), pp. 153–172.

- [65] Tom Bosma et al. “Identification and tunable optical coherent control of transition-metal spins in silicon carbide”. In: *npj Quantum Information* 4.1 (2018), p. 48.
- [66] M Steger et al. “Reduction of the Linewidths of Deep Luminescence Centers in Si 28 Reveals Fingerprints of the Isotope Constituents”. In: *Physical review letters* 100.17 (2008), p. 177402.
- [67] Hisashi Sumikura et al. “Ultrafast spontaneous emission of copper-doped silicon enhanced by an optical nanocavity”. In: *Scientific reports* 4 (2014), p. 5040.
- [68] Feng Tian et al. “All-optical dynamic modulation of spontaneous emission rate in hybrid optomechanical cavity quantum electrodynamics systems”. In: *arXiv preprint arXiv:1901.07691* (2019).
- [69] Michael Lurie Goldman et al. “Phonon-induced population dynamics and intersystem crossing in nitrogen-vacancy centers”. In: *Physical review letters* 114.14 (2015), p. 145502.
- [70] Martin A Green. “Self-consistent optical parameters of intrinsic silicon at 300 K including temperature coefficients”. In: *Solar Energy Materials and Solar Cells* 92.11 (2008), pp. 1305–1310.
- [71] KG Svantesson and NG Nilsson. “Determination of the temperature dependence of the free carrier and interband absorption in silicon at 1.06 μm ”. In: *Journal of Physics C: Solid State Physics* 12.18 (1979), p. 3837.
- [72] Dominik G Rabus. *Integrated ring resonators*. Springer, 2007.
- [73] Wim Bogaerts et al. “Silicon microring resonators”. In: *Laser & Photonics Reviews* 6.1 (2012), pp. 47–73.
- [74] Charles Kittel, Paul McEuen, and Paul McEuen. *Introduction to solid state physics*. Vol. 8. Wiley New York, 1996.
- [75] Allen Taflove and Susan C Hagness. *Computational electrodynamics: the finite-difference time-domain method*. Artech house, 2005.
- [76] Kane Yee. “Numerical solution of initial boundary value problems involving Maxwell’s equations in isotropic media”. In: *IEEE Transactions on antennas and propagation* 14.3 (1966), pp. 302–307.
- [77] Ardavan F Oskooi et al. “MEEP: A flexible free-software package for electromagnetic simulations by the FDTD method”. In: *Computer Physics Communications* 181.3 (2010), pp. 687–702.
- [78] Gary Wolfowicz et al. “Optical charge state control of spin defects in 4H-SiC”. In: *Nature communications* 8.1 (2017), p. 1876.

- [79] James F Ziegler, Matthias D Ziegler, and Jochen P Biersack. “SRIM—The stopping and range of ions in matter (2010)”. In: *Nuclear Instruments and Methods in Physics Research Section B: Beam Interactions with Materials and Atoms* 268.11-12 (2010), pp. 1818–1823.
- [80] WE Carlos et al. “Annealing of multivacancy defects in 4H-SiC”. In: *Physical Review B* 74.23 (2006), p. 235201.
- [81] Andreas Gällström et al. “Influence of Cooling Rate after High Temperature Annealing on Deep Levels in High-Purity Semi-Insulating 4H-SiC”. In: *Materials science forum*. Vol. 556. Trans Tech Publ. 2007, pp. 371–374.
- [82] Jae-Hyung Lee et al. “Smart-cut layer transfer of single-crystal SiC using spin-on-glass”. In: *Journal of Vacuum Science & Technology B, Nanotechnology and Microelectronics: Materials, Processing, Measurement, and Phenomena* 30.4 (2012), p. 042001.
- [83] Joohyun Koh et al. “Correlation of real time spectroellipsometry and atomic force microscopy measurements of surface roughness on amorphous semiconductor thin films”. In: *Applied physics letters* 69.9 (1996), pp. 1297–1299.
- [84] YA Kryukov et al. “Experimental and theoretical study of the evolution of surface roughness in amorphous silicon films grown by low-temperature plasma-enhanced chemical vapor deposition”. In: *Physical Review B* 80.8 (2009), p. 085403.
- [85] Michio Kondo et al. “Substrate dependence of initial growth of microcrystalline silicon in plasma-enhanced chemical vapor deposition”. In: *Journal of applied physics* 80.10 (1996), pp. 6061–6063.
- [86] H Fujiwara et al. “Assessment of effective-medium theories in the analysis of nucleation and microscopic surface roughness evolution for semiconductor thin films”. In: *Physical Review B* 61.16 (2000), p. 10832.
- [87] Luozhou Li et al. “Nanofabrication on unconventional substrates using transferred hard masks”. In: *Scientific reports* 5 (2015), p. 7802.
- [88] Gary E McGuire. “Semiconductor Materials and Process Technology Handbook for Very Large Scale Integration(VLSI) and Ultra Large Scale Integration(ULSI)”. In: *Noyes Data Corporation, Noyes Publications, Mill Rd. at Grand Ave, Park Ridge, New Jersey 07656, USA, 1988. 675 (1988), pp. 46–72.*
- [89] J Baro et al. “PENELOPE: an algorithm for Monte Carlo simulation of the penetration and energy loss of electrons and positrons in matter”. In: *Nuclear Instruments and Methods in Physics Research Section B: Beam Interactions with Materials and Atoms* 100.1 (1995), pp. 31–46.
- [90] Matthew Borselli, Thomas J Johnson, and Oskar Painter. “Beyond the Rayleigh scattering limit in high-Q silicon microdisks: theory and experiment”. In: *Optics express* 13.5 (2005), pp. 1515–1530.

- [91] C Petridis et al. “Mode-hop-free tuning over 80 GHz of an extended cavity diode laser without antireflection coating”. In: *Review of Scientific Instruments* 72.10 (2001), pp. 3811–3815.
- [92] Christopher P Anderson et al. “Electrical and optical control of single spins integrated in scalable semiconductor devices”. In: *Science* 366.6470 (2019), pp. 1225–1230.
- [93] David Thomson et al. “Roadmap on silicon photonics”. In: *Journal of Optics* 18.7 (2016), p. 073003.
- [94] Simone Ferrari, Carsten Schuck, and Wolfram Pernice. “Waveguide-integrated superconducting nanowire single-photon detectors”. In: *Nanophotonics* 7.11 (2018), pp. 1725–1758.
- [95] David O Bracher, Xingyu Zhang, and Evelyn L Hu. “Selective Purcell enhancement of two closely linked zero-phonon transitions of a silicon carbide color center”. In: *Proceedings of the National Academy of Sciences* 114.16 (2017), pp. 4060–4065.
- [96] Jonathan M Kindem et al. “Characterization of Yb 3+ 171: YVO 4 for photonic quantum technologies”. In: *Physical Review B* 98.2 (2018), p. 024404.
- [97] Emma R Schmidgall et al. “Frequency control of single quantum emitters in integrated photonic circuits”. In: *Nano letters* 18.2 (2018), pp. 1175–1179.
- [98] Daniil M Lukin et al. “4H-silicon-carbide-on-insulator for integrated quantum and nonlinear photonics”. In: *Nature Photonics* (2019), pp. 1–5.
- [99] Qimin Quan and Marko Loncar. “Deterministic design of wavelength scale, ultra-high Q photonic crystal nanobeam cavities”. In: *Optics express* 19.19 (2011), pp. 18529–18542.

Appendix A

GAAS PHOTONIC CRYSTALS

This chapter describes initial attempts of fabricating GaAs photonic crystal devices for coupling Yb^{3+} ions in YVO_4 with optical transition at 984 nm [96]. This only shows the starting point of the fabrication optimization and parameters or procedures described here will be greatly improved in the future. The plan of fabrication of GaAs devices is as following. They are first fabricated on GaAs-AlGaAs-GaAs substrate then undercut to be released from the substrate. We use a nanomanipulator to pick up a device and transfer it deterministically on YVO_4 substrate.

GaAs periodic photonic crystal band diagram

In this simulation, we simulate only a unit lattice of a periodic PhC and see if there are forbidden modes (bandgap) exist so the PhC will reflect those mode propagating inside acting like a mirror. We sweep parameters (width, height, hole period and hole radius) with initial guess chosen based on the strategy described in Quan and Loncar [99]. The goal is to find a parameter set that gives a wide bandgap around wavelength 980 nm with GaAs layer height around 240nm which corresponds to the top layer height of GaAs/AlGaAs/GaAs samples we had for tests. The PhC refractive index is set to GaAs and the surrounding medium including holes in PhC are air. The optimized parameters are (width, height, hole period and hole radius) = (1, 0.7, 1, 0.25) that corresponds to (343 nm, 240 nm, 343 nm, 86 nm) if set height to 240 nm. The band diagram with these parameters is shown in figure A.1. The second 3D simulation is to check that the partial periodic PhC acts as a mirror. In this configuration, shown in figure A.2, PhC with 3 holes is sandwiching a defect at the center. A light source at the center generates field around the wavelength of the bandgap center. A harmonic inversion function recognizes the resonance created with the structure, thus supporting the result of the previous bandgap simulation.

A.1 GaAs photonic crystal fabrication

The first attempt of GaAs photonic crystal was based on the parameters described in the previous section mainly to optimize dry etching recipe and device transfer. The initial dry etching recipe of ICP-RIE etcher is based on $\text{Ar}:\text{SiCl}_4=3:10$ flow rate. With varying RF/ICP power, the etched sidewall remained rough.

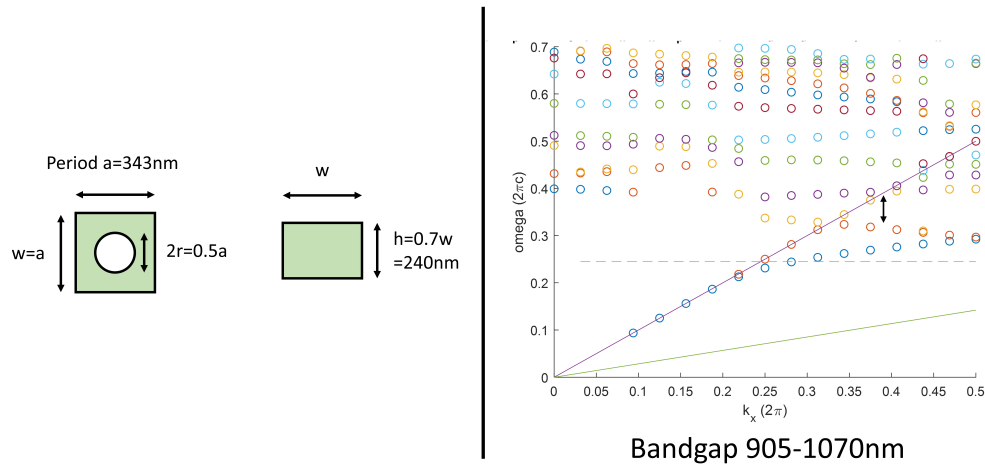


Figure A.1: 3D periodic photonic crystal bandgap simulation.

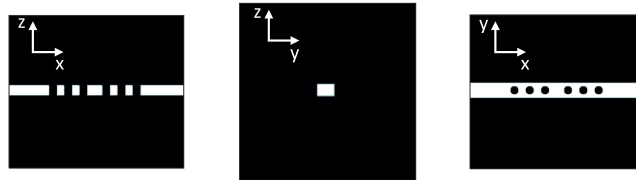


Figure A.2: 3D photonic crystal simulation with defect at the center

AlGaAs undercut

The undercut procedure for 100 nm thickness AlGaAs is shown in the following table ??.

Photonic crystal transfer by nanomanipulator

Transferring smaller structures or single photonic devices to desired location can be performed using a nanomanipulator. In the FIB/SEM system, this methods allows for device examination in microscopic level and transfer at the same time. In this method, platinum is deposited where we want to hold and is welded to the probe. In order to avoid deposition on the device itself, We patterned two lines along with the PhC and cut and transfer a larger area including the device with FIB as shown in A.3.

Procedure	time (s)
Dip in citric acid	60
Dip in 3.5% HF	3
Dip in water	10
Repeat dipping in HF then water twice	9 total HF dip time
Dip in citric acid	60
Put still wet sample to IPA, gently take out (never blow dry)	

Table A.1: a-Si recipe

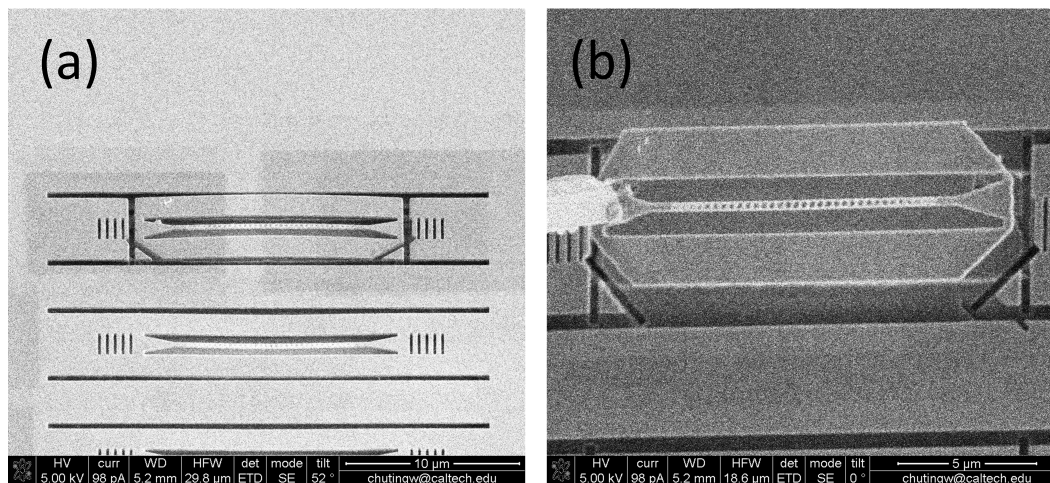


Figure A.3: Transferring a part of devices using a nanomanipulator (a) Cut through between the 2 patterned lines before grating couplers because undercut wasn't enough to detach grating couplers from the substrate (b) The probe at the left side is welded to platinum, deposited around the grating tapered part, and the device is lifted up.

Appendix B

RELATED CODES

Si oxidation time estimation based on desired thickness

```

1 % Calculates oxidation rate from Equations taken from a chapter written by
2 % B. E. Deal in Semiconductor materials and process technology handbook
3 %: for very large scale integration (VLSI) and ultra large scale integration (ULSI)
4 %/ edited by Gary E. McGuire. (pp. 48-57)
5
6 %Input%%%%%%%%%%%%%%%%%%%%%%%%%%%%%%%%%%%%%%%%%%%%%%%%%%%%%%%%%%%%%%%%%%%%%%%%%
7 mode=1;%Oxidation condition 1:wet,2:dry
8 siori=1;%Si orientation 1:(100),2:(111)
9 T=1000;%Temperature in Celcius
10 xi=2.5;%Initial oxide thickness (nm)
11 xsi=250;%Final thickness of Si consumed (nm), e.g. if you have 500nm Si and
12     %want to make it 360nm, xsi=140nm
13
14 fit=1; %Fit the actual data below to scale the theoretical curve. 1:yes,2:no
15 %Actual data of time(hr) and xsi(um)
16
17 % %Newer wet oxidation data (after 3/24 when furnace 1 is replaced with new tube)
18 p1=[4/3,0.24176];%(hr,(oxidized si thickness)um)
19 p2=[32/60,0.13901];
20 p3=[1.5,0.26377];
21
22 %Newer dry oxidation data
23 % p1=[0.3,0.01146];
24 % p2=[0.1667,0.00676];
25
26 data=cat(1,p1,p2,p3);
27
28
29 %Basic calculation%%%%%%%%%%%%%%%%%%%%%%%%%%%%%%%%%%%%%%%%%%%%%%%%%%%%%%%%%%%%%%%%%%%%%%%%%
30 oxd=2.20*10^22;%molecular density of SiO2 (/cm^3)
31 sid=4.99*10^22; %Atomic density of Si(/cm^3)
32 %Oxide thickness:consumed Si thickness=
33
34 xo=xsi*sid/oxd;%Final oxide thickness (nm)
35 fprintf('Final oxide thickness %f\n\n',xo)
36
37 xi=xi/1000;%change units to um
38 xo=xo/1000;
39 %%%%%%%%%%%%%%%%%%%%%%%%%%%%%%%%%%%%%%%%%%%%%%%%%%%%%%%%%%%%%%%%%%%%%%%%%%
40
41 %Parameters for oxidation thickness equation%%%%%%%%%%%%%%%%%%%%%%%%%%%%%%%%%%%%%%%%%%%%%%%%%%%%%%%%%%%%%%%%%%%%%%%%%
42 C1d=7.72*10^2;%(um^2/hr)
43 C2d=6.23*10^6;%(um/hr)
44 E1d=1.23; %(eV)
45 E2d=2.0;
46
47 C1w=3.86*10^2;
48 C2w=1.63*10^8;
49 E1w=0.78; %(eV)
50 E2w=2.05;
51 k=8.617*10^(-5);%eV/K
52 %%%%%%%%%%%%%%%%%%%%%%%%%%%%%%%%%%%%%%%%%%%%%%%%%%%%%%%%%%%%%%%%%%%%%%%%%%
53
54 if siori==1
55     C2d=C2d/1.7;
56     C2w=C2w/1.7;

```

Si oxidation time estimation based on desired thickness

```

57 end
58
59 switch mode
60     case 1
61         B=C1w*exp(-E1w/k/(T+273));
62         B_A=C2w*exp(-E2w/k/(T+273));
63
64     case 2
65         B=C1d*exp(-E1d/k/(T+273));
66         B_A=C2d*exp(-E2d/k/(T+273));
67     end
68     A=B/B_A;
69
70     %Oxidation thickness
71     tau=xi^2/B+xi/B_A;
72     t=xo/B_A+xo^2/B-tau;% calculate the time needed to have final ox thickness
73     t_list=linspace(0,2*t,300);
74     xo_list=1/2*(-A+sqrt(A^2+4*B*t_list+4*B*tau));
75     hr=floor(t);
76     min=floor((t-hr)*60);
77     sec=floor(((t-hr)*60-min)*60);
78     fprintf('Theory oxidation time %d:%d:%d\n',hr,min,sec)
79
80     %Fitting actual data%%%%%%%%%%%%%%%%%%%%%%%%%%%%%%%%%
81     if fit==1
82         xop=data(:,2)*sid/oxd;%oxide thickness for data
83         func=@(a,t_data)(1/2*(-a(1)+sqrt(a(1)^2+4*a(2)*t_data+4*a(2)*tau)));
84         iguess=[A,B];
85         [beta,R]=nlinfit(data(:,1),xop,func,iguess,statset('MaxIter', 1e6));
86         xo_scaled=1/2*(-beta(1)+sqrt(beta(1)^2+4*beta(2)*t_list+4*beta(2)*tau));
87         t_scaled=xo*beta(1)/beta(2)+xo^2/beta(2)-tau;
88
89         shr=floor(t_scaled);
90         smin=floor((t_scaled-shr)*60);
91         ssec=floor(((t_scaled-shr)*60-smin)*60);
92         fprintf('Scaled theory oxidation time %d:%d:%d\n',shr,smin,ssec)
93         %%%%%%%%%%%%%%%%%%%%%%%%%%%%%%%%%%
94
95         plot(t_list,xo_list,t_list,xo_scaled,'r',data(:,1),xop,'ro')
96         legend('Theory','Scaled theory','data')
97         title('Oxidation calculation')
98         ylabel('Oxide thickness (um)')
99         xlabel('time (hr)')
100     else
101         plot(t_list,xo_list)
102         ylabel('Oxide thickness (um)')
103         xlabel('time (hr)')
104     end
105
106
107

```

B.1 MEEP codes

2D cylindrical ring resonator simulation

```

C:\Users\Faraon Lab\Documents\Andrej_lab\MEEP\20180927_c-Si_ring_on_SiC_Q_vs_gap\2DRing_Si_on_SiC_TM_2D.cfl
Wednesday, September 11, 2019 3:40 PM

(define-param xo 0)
(define-param yo 0)
(define-param h 0.36) ;height of the ring
(define-param radi 3.75) ;external radius of the ring
(define-param w 0.30) ;width of the ring
(define-param res 40) ;resolution
(define-param fcen 0.9341) ; pulse center frequency 1070nm
(define-param df 0.005) ; pulse width (in frequency)
(define-param tim 1000) ;running time
(define-param dpml 0.5) ; thickness of PML (one side)
(define-param pad 0.5) ; thickness of pad b/w PML and edge of the ring (one side)

(define n_Si 3.550) ; refractive index of c-Si at 1070nm
(define n_SiC 2.637) ; refractive index of SiC

(define-param sx (+(* radi 2) (* dpml 2) (* pad 2)))
(define-param sy (+(* radi 2) (* dpml 2) (* pad 2)))

(set! geometry-lattice (make lattice (size sx sy no-size)))

(set! default-material (make medium (index 1))) ; air

(set! geometry (list
  (make cylinder (center xo yo) (radius radi) (height infinity)
    (material (make dielectric (index n_Si)))) ; Si ring
  (make cylinder (center xo yo (/ h 2)) (radius (- radi w)) (height infinity)
    (material (make dielectric (index 1)))) ; center hole
))

(set! pml-layers (list (make pml (thickness dpml))))

(set! sources (list
  (make source
    (src (make gaussian-src (frequency fcen) (fwidth df)))
    (component Ez)
    (center (+ xo (- radi (/ w 2))) yo) (size h h)
  ))

(set-param! resolution res) ;Resolution

(run-sources+ tim
  (at-beginning output-epsilon)
  (after-sources (harminv Ex (vector3 (+ xo (- radi (/ w 2))) yo) fcen df))
  (after-sources (harminv Ez (vector3 (+ xo (- radi (/ w 2))) yo) fcen df))
)

(run-until (/ 1 fcen) (at-every (/ 1 fcen 8) output-efield))

```

3D ring resonator with waveguides simulation

```

C:\Users\Faraon Lab\Documents\Andrej_lab\MEEP\20180927_c-Si_ring_on_SiC_Q_vs_gap\3DRing_Si_on_SiC_wg_TM.ctf
Wednesday, September 11, 2019 3:43 PM

(define-param xo 0)
(define-param yo 0)
(define-param h 0.36) ;height of the ring
(define-param radi 3.75) ;external radius of the disk
(define-param w 0.3) ;width of the ring
(define-param sp 0.3) ;ring waveguide spacing
(define-param wgw 0.3) ;width of the waveguide

(define-param res 40) ;resolution
(define-param fcen 0.9285) ; pulse center frequency 1070nm
(define-param df 0.01) ; pulse width (in frequency)
(define-param tim 1000) ;running time
(define-param dpml 0.5) ; thickness of PML
(define-param pad 0.5) ; thickness of pad b/w PML and edge of the ring (one side)

(define n_Si 3.550) ; refractive index of Si at 1070nm
(define n_SiC 2.637) ; refractive index of SiC

(define-param sx (+(* radi 2) (* dpml 2) (* pad 2)))
(define-param sy (+(* radi 2) (* dpml 2) (* pad 2) (* sp 2) (* wgw 2)))
(define-param sz (+ h (* dpml 2) (* pad 2)))

(set! geometry-lattice (make lattice (size sx sy sz)))

(set! default-material (make medium (index 1))) ; air

;(define-param guide? true);

(set! geometry (list
  (make block (center xo yo (/ sz -4)) (size sx sy (/ sz 2))
    (material (make dielectric (index n_SiC)))) ; SiC substrate
  (make cylinder (center xo yo (/ h 2)) (radius radi) (height h) (axis 0 0 1)
    (material (make dielectric (index n_Si)))) ; Si ring
  (make cylinder (center xo yo (/ h 2)) (radius (- radi w)) (height h) (axis 0 0 1)
    (material (make dielectric (index 1)))) ; center hole
  (make block (center xo (+ yo (* radi -1) (* sp -1) (* wgw -0.5)) (/ h 2)) (size sx
    wgw h)
    (material (make dielectric (index n_Si)))) ; waveguide
  (make block (center xo (+ yo radi sp (* wgw 0.5)) (/ h 2)) (size sx wgw h)
    (material (make dielectric (index n_Si))))
))

(set! pml-layers (list (make pml (thickness dpml))))

(set! sources (list
  (make source
    (src (make gaussian-src (frequency fcen) (fwidth df)))
    (component Ez)
    (center (+ xo radi (/ w -2)) yo (/ h 4)) (size h h h))
))

(set-param! resolution res)

(run-sources+ tim
  (at-beginning output-epsilon)
  (after-sources (harminv Ez (vector3 (+ xo radi (/ w -2)) yo (/ h 4)) fcen df))
)

```

3D ring resonator with waveguides simulation

C:\Users\Faraon.Lab\Documents\Andrej_lab\WEEPI\20180927_c-Si_ring_on_SiC_Q_vs_gap\3D\Ring_Si_on_SiC_wg_TM.ctb Wednesday, September 11, 2019 3:43 PM
(run-until (/ 1 fcen) (at-every (/ 1 fcen 4) output-efield))

2D grating coupler flux simulation

```

C:\Users\Faroon Lab\Documents\Andrej_lab\MEEP\20170418_c-Si_ring_on_SiC\2D grating for TM2D_Si_grating_flux_TM.ctl
Wednesday, September 11, 2019 3:35 PM
; 2D waveguide with gratings on the right, source in the waveguide polarized in the TM
direction (Ey)

(define-param per 1.00)
(define-param duty 0.2)
(define-param h 0.54)
(define-param dpml 0.5)

(define sx 15)
(define sy 10)

(define-param ref false); if true, it's just a waveguide

(define n_Si 3.550) ; refractive index of Si at 1070nm
(define n_SiC 2.637) ; refractive index of SiC

(define-param fcen 0.9341) ; pulse center frequency 1070nm
(define-param df 0.01) ; pulse width (in frequency)

(define-param nfreq 10) ; number of frequencies at which to compute flux
(set-param! resolution 40) ; simulation resolution

(set! geometry-lattice (make lattice (size sx sy no-size)))

(set! geometry
  (append
    (list
      (make block (center 0 (+ (/ sy -4) (/ h 2))) (size sx h) ;Grating
        (material (make dielectric (index n_Si))))
      (make block (center 0 (* sy (/ -3 8))) (size sx (/ sy 4)) ;Substrate
        (material (make dielectric (index n_SiC))))
      (geometric-object-duplicates (vector3 per 0 0) 0 36 ;Grating trenches
        (make block
          (center (/ sx -4) (+ (/ sy -4) (/ h 2)))
          (size (* (- 1 duty) per) h)
          (material (make dielectric (index 1)))))))

(set! pml-layers (list (make pml (thickness dpml))))

(set! sources (list (make source
  (src (make gaussian-src (frequency fcen) (fwidth
    df)))
  (component Ey) (center (+ (/ sx -2) dpml 0.1) (+ (/ sy -4) (/ h 2))) (size 0 h))))

(define trans ; transmitted flux to y direction
  (add-flux fcen df nfreq
    (make flux-region
      (center (- (/ sx 8) (/ dpml 2)) (- (/ sy 2) dpml 0.5)) (size (- (* sx
        0.75) dpml) 0))))
(define trans2 ;transmitted flux to x
direction
  (add-flux fcen df nfreq
    (make flux-region
      (center (- (/ sx 2) dpml 0.5) (/ sy 8)) (size 0 (- (* sy 0.75) 2))))

(run-sources+
  (stop-when-fields-decayed 50 Ey
    (vector3 (+ (/ sx -2) dpml 0.1) (+ (/ sy -4) (/ h 2)))
    1e-3)
  )

```

2D grating coupler flux simulation

```
C:\Users\Faraon.Lab\Documents\Andrej_lab\WEEP\20170418_c-Si_ring_on_SiC\2D grating for TM2D_Si_grating_flux_TM.ctl      Wednesday, September 11, 2019 3:35 PM
;(run-until 50 (at-beginning output-epsilon) (at-every 10 output-efield) )
(display-fluxes trans trans2)
```

2D grating coupler flux normalization (simple waveguide)

```

C:\Users\Faraon Lab\Documents\Andrej_lab\MEEP\20170418_c-Si_ring_on_SiC\2D grating for TM\2D_Si_wg_on_SiC_TM.ctl
Wednesday, September 11, 2019 3:36 PM
; 2D waveguide with gratings on the right, source in the waveguide polarized in the TM direction

(define-param h 0.54)
(define-param dpml 0.5)

(define sx 15)
(define sy 10)

(define n_Si 3.550) ; refractive index of Si at 1070nm
(define n_SiC 2.637) ; refractive index of SiC

(define-param fcen 0.9341) ; pulse center frequency 1070nm
(define-param df 0.01) ; pulse width (in frequency)

(define-param nfreq 10) ; number of frequencies at which to compute flux
(set-param! resolution 40) ; simulation resolution

(set! geometry-lattice (make lattice (size sx sy no-size)))
(set! default-material (make medium (index 1))) ; air

(set! geometry
  (list
    (make block (center 0 (+ (/ sy -4) (/ h 2))) (size sx h)
      (material (make dielectric (index n_Si))))
    (make block (center 0 (* sy (/ -3 8))) (size sx (/ sy 4))
      (material (make dielectric (index n_SiC)))))

(set! pml-layers (list (make pml (thickness dpml))))

(set! sources (list (make source
  (src (make gaussian-src (frequency fcen) (fwidth
    df)))
  (component Ey) (center (+ (/ sx -2) dpml 0.1) (+ (/ sy -4) (/ h 2))) (size 0 h))))

(define fluxi ;initial flux (corresponding right at the starting point of grating in other
programs)
  (add-flux fcen df nfreq
    (make flux-region
      (center (/ sx -4) (+ (/ sy -4) (/ h 2))) (size 0 (* h 2)))))
(define fluxf ;flux go through the end
  (add-flux fcen df nfreq
    (make flux-region
      (center (- (/ sx 2) dpml 0.1) (+ (/ sy -4) (/ h 2))) (size 0 (* h 2)))))

(run-until 150
  (at-beginning output-epsilon)
  (at-end output-efield))

(run-sources+
  (stop-when-fields-decayed 50 Ey
    (vector3 (- (/ sx 2) dpml 0.1) (+ (/ sy -4) (/ h 2))) 1e-4))
;(run-until (/ 1 fcen) (at-every (/ 1 fcen 8) output-efield))

(display-fluxes fluxi fluxf)

```

3D grating coupler flux simulation

```

C:\Users\Faraon Lab\Documents\Andrej_lab\MEEP\20170418_c-Si_ring_on_SiC\3D grating for TMSI_curved_grating_on_SiC_flux_TM.ctf  Wednesday, September 11, 2019 3:31 PM
; TM mode (Ez)

(define-param wgh 0.24) ;height of the waveguide + grating
(define-param wgl 0.50) ;length of the waveguide (doesn't include pad or dpml)
(define-param wgw 0.40) ;width of the waveguide
(define-param gangle (* (/ 105 180) pi)) ;Full angle of the grating (deg)
(define ga (* (/ gangle 180) pi));Full angle of the grating (rad)
(define-param gper 0.470) ;grating period
(define-param gduty 0.82) ;duty cycle of the grating
(define ggap (* gper (- 1 gduty))) ;width of the grating gap
(define-param gn 6) ;Grating number
(define-param i 0)

(define-param res 40) ;resolution
(define-param fcen 0.9341) ; pulse center frequency 1070nm
(define-param df 0.01) ; pulse width (in frequency)
(define-param tim 100) ;running time
(define-param dpml 0.5) ; thickness of PML (one side)
(define-param pad 0.5) ; thickness of pad b/w PML and edge of the ring (one side)

(define-param n_Si 3.550) ; refractive index of c-Si at 1070nm
(define-param n_SiC 2.637) ; refractive index of SiC
(define-param nfreq 10) ; number of frequencies at which to compute flux

(define sx (- (+ wgl (* gper 6) (* pad 2) (* dpml 2)) ggap))
(define sy (+ (* pad 2) (* dpml 2) (* (sin (/ ga 2)) gper 12)))
(define sz 7.5)

(set! geometry-lattice (make lattice (size sx sy sz)))

(set! default-material (make medium (index 1))) ; air

(set! geometry (list

  (make cylinder (center (- (+ (/ sx -2) dpml pad wgl) ggap) 0 (+ (/ sz -4) (/ wgh
  2))) (radius (* gper 6)) (height wgh) (axis 0 0 1)
  (material (make dielectric (index n_Si)))) ; c-Si cylinder (most outer grating
  one)

  (make cylinder (center (- (+ (/ sx -2) dpml pad wgl) ggap) 0 (+ (/ sz -4) (/ wgh
  2))) (radius (- (* gper 6) (- gper ggap))) (height wgh) (axis 0 0 1)
  (material (make dielectric (index 1)))) ; air cylinder (make a grating
  shape)

  (make cylinder (center (- (+ (/ sx -2) dpml pad wgl) ggap) 0 (+ (/ sz -4) (/ wgh
  2))) (radius (* gper 5)) (height wgh) (axis 0 0 1)
  (material (make dielectric (index n_Si)))) ; c-Si cylinder (most outer grating
  one)

  (make cylinder (center (- (+ (/ sx -2) dpml pad wgl) ggap) 0 (+ (/ sz -4) (/ wgh
  2))) (radius (- (* gper 5) (- gper ggap))) (height wgh) (axis 0 0 1)
  (material (make dielectric (index 1)))) ; air cylinder (make a grating shape)

  (make cylinder (center (- (+ (/ sx -2) dpml pad wgl) ggap) 0 (+ (/ sz -4) (/ wgh
  2))) (radius (* gper 4)) (height wgh) (axis 0 0 1)
  (material (make dielectric (index n_Si)))) ; c-Si cylinder (most outer grating
  one)

  (make cylinder (center (- (+ (/ sx -2) dpml pad wgl) ggap) 0 (+ (/ sz -4) (/ wgh
  2))) (radius (- (* gper 4) (- gper ggap))) (height wgh) (axis 0 0 1)
  (material (make dielectric (index 1)))) ; air cylinder (make a grating shape)

  (make cylinder (center (- (+ (/ sx -2) dpml pad wgl) ggap) 0 (+ (/ sz -4) (/ wgh
  2))) (radius (* gper 3)) (height wgh) (axis 0 0 1)

```

3D grating coupler flux simulation

C:\Users\Faraon Lab\Documents\Andrej_lab\MEEP\20170418_c-Si_ring_on_SiC\3D grating for TMSI\curved_grating_on_SiC_flux_TM.ctf Wednesday, September 11, 2019 3:31 PM

```

(material (make dielectric (index n_Si)))) ; c-Si cylinder (most outer grating
one)
(make cylinder (center (- (+ (/ sx -2) dpml pad wgl) ggap) 0 (+ (/ sz -4) (/ wgh
2))) (radius (- (* gper 3) (- gper ggap))) (height wgh) (axis 0 0 1)
(material (make dielectric (index 1)))) ; air cylinder (make a grating shape)

(make cylinder (center (- (+ (/ sx -2) dpml pad wgl) ggap) 0 (+ (/ sz -4) (/ wgh
2))) (radius (* gper 2)) (height wgh) (axis 0 0 1)
(material (make dielectric (index n_Si)))) ; c-Si cylinder (most outer grating
one)
(make cylinder (center (- (+ (/ sx -2) dpml pad wgl) ggap) 0 (+ (/ sz -4) (/ wgh
2))) (radius (- (* gper 2) (- gper ggap))) (height wgh) (axis 0 0 1)
(material (make dielectric (index 1)))) ; air cylinder (make a grating shape)

(make cylinder (center (- (+ (/ sx -2) dpml pad wgl) ggap) 0 (+ (/ sz -4) (/ wgh
2))) (radius (* gper 1)) (height wgh) (axis 0 0 1)
(material (make dielectric (index n_Si)))) ; c-Si cylinder (most outer grating
one)
(make cylinder (center (- (+ (/ sx -2) dpml pad wgl) ggap) 0 (+ (/ sz -4) (/ wgh
2))) (radius (- (* gper 1) (- gper ggap))) (height wgh) (axis 0 0 1)
(material (make dielectric (index 1)))) ; air cylinder (make a grating
shape)

(make block (center (- (+ (/ sx -2) dpml pad wgl) ggap (* 3 gper (sin (/ ga 2))))
(* gper 3 (cos (/ ga 2))) (+ (/ sz -4) (/ wgh 2)))
(size (* 12 gper) (* 6 gper) wgh) (e1 (cos (/ ga 2)) (sin (/ ga 2)) 0) (e2 (sin
(/ ga 2)) (- 0 (cos (/ ga 2))) 0) (e3 0 0 1)
(material (make dielectric (index 1)))) ; Air block at +y direction (to make the
grating angle)

(make block (center (- (+ (/ sx -2) dpml pad wgl) ggap (* 3 gper (sin (/ ga 2))))
(* gper -3 (cos (/ ga 2))) (+ (/ sz -4) (/ wgh 2)))
(size (* 12 gper) (* 6 gper) wgh) (e1 (cos (/ ga 2)) (- 0 (sin (/ ga 2))) 0) (e2
(sin (/ ga 2)) (cos (/ ga 2)) 0) (e3 0 0 1)
(material (make dielectric (index 1)))) ; Air block at -y direction (to make the
grating angle)

(make block (center (/ (- (+ dpml pad wgl) sx) 2) 0 (+ (/ sz -4) (/ wgh 2))) (size
(+ dpml pad wgl 0.2) wgw wgh)
(material (make dielectric (index n_Si)))) ; c-Si waveguide

; (make block (center (- (/ (+ pad dpml) 2) 0.2) 0 (- (/ sz 2) dpml 0.5)) (size (-
sx (* dpml 2) pad wgl) (- sy (* dpml 2)) 0.2)
; (material (make dielectric (index n_Si)))) ; test flux block

; (make block (center (- (/ sx 2) dpml 0.2) 0 (- (+ (/ sy 8) (* wgh 1.5) (* dpml
-0.5)) 0.2)) (size 0.2 (- sy (* dpml 2)) (- (* sz 0.75) dpml (* wgh 3)) )
; (material (make dielectric (index n_Si)))) ; test flux block

(make block (center 0 0 (* sz (/ -3 8))) (size sx sy (/ sz 4))
(material (make dielectric (index n_SiC)))) ; SiC substrate
))

(set! symmetries (list

(make mirror-sym (direction Y) (phase -1)) ;Use odd mirror symmetry for xz plane at y=0
))

(set! pml-layers (list (make pml (thickness dpml))))

```

3D grating coupler flux simulation

```

C:\Users\Faraon Lab\Documents\Andrei_lab\MEEP\20170418_c-Si_ring_on_SiC\3D grating for TMSI\curved_grating_on_SiC_flux_TM.ctf  Wednesday, September 11, 2019 3:31 PM
(set! sources (list
  (make source
    (src (make gaussian-src (frequency fcen) (fwidth df)))
    (component Ez)
    (center (+ (/ sx -2) dpml 0.1) 0 (+ (/ sz -4) (/ wgh 2))) (size 0 wgw wgh))
  ))

(set-param! resolution res)

;Setting flux region to compute flux through specified area
(define trans ; transmitted flux to y direction
  (add-flux fcen df nfreq
    (make flux-region
      (center (- (/ (+ pad dpml) 2) 0.2) 0 (- (/ sz 2) dpml 0.5)) (size (- sx (*
        dpml 2) pad wgl) (- sy (* dpml 2) 0))))))

(define trans2 ;transmitted flux to x
direction
  (add-flux fcen df nfreq
    (make flux-region
      (center (- (/ sx 2) dpml 0.2) 0 (- (+ (/ sy 8) (* wgh 1.5) (* dpml -0.5))
        0.2)) (size 0 (- sy (* dpml 2)) (- (* sz 0.75) dpml (* wgh 3)) ))))

(run-until 300 (at-beginning output-epsilon) (at-every 30 output-efield) )
(display-fluxes trans trans2)

```

3D grating coupler flux normalization (simple waveguide)

```

C:\Users\Faraon Lab\Documents\Andrej_lab\MEEP\20170418_c-Si_ring_on_SiC\3D grating for TMSI_wg_on_SiC_TM.ctf
Wednesday, September 11, 2019 3:33 PM

; TM mode (Ez)

(define-param wgh 0.24) ;height of the waveguide + grating
(define-param wgl 0.50) ;length of the waveguide (doesn't include pad or dpml)
(define-param wgw 0.40) ;width of the waveguide
(define-param gangle 0) ;Full angle of the grating (deg)
(define ga (* (/ gangle 180) pi));Full angle of the grating (rad)
(define-param gper 0.470) ;grating period
(define-param gduty 0.82) ;duty cycle of the grating
(define ggap (* gper (- 1 gduty))) ;width of the grating gap
(define-param gn 6) ;Grating number
(define-param i 0)

(define-param res 40) ;resolution
(define-param fcen 0.9341) ; pulse center frequency 1070nm
(define-param df 0.01) ; pulse width (in frequency)
(define-param tim 100) ;running time
(define-param dpml 0.5) ; thickness of PML (one side)
(define-param pad 0.5) ; thickness of pad b/w PML and edge of the ring (one side)

(define-param n_Si 3.550) ; refractive index of c-Si at 1070nm
(define-param n_SiC 2.637) ; refractive index of SiC
(define-param nfreq 10) ; number of frequencies at which to compute flux

(define sx (- (+ wgl (* gper 6) (* pad 2) (* dpml 2)) ggap))
(define sy (+ (* pad 2) (* dpml 2) (* (sin (/ ga 2)) gper 12)))
(define sz 7.5)

(set! geometry-lattice (make lattice (size sx sy sz)))

(set! default-material (make medium (index 1))) ; air

(set! geometry (list

  (make block (center (/ (- (+ dpml pad wgl) sx) 2) 0 (+ (/ sz -4) (/ wgh 2))) (size
    (* sz 3) wgw wgh)
    (material (make dielectric (index n_Si))))); c-Si waveguide

  (make block (center 0 0 (* sz (/ -3 8))) (size sx sy (/ sz 4))
    (material (make dielectric (index n_SiC))))); SiC substrate

))

(set! symmetries (list

  (make mirror-sym (direction Y) (phase -1)) ;Use odd mirror symmetry for xz plane at y=0

))

(set! pml-layers (list (make pml (thickness dpml))))

(set! sources (list
  (make source
    (src (make gaussian-src (frequency fcen) (fwidth df)))
    (component Ez)
    (center (+ (/ sx -2) dpml 0.1) 0 (+ (/ sz -4) (/ wgh 2))) (size 0 wgw wgh))
  ))

(set-param! resolution res)

```

3D grating coupler flux normalization (simple waveguide)

C:\Users\Faraon Lab\Documents\Andrei_lab\MEEP\20170418_c-Si_ring_on_SiC\3D grating for TMSI_wg_on_SiC_TM.ct Wednesdays, September 11, 2019 3:33 PM

```
;Setting flux region to compute flux through specified area
(define trans ; transmitted flux right before going into grating
part
  (add-flux fcen df nfreq
    (make flux-region
      (center (+ (/ sx -2) dpml pad wgl) 0 (+ (/ sz -4) (/ wgh 2))) (size 0 (*
        wgw 1.5) (* wgh 1.5) ) ) ) )

(define trans2 ;transmitted flux to x
direction
  (add-flux fcen df nfreq
    (make flux-region
      (center (- (/ sx 2) dpml 0.1) 0 (+ (/ sz -4) (/ wgh 2))) (size 0 (* wgw
        1.5) (* wgh 1.5) ) ) ) )

(run-until 300 (at-beginning output-epsilon) (at-every 30 output-efield) )
(display-fluxes trans trans2)
```